Title
Parametric Mixing and Amplification with Nonlinear Acoustics

Author
Lu, Ting

Publication Date
2021

Peer reviewed|Thesis/dissertation

UNIVERSITY OF CALIFORNIA

Los Angeles

Parametric Mixing and Amplification with Nonlinear Acoustics

A dissertation submitted in partial satisfaction

of the requirements for the degree Doctor of Philosophy

in Electrical and Computer Engineering

by

Ting Lu

2021

ABSTRACT OF THE DISSERTATION

Parametric Mixing and Amplification with Nonlinear Acoustics

by

Ting Lu

Doctor of Philosophy in Electrical and Computer Engineering

University of California, Los Angeles, 2021

Professor Yuanxun Wang, Chair

The wireless industry has changed our lives in many different aspects in the past decade. As the communication technology develops, the complexity of our mobile RF front-end increases because of advanced communication standards. This requires next generation RF front-end to be more efficient and compact than presently available. Acoustic wave devices have been widely used for filters and diplexers in the radio frequency front-end module due to their excellent quality factor and small footprints at radio frequency. Acoustic duplexers offer great isolation for transmitting and receiving signals at closely spaced frequency bands in frequency division duplex communication systems. However, the exploitation of these acoustic wave technologies remains in the passive domain rather than active domain.

This dissertation is to explore parametric mixing and amplification on the acoustic wave platform, with the aim to develop a new class of nonlinear acoustic components such as acoustic mixers providing orders of magnitude improvement in size, and novel acoustic resonators with enhanced and amplified performance. Firstly, the acoustic nonlinear transmission line concept is proposed using the analogy between electromagnetic wave and acoustic wave, i.e., parametric mixing is

expected to happen in the nonlinear acoustic waveguide where the mechanical stiffness is modulated by the pump wave. This concept is proved using multi-physics finite element simulation and validated with analytical equations. Secondly, practical implementations of acoustic nonlinear transmission line using nonlinear materials including Barium Strontium Titanite (BST) and Aluminum Nitride (AlN) are investigated. Parametric mixing is observed in the BST coupled surface acoustic wave grating and in the AlN Lamb wave delay line. Comparing to BST implementation, AlN implementation demonstrates a higher nonlinear stiffness modulation under same power level and is more optimal for power efficient parametric mixing and amplification purpose. Lastly, a non-degenerate phase independent parametric Q-enhancement technique is explored and demonstrated on AlN Lamb wave resonators. This technique is implemented by parametrically pumping AlN material stiffness to realize a negative resistance seen at the signal path. A multi-resonance coupled nonlinear model is developed to simulate the parametric coupling of each resonance and extract the nonlinearity of AlN from experimental data. The device quality factor is boosted in both simulation and experiment with proper pump frequency and pump power. This dissertation presents a complete study of parametric mixing and amplification on the nonlinear acoustic platform, and it can be readily capitalized to develop nonlinear acoustic devices for future communication systems.

The dissertation of Ting Lu is approved.

Chee Wei Wong

Gregory P. Carman

Robert N. Candler

Yuanxun Wang, Committee Chair

University of California, Los Angeles

2021

This dissertation is dedicated to my family.

For their love, encouragement and support.

TABLE OF CONTENTS

LIST OF FIGURES

LIST OF TABLES

SYMBOLS AND ACRONYMS

AlN	Aluminum Nitride
BAW	Bulk Acoustic Waves
BST	Barium Strontium Titanite
EM	Electromagnetics
FDD	Frequency Division Duplex
FEM	Finite Element Method
IDT	Interdigital Transducer
mBVD	Modified Butterworth Van Dyke
PCB	Printed Circuit Board
Q factor	Quality Factor
RF	Radio Frequency
SAW	Surface Acoustic Wave
TVTL	Time Varying Transmission Line
VNA	Vector Network Analyzer

ACKNOWLEDGMENTS

I would like to express my gratitude to my advisor, Professor Yuanxun Wang, for his professional comments, remarks, and engagement throughout this work. Professor Wang provides many valuable helps and encouragement when I run into puzzles of my research. He is my role model for conducting research. I have learned from Professor Wang the knowledge and principle in managing research, collaborating with people from different discipline, and the spirit of always seeking for challenge and improvement, which I really appreciate and would benefit my future career.

I would also like to sincerely thank my committee members, Professor Chee Wei Wong, Professor Robert Candler and Professor Greg Carman, for reviewing, discussing and providing help for this dissertation and my work. It's a great honor for me to have them serve as my committee members.

I am very grateful to my excellent collaborators for their support and contribution to this work. In particular, I would like to thank Professor Greg Carman, Dr. Joseph Schneider, Professor Robert Candler, Dr. Sidhant Tiwari for the tremendous fabrication and experiment support. I would like to thank Dr. Zhi Yao, Dr. Cui Han, Xiating Zou, Qian Gao, Dr. Lap K. Yeung and other lab mates in Digital Microwave Lab for great discussions and help.

I would also like to thank the public lab resources at UCLA for providing fabrication and experiment facilities. I would like to acknowledge Minji Zhu, the lab manager of Center for high frequency electronics (CHFE), for his help and support, and staff members in UCLA Nanoelectronics Research Facility and the Integrated Systems Nanofabrication Cleanroom, Lorna Tokunaga and Krissy Do, for their helpful discussions.

I also gratefully acknowledge sources of financial support for this work. This work is supported by the Emerging Frontiers in Research and Innovation (EFRI) program of National Science Foundation. I also acknowledge the financial support from UCLA department fellowship and UCLA dissertation year fellowship, and internship opportunities from Skyworks and Qualcomm.

Finally, I express my deepest love to my parents, my boyfriend Peng and my friends for their love, encouragement, and support.

VITA

Education:

2018-2021	Graduate Student Researcher in Electrical and Computer Engineering
	University of California, Los Angeles, USA
2016-2018	M.S. in Electrical and Computer Engineering
	University of California, Los Angeles, USA
2012-2016	B.S. in Information Engineering (Optics)
	Zhejiang University, Hangzhou, P.R. China

Publications:

The work presented in this dissertation is based on the following publications and conference presentations:

1. **T. Lu**, J.D. Schneider, X. Zou, S. Tiwari, Z. Yao, G.P. Carman, R.N. Candler, Y.E. Wang. “Lamb Wave Resonator Loaded Non-reciprocal RF Devices.” International Microwave Symposium (IMS), IEEE, 2020
2. J.D. Schneider, **T. Lu**, S. Tiwari, X. Zou, A. Mal, R.N. Candler, Y.E. Wang, G.P. Carman. "Frequency conversion through nonlinear mixing in acoustic waves." Journal of Applied Physics 128, no. 6 (2020): 064105.
3. Z. Yao, S. Tiwari, **T. Lu**, J. Rivera, K.Q.T. Luong, R.N. Candler, G.P. Carman, Y.E. Wang "Modeling of Multiple Dynamics in the Radiation of Bulk Acoustic Wave Antennas," in IEEE Journal on Multiscale and Multiphysics Computational Techniques, vol. 5, pp. 5-18, 2020

4. **T. Lu**, J.D. Schneider, Z. Yao, G.P. Carman, Y.E. Wang. “Nonlinear Surface Acoustic Wave Grating for Parametric Amplification.” Radio and Wireless Symposium (RWS), IEEE, 2019

5. J. D. Schneider, **T. Lu**, S. Tiwari, X. Zou, A. Mal, R.N. Candler, Y.E. Wang, G.P. Carman. “Parametric Coupling in Aluminum Nitride Lamb Wave Devices Through a Nonlinear Elastic Modulus.” Conference presentation, American Physical Society, March 2020

6. **T. Lu**, J.D. Schneider, Z. Yao, G.P. Carman, Y.E. Wang*. “Barium Strontium Titanite couple Surface Acoustic Wave Transmission Line.” Progress in Electromagnetics Research Symposium, 2019

7. J. D. Schneider, **T. Lu**, G.P. Carman, Y.E. Wang, A. Mal. “Parametric coupling in Lamb wave devices", SPIE Smart Structures and Materials + NDE and Health Monitoring, Mar. 2019

8. **T. Lu**, J.D. Schneider, Z. Yao, G.P. Carman, Y.E. Wang. “Nonlinear SAW Grating for Parametric Amplification” EFRI 2-DARE, NewLAW Joint Grantees Meeting, 2018

9. **T. Lu**, J.D. Schneider, Z. Yao, M. Zakeri, S. Keller, C.S. Lynch, G.P. Carman, Y.E. Wang. “Parametric Amplification with Surface Acoustic Wave.” Center for Translational Application of Nanoscale Multiferroic System on-site NSF Annual Review, 2018

10. **T. Lu**, J.D. Schneider, M. Zakeri, Z. Yao, S. Keller, C.S. Lynch, G.P. Carman, Y.E. Wang. “Parametric Frequency Mixer on Surface Acoustic Wave platform.” Napa Microsystem Workshop, IEEE, 2017

Chapter 1 Introduction

Acoustic wave devices have been widely used for filters and diplexers in the radio frequency (RF) front-end module due to their excellent quality factor and small footprints at radio frequency. However, the exploitation of these acoustic wave technologies remains in the passive domain rather than active domain. Here, this work is to explore parametric mixing and amplification on the acoustic wave platform, with the aim to develop a new class of nonlinear acoustic components such as acoustic mixers that provide orders of magnitude improvement in dramatically reduces size, and novel acoustic resonators with enhanced and amplified performance.

1.1 Background and Motivation

The wireless industry has changed our lives in many ways in the past decade. This change is largely attributed to the semiconductor advancement based integrated circuit (IC) technology which generates fasted, smaller and more power efficient mobile devices. However, some limitations of the IC technology such as inability to high quality factors (Q) on-chip components remain and need further resolving. Besides, as the communication technology develops, the complexity of our mobile RF front-end increases. Figure 1-1 shows the schematic of a mobile receiver. The RF components are labeled in red. As the cellular standards develop, the number of communication bands increases, thus more and more filters/duplexers, amplifiers and mixers are required at the RF front-end. This increases the need for developing high performance next device generation RF front-end which is more efficient and smaller than presently available.

Acoustic wave devices are essential components in most RF front-end because the acoustic material has intrinsic high quality factor. Commercial acoustic products include surface acoustic wave and bulk acoustic wave filters and duplexers that have quality factor around 4000. RF

duplexers made of acoustic wave components are very important. As shown in Figure 1-2, each communication band requires an acoustic duplexer which consist of a TX filter and a RX filter to isolate transmitting and receiving signals at closely spaced frequency bands in frequency division duplex communication systems, and the acoustic duplexer protects receiver from strong transmitting signal. Acoustic duplexers can offer low in-band insertion loss (~1-2dB) and high out of band rejection(50-60dB) at a very narrow duplex spacing, usually 45MHz or even less. This is very hard to be achieved by other type of duplexers. Meanwhile, because the acoustic wave propagates much slower than the electromagnetic wave in the radio frequency, acoustic wave devices have dramatically reduced size compared to the electronic counterparts.

To summary, acoustic wave devices have the advantage of largely reduced footprint due to short wavelength at radio frequency and high quality factor in acoustic resonators, filters and delay lines. However, the exploitation of the acoustic wave technologies remains in the passive domain rather than active domain. To advance these acoustic wave devices they must be packaged with active semiconductor ICs in a RF front-end device and suffer performance degradation and additional assembly cost.

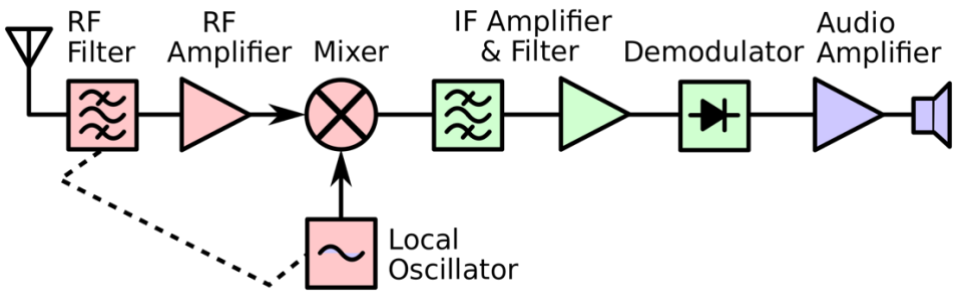

Figure 1-1: Schematic of a mobile receiver. In the RF stage (components in red), the signal is sensed by the antenna, filtered, amplified, and mixed down to the intermediate frequency (IF).

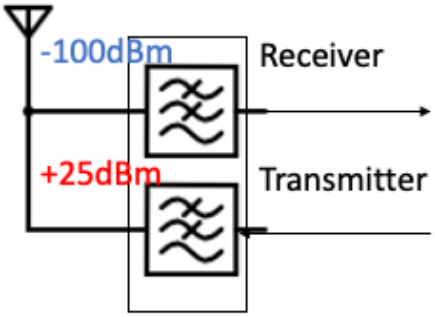

Figure 1-2: An acoustic duplexer in the RF front end. It consists of a TX filter and a RX filter to isolate transmitting and receiving signals at closely spaced frequency bands in frequency division duplex communication systems

The motivation for this work is to develop parametric mixing and amplification on the acoustic wave platform, which will obtain great leverage on the slow velocity and short wavelength of acoustic waves at RF to minimize the footprint of transmission lines and the high quality factor of mechanical resonances and acoustic wave propagation to reduce the noise associated with energy loss. The short-term goal is to develop a new class of nonlinear acoustic components such as parametric acoustic mixers providing orders of magnitude improvement in size, and novel acoustic resonators with parametric enhanced quality factor. The long-term vision for this work is to yield a new acoustic RF front-end which includes acoustic filters, acoustic amplifiers and acoustic mixers providing orders of magnitude improvements in dramatically reduced size without degrading performance.

1.2 Introduction to Acoustic Wave Devices

Acoustic filters nowadays are the most popular filter technology to meet the cellular phone standards requirement with their form factor. [1] Surface acoustic wave devices became attractive after the interdigital transducer (IDT) was invented in 1965. [2] The arise of IDT allowed for efficient excitation and detection of surface acoustic wave on piezoelectric substrate.

Surface acoustic wave technology was first used for intermediate frequency (IF) filters [3] and then replaced the ceramic platform for making RF filters. The development of bulk acoustic wave (BAW) technology for filter application was started around 1980s.[4] Today, in the frequency range up to 1GHz, filters made of surface acoustic wave(SAW) dominate the market, while surface acoustic wave filters and bulk acoustic wave (BAW) filters are competing for their share in the frequency above 1GHz. As the technology develops, new acoustic wave technology arises and is making progress. Recently, the Lamb wave platform is being intensively explored because the higher order modes of Lamb wave allow for higher operating frequencies. [5]

Success of acoustic devices is because of the availability of high-quality piezoelectric substrates, reliable fabrication technologies, precise simulation software and advanced design tools. This section gives a brief overview of acoustic basics to engineers and researchers who want to dig into this field.

1.2.1 Constitutive Equations for Linear Piezoelectricity

The derivation of the constitutive equation for piezoelectricity can be found in [6] and briefly summarize below.

Dielectric property of insulating material is characterized by a relationship between the electric field E and electrical displacement D:

$$D = \varepsilon E \tag{1.1}$$

In this case, ε is the dielectric permittivity defined under a DC bias electric field and tested with a small AC electric field

$$\varepsilon(E_0) = \left.\frac{dD}{dE}\right|_{E=E_0} \tag{1.2}$$

Elastic properties of a solid dielectric are controlled by Hook's law written as

$$T = cS \tag{1.3}$$

where T is the stress tensor, S is the strain tensor, c is the elastic stiffness tensor.

In piezoelectric material, the electromechanical coupling should be added, and the constitutive equation for electrical displacement (1.1) should be modified by adding the contribution of piezoelectric effect. A new constitutive equation is written as

$$D = eS + \varepsilon^S E \tag{1.4}$$

where e is the piezoelectric coupling constant, the upper suffix 'S' is added to the dielectric permittivity tensor ε^S to indicate that it is measured under the condition of constant strain (i.e., the material is mechanically clamped during the measurement).

Using thermodynamics, converse piezoelectric response must be exhibited in materials exhibiting piezoelectric response, i.e., response of mechanical stress to the applied electric field. Same piezoelectric coupling constant is used for both direct piezoelectric effect and converse piezoelectric effect. A modified constitutive equation for mechanical stress (1.3) is written as

$$T = c^E S - eE \tag{1.5}$$

Where the upper suffix 'E' is added to the elastic stiffness c^E to indicate that it is measured under the condition of constant electric field (i.e., the material is under short-circuited electrical condition during the measurement).

If the mechanical condition changes, the dielectric response of piezoelectric material will also be changed. The dielectric permittivity of piezoelectric material with mechanically free condition ε^T can be found by substituting $T = 0$ to equation (1.4) and (1.5):

$$\varepsilon^T = \frac{\partial D}{\partial E}\Big|_{T=0} = \varepsilon^S + \frac{e^2}{c^E} \tag{1.6}$$

Intuitively, this response happens since the electric field does not only affect the electric displacement but also deforms the sample through the direct piezoelectric effect. This deformation adds back to the electrical displacement through the converse piezoelectric effect.

Similarly, the elastic stiffness measured under the open circuit condition c^D differs from that measured under short circuit condition c^E, and can be found by substituting $D = 0$ to equation (1.4) and (1.5):

$$c^D = \frac{\partial T}{\partial S}\Big|_{D=0} = c^E + \frac{e^2}{\varepsilon^S} \tag{1.7}$$

linear piezoelectric is addressed in this subsection and nonlinear piezoelectric will be discussed in chapter 3.

1.2.2 Finite Element Modelling of Piezoelectricity

Precise modelling technology is typically implemented in the acoustic wave device design process. Modern finite element method (FEM) uses fully coupled multi-physics package for electromagnetics, structural mechanics, acoustics, fluid flow, heat transfer, and chemical engineering behavior. The finite element method offers the opportunity to simulate piezoelectric material and acoustic components using fully coupled physics of electrostatics and solid mechanics. This subsection describes the modelling of surface acoustic wave devices as an example, for demonstrating the effects of external circuit on the interdigital transducer (IDT), propagation of surface acoustic wave, and coupling between electrical energy and mechanical energy. Note the FEM modeling knowledge is applied in chapter 2 for demonstrating the parametric effects on surface acoustic platform.

Surface acoustic wave can be excited by applying voltage on the interdigital transducer. Figure 1-3 shows the geometry of interdigital transducer. In the simulation, the substrate material is YX-128° cut lithium niobate, the interdigital transducer material is gold. The wave speed in YX-128° cut lithium niobate is 3895 m/s, the frequency for excited surface acoustic wave is 861MHz, the width and gap for each interdigital transducer are a quarter wavelength of the surface acoustic wave. The voltage excition is 1V which applied to the first, third, and fifth interdigital transducer from the left, and the ground is applied to the second, fourth, and sixth interdigital transducer from the left. The electrostatics and solid mechanics physics are applied to all the regions in the geometry, the boundary condition for left, bottom, and right edge of the lithium niobate is low-reflection boundary.

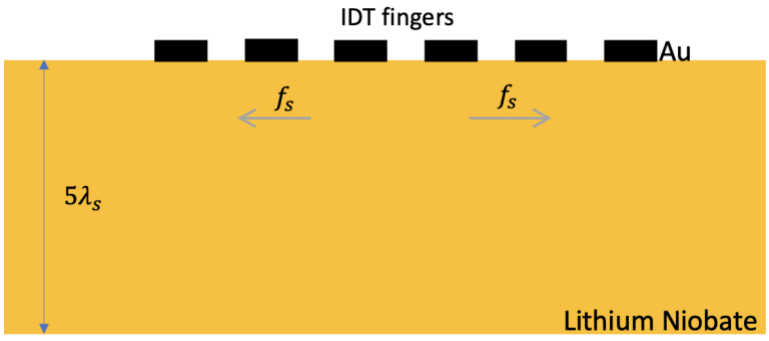

Figure 1-3: Simulated interdigital transducer (IDT) geometry.

Surface acoustic waves can be excited in time domain or frequency domain. Time domain simulation is better for observing the propagation of acoustic wave. Figure 1-4 shows the displacement at three different time steps, where the propagating pattern for surface acoustic wave can be observed.

Besides displacement, strain, stress, and electric potential of surface acoustic wave are also simulated. Figure 1-5 shows the strain(S11), stress(T11) and electric potential when surface acoustic wave reaches the low reflection boundary. Figure 1-5(c) shows that the electric

potential for surface acoustic wave is low, and it is a sign of large insertion loss in the surface acoustic wave delay line. Therefore, equivalent circuit model of interdigital transducer is developed in the next subsection for impedance matching.

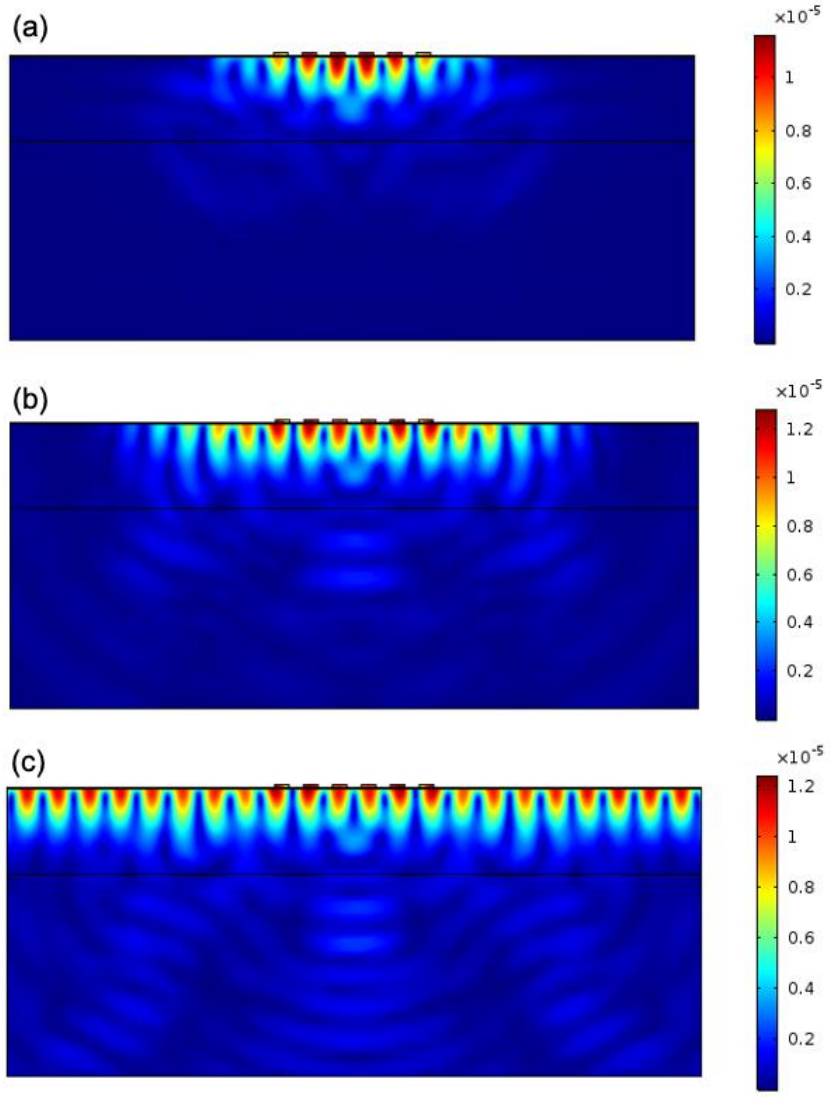

Figure 1-4: Displacement of surface acoustic wave at time step (a) 1.7×10^{-9}s (b) 3.44×10^{-9}s (c) 1.042×10^{-8}s.

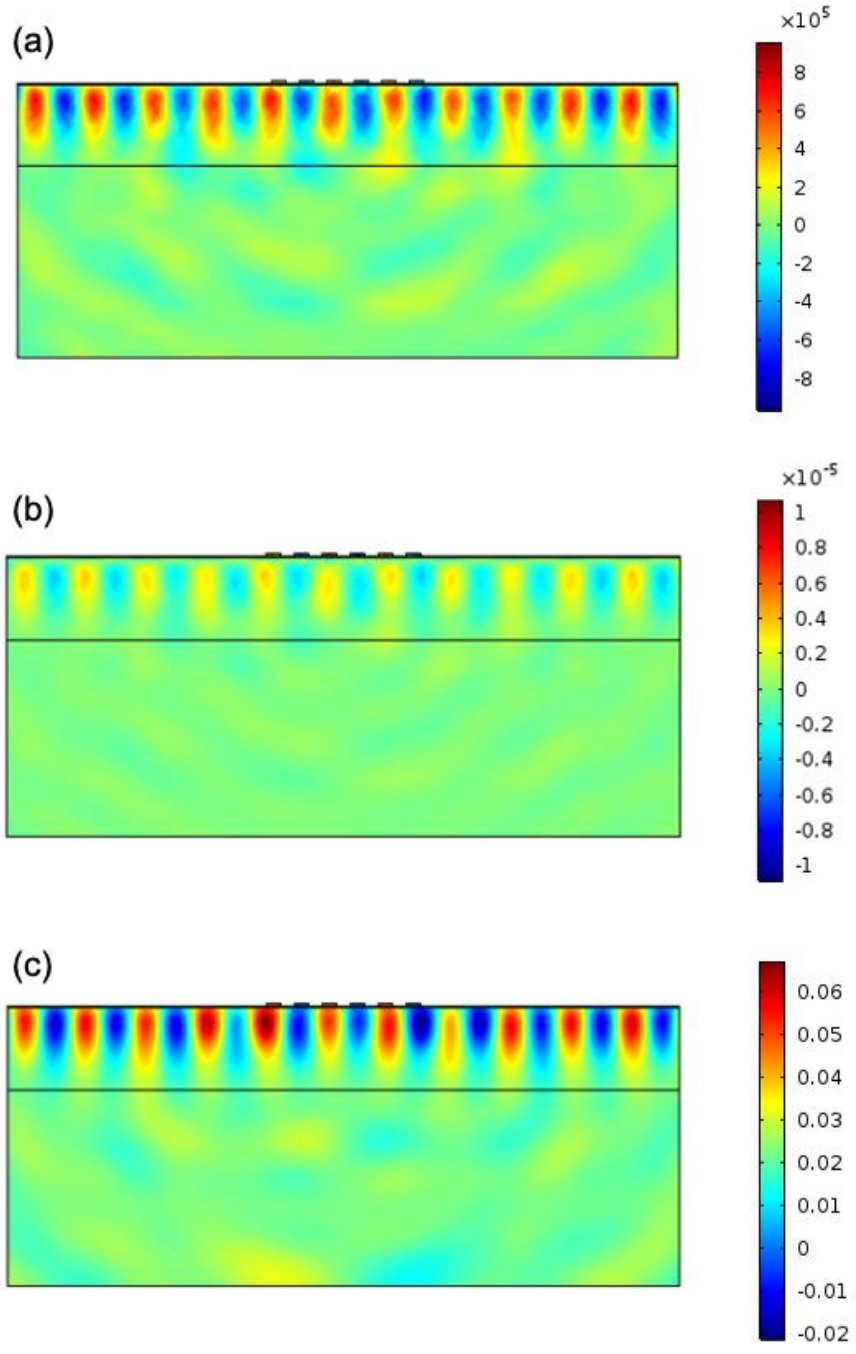

Figure 1-5: (a) Strain (S11) (b) Stress (T11) (c) Electric potential at time step 9.3×10^{-9}s.

1.2.3 Circuit Model for Interdigital Transducer and Impedance Matching

Equivalent circuit model is another efficient and precise technology for simulating acoustic wave components. Equivalent circuit model emphasizes the electrical properties, and in this subsection the modelling knowledge is used for impedance matching of the acoustic wave devices. Impedance matching is essential for RF devices to minimize power reflection and maximize power transmission. Note that the equivalent circuit modelling knowledge is also applied in chapter 3 and chapter 4 for predicting the parametric mixing and amplification effects.

Mason circuit has been widely used for modeling surface acoustic wave interdigital transducers[7]. Figure 1-6 shows the mason equivalent circuit model for one periodic section of interdigital transducer. Because surface acoustic wave can travel in both directions in the substrate, so the network has three ports with two acoustic ports and one electrical port. The mason equivalent circuit contains capacitors that represent electrode capacitance per section, transformers that represent the electromechanical coupling between electromagnetic wave and acoustic wave, and sections of transmission line that represent the propagation of surface acoustic wave on the piezoelectric substrate.

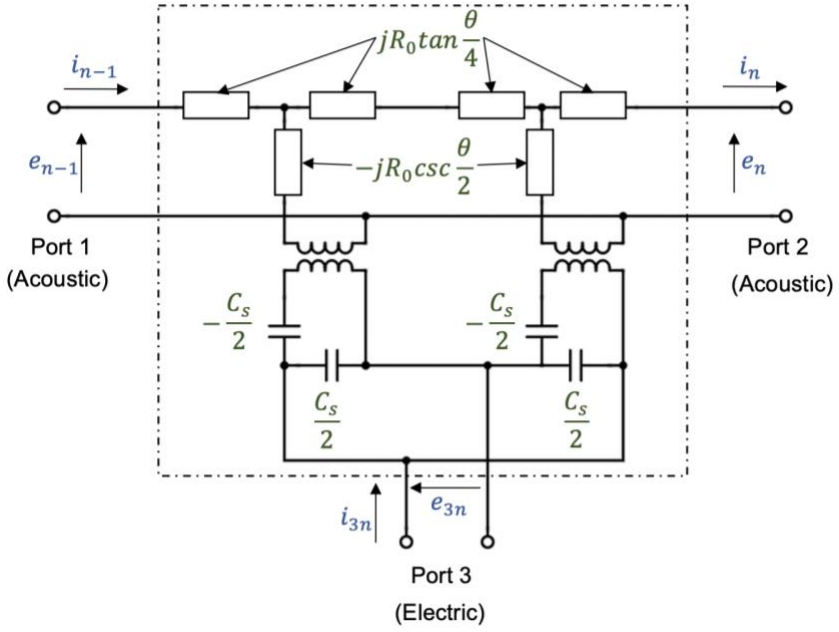

Figure 1-6: Mason equivalent circuit for one period section, adapted from [7].

The Mason equivalent circuit models the full physics of piezoelectric, electrostatic, and mechanic. This model can be simplified if only electrostatic, piezoelectric and resonance are of interest. As shown in Figure 1-7, the interdigital transducer can be modeled by admittance $Y = G(f) + jB(f)$ that represents electromechanical coupling and resonance, and capacitance C_0 that represents the static capacitor between electrodes. When the interdigital transducer is at resonance, the imaginary part of the admittance becomes zero.

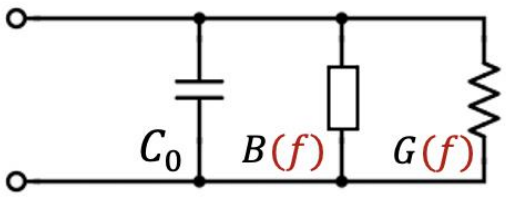

Figure 1-7: Simplified equivalent circuit of interdigital transducer.

Based on the theory, a straightforward equivalent circuit for impedance matching of two-port surface acoustic wave delay line is developed as shown in Figure 1-8. Here, one set of interdigital transducers is for exciting the surface acoustic wave (input), one set of interdigital transducers is for transforming the mechanical wave into electromagnetic wave(output). The two-port surface acoustic wave delay line is put into a black box, and a Z matrix is used to model the behavior. This method offers tremendous help in designing the matching LC circuit. Because the two-port surface acoustic wave delay line is reciprocal, the same matching circuit is used in both the source and load. R_s and R_L are the source resistor and load resistor (usually 50 Ohm in experiment), respectively.

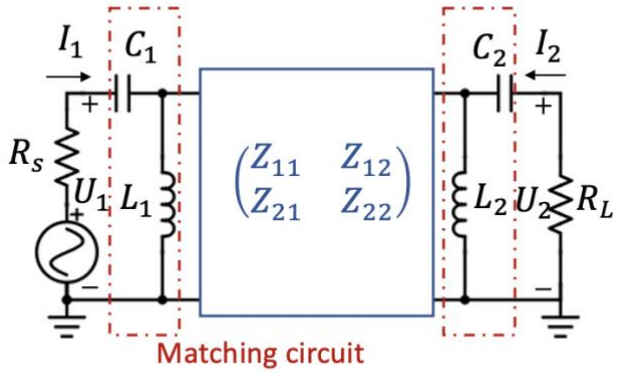

Figure 1-8: Impedance matching network for two-port surface acoustic wave delay line.

The matching circuit of two-port surface acoustic wave delay line is built in fully coupled finite element method package. The simulation demonstrates that the matching circuit can transform arbitrary transducer impedance to 50 Ohm and thus delivers higher power from the input interdigital transducers to the output interdigital transducers. The geometry of two-port surface acoustic wave delay line is shown in Figure 1-9.

Figure 1-9: Geometry of two-port surface acoustic wave delay line.

The initial input impedance of interdigital transducers is measured for determining the value of inductor and capacitor in the matching circuit. The impedance matching method is included in [8]. For extracting the impedance of interdigital transducers, voltage U_1 on the input interdigital transducers and the current I_1flowing into the network shown in Figure 1-8 are measured when the output interdigital transducers are open-circuited. The real part is 14Ohm at 973.75MHz, with imaginary part -27Ohm. The real part at the resonance frequency is caused by the energy coupling, the imaginary part is due to static capacitance of the electrodes.

The matching circuit can be designed with the input impedance of the interdigital transducers. The series capacitor $C_1(C_2)$ is 6.5378pF, and the parallel inductor $L_1(L_2)$ is 4190.9pH. By adding the matching LC circuit on both ports, larger output electrical power is obtained at output interdigital transducers. Figure 1-10(a) shows the voltage excitation U_1 on the input interdigital transducers and induced voltage U_2 on the output interdigital transducers, and Figure 1-10(b) shows the current I_1 flowing into the input interdigital transducers and the current I_2 flowing out from the output interdigital transducers. Almost 6~8 dB insertion loss is observed in the two-ports interdigital transducers configuration, which is the theoretical limit of this bidirectional two-port surface acoustic wave delay line configuration. 3dB insertion loss happens at both input and output transducers because the

acoustic wave can travel in two directions. This impedance matching technique is very helpful in developing the matching circuit for surface acoustic wave devices in simulation, with guidance on the fabrication and characterization of surface acoustic wave devices.

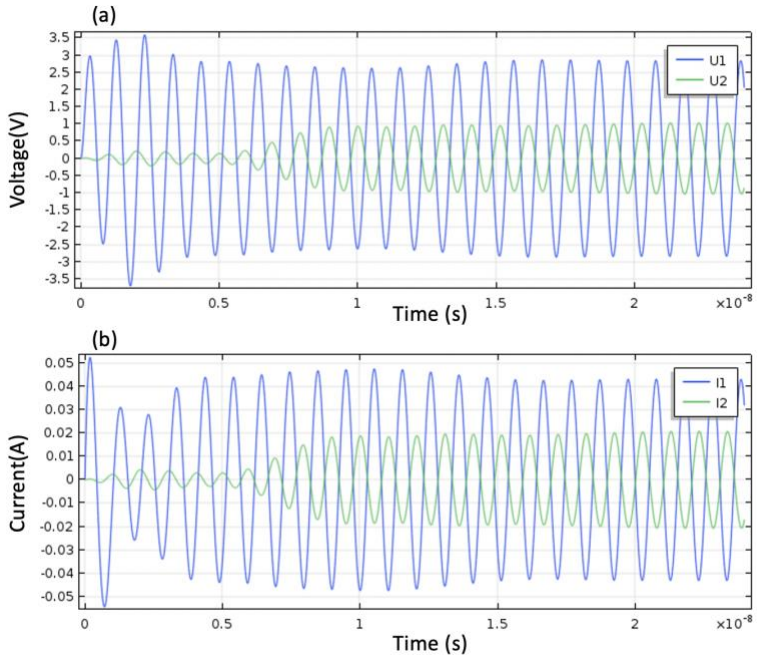

Figure 1-10: Comparison of (a) the voltage excitation U_1 on the input interdigital transducers and induced voltage U_2 on the output interdigital transducers (b) the current I_1 flowing into the input interdigital transducers and the current I_2 flowing out from the output interdigital transducers.

1.2.4 Fabrication and Characterization of Acoustic Wave devices

The general procedure of fabrication and characterization of acoustic wave devices is demonstrated in this section. A brief introduction of fabrication and characterization of surface acoustic wave devices is shown as an example below. Details about the fabrication recipes and measurement methods of surface acoustic wave devices and lamb wave devices are included in the appendix A1 and A2, respectively.

The fabrication process of surface acoustic wave delay lines includes wafer preparation, photolithography, develop, metal deposition, and lift off. Detailed recipe of every step is included in the appendix. The final chip after the whole fabrication process is shown in Figure 1-11, with each pattern on the chip representing one surface acoustic wave delay line. Comparison of the size between the chip and a coin is shown, proving that acoustic wave devices have much smaller device size than electromagnetic wave devices.

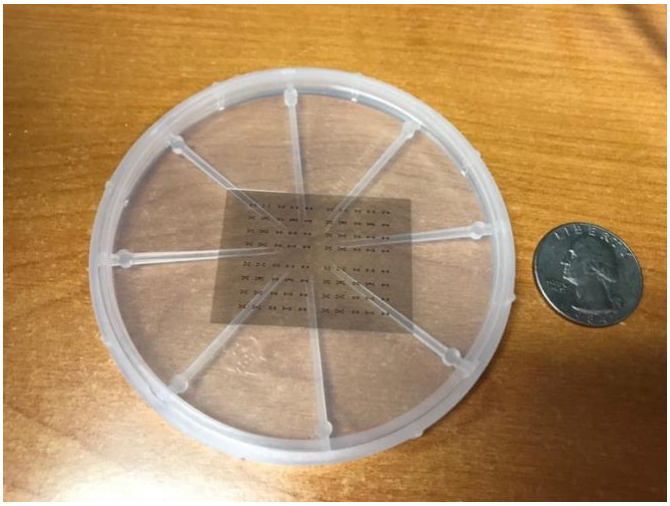

Figure 1-11: Final chip after whole fabrication process. Each pattern on the chip represents one surface acoustic wave delay line. The size comparison proves that acoustic wave devices have much smaller device size than electromagnetic wave devices.

The characterization of the acoustic devices is usually performed using the vector network analyzer (VNA). There are two ways to connect the acoustic devices to the vector network analyzer. The first method is to make printed circuit board (PCB) and use wire bonding to connect the metal pads of the acoustic device to the PCB. The PCB is connected to the VNA using cables and connectors. The details are included in the Appendix A1. The second method is to use ground-signal-ground (GSG) probes to contact the corresponding pads on the acoustic device. The probes are connected to the VNA using cables and connectors. The details are included in the Appendix A2. Before real measurement, calibration is performed for

compensating the phase and loss of the cable connections. Figure 1-12 shows the return loss (S11) and insertion loss (S21) of a two-port surface acoustic wave delay line.

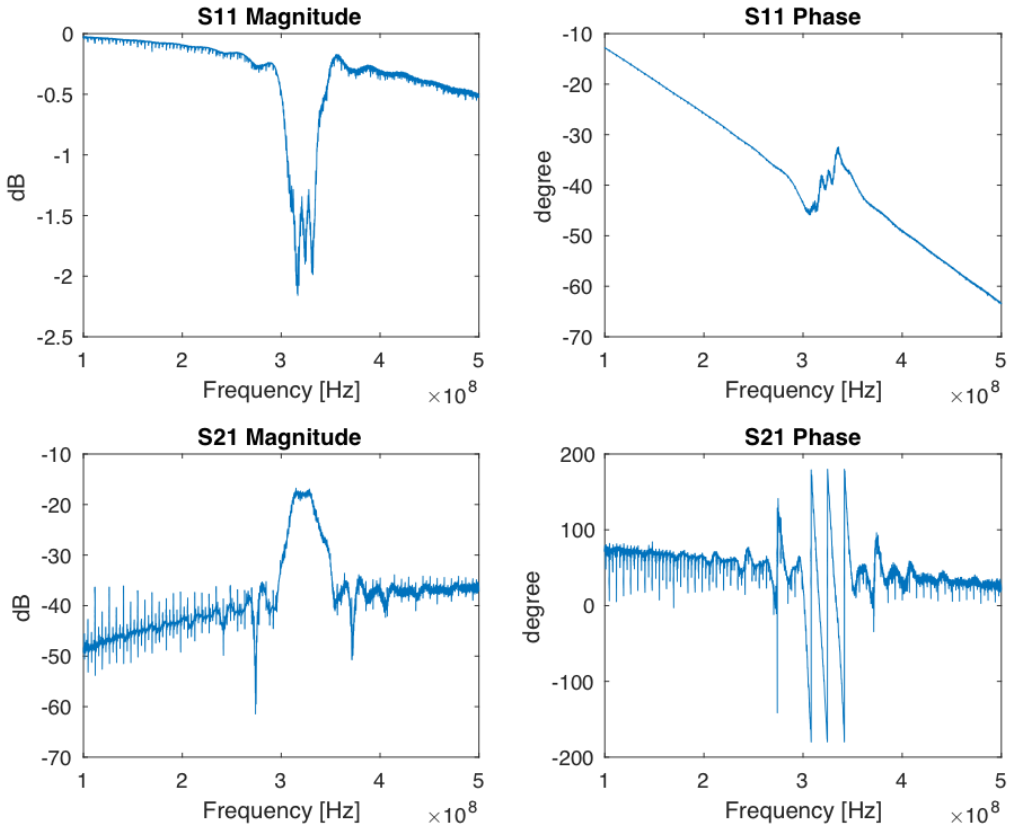

Figure 1-12: S parameters for a two-port surface acoustic wave delay line.

To summarize, this section gives a brief overview of acoustic basics, including the constitutive equations of piezoelectric, finite element method modeling and equivalent circuit modeling of interdigital transducers, and fabrication and characterization of acoustic wave devices. The knowledge in this section is applied in the following chapters to demonstrate the parametric mixing and parametric amplification on the acoustic wave platform from theory, simulation, and experiment.

1.3 Dissertation Outline

In this dissertation, parametric mixing and parametric amplification are explored on the acoustic wave platform. In chapter 2 the concept of acoustic nonlinear transmission line is clearly stated using the analogy between electromagnetic wave and acoustic wave. Unlike the past efforts, the proposed method takes advantage of high quality factor of acoustic wave for distributed effects, leverages on short wavelength of acoustic wave for device with small footprint, and explores nonlinear material that can achieve parametric amplification without lossy coupling. The method is proved in simulation and matched with analytical equations of time varying transmission line. In chapter 3 the practical implementations of acoustic nonlinear transmission line using nonlinear materials are discussed. Parametric mixing and amplification are observed in BST coupled surface acoustic wave grating by external permittivity coupling method illustrated in nonlinear constitutive equations. Besides, the nonlinear acoustic transmission line implementation using AlN is proved on the Lamb wave platform by a fabricated three-port Lamb wave delay line. Parametric mixing and frequency conversion are observed in experiment, and the nonlinear stiffness of AlN is extracted by the equivalent circuit model from experimental data. Implementations using these two different nonlinear materials are compared and AlN implementation demonstrates a higher nonlinear stiffness modulation. In chapter 4, a phase independent parametric Q-enhancement technique is explored and demonstrated on aluminum nitride (AlN) Lamb wave resonators. Additionally, a nonlinear circuit model is developed to simulate the parametric coupling of each resonance and extract the material nonlinearity from experimental data. The nonlinear model developed for multi-resonance acoustic device is a universal model that can be applied for designs of filters and waveguides built on acoustic wave platforms. The demonstrated Q-enhancement method is simple to implement and can be applied to other types of resonators that have nonlinear behavior and support multi-resonance operation. Finally, a brief conclusion will be given in

chapter 5. The author hopes that the advancements discussed in this dissertation will lead to further developments in nonlinear acoustic devices for future communication systems.

Chapter 2 Proposed Concept: Acoustic Nonlinear Transmission Line

In this chapter, the concept of electromagnetic time varying transmission line and its application on the active components are introduced. Past efforts on parametric amplification with acoustic wave platform are investigated and their limitation are discussed. Then the acoustic nonlinear transmission line idea is proposed to realize parametric effects on the acoustic platform, as inspired by the analogy between electromagnetic waves and acoustic waves. The proposed idea takes advantage of high quality factor of acoustic wave for distributed effects, leverages on short wavelength of acoustic wave for device with small footprint, and explores nonlinear material that can achieve parametric amplification without using diodes. The proposed idea is first validated using multi-physics finite element simulation, and then matched with analytical equations derived for time varying transmission line.

2.1 Introduction to Time Varying Transmission Line (TVTL)

Parametric mixers/amplifiers are reactance-based devices that utilize nonlinear reactance to create either mixing components or negative resistance. The parametric frequency conversion behavior in the time-varying transmission line was intensively studied between 1950's and 1960's [9-12]. The primary application for parametric behavior was to develop parametric amplifier without using the solid-state device. However, this interest died out later as semiconductor transistors were invented and considered as an overall better technology in terms of gain and physical dimensions of the amplifiers.

Recently there has been a resurgence of interest in utilizing parametric mixing and amplification due to the intrinsically lower noise characteristics of the reactance-based components over the conductance-based components [13-18]. Discrete parametric mixing was realized and applied in

frequency converters and multipliers [13-16]. Degenerating parametric effects are utilized in distributed circuit architectures for resonators and narrow band amplifiers [17-18]. The concept of parametric mixing and amplification has also been applied in other fields. Nonlinear optical components including optical amplifiers [19-20], optical mixers [21], optical isolator [22] and oscillators [23] are realize based on parametric effects. Josephson junctions are employed as nonlinear inductors for nonlinear wave propagation [24] and parametric amplification [25] for microwave superconducting and quantum application.

The theory of time varying transmission line (TVTL) is briefly summarized as follows. To realize time varying transmission line [26] , a nonlinear transmission line whose material property is modulated by the amplitude of the wave is used. The schematic of time varying transmission line is shown in Figure 2-1. A signal wave and a modulation wave are both launched into the same nonlinear transmission line propagating toward the +z direction at the angular frequencies ω_s and ω_m respectively. The modulation frequency is normally chosen to be greater than the signal frequency ($\omega_m > \omega_s$) in order to realize gains. Because of the nonlinearity of the material property such as the capacitance of the transmission line, the signal wave is mixed with the modulation wave, generating two sidebands of the carrier, $\omega_{m-s} = \omega_m - \omega_s$ and $\omega_{m+s} = \omega_m + \omega_s$. Assume the variation of the capacitance is small and transmission line is non-dispersive over the bandwidth interested, the phase matching condition can be written as:

$$\frac{\omega_s}{\beta_s} = \frac{\omega_{m-s}}{\beta_{m-s}} = \frac{\omega_{m+s}}{\beta_{m+s}} = \frac{\omega_m}{\beta_m} = v_p = \frac{1}{\sqrt{L'C_0'}} \tag{2.1}$$

The boundary condition at the source is:

$$v(0,t) = V_0 \cos(\omega_s t + \phi_s) \tag{2.2}$$

Using the boundary condition, a solution for the voltage along TVTL can be derived as follows:

$$v(z,t) = V_s(z)\cos(\omega_s t - \beta_s z + \phi_s) + V_{m-s}(z)\cos(\omega_{m-s} t - \beta_{m-s} z + \phi_m - \phi_s) +$$
$$V_{m+s}(z)\cos(\omega_{m+s} t - \beta_{m+s} z + \phi_m + \phi_s) \quad (2.3)$$

The amplitude of these three voltages in Equation (2.3) are functions of the propagation distance expressed as the following:

$$V_s(z) = V_0 \cos\left(\frac{1}{2\sqrt{2}}\xi\beta_s z\right) \quad (2.4.1)$$

$$V_{m-s}(z) = -\frac{V_0}{\sqrt{2}}\frac{\beta_{m-s}}{\beta_s}\sin\left(\frac{1}{2\sqrt{2}}\xi\beta_s z\right) \quad (2.4.2)$$

$$V_{m+s}(z) = -\frac{V_0}{\sqrt{2}}\frac{\beta_{m+s}}{\beta_s}\sin\left(\frac{1}{2\sqrt{2}}\xi\beta_s z\right) \quad (2.4.3)$$

where $\xi = C'_m/C'_0$ is defined as the capacitance modulation index. As shown in the results, if β_{m-s}, β_s, β_{m+s} and z are carefully chosen, the magnitude of up converted wave and down converted wave can be larger than that of original wave. In other words, gain can be realized using time-varying transmission line.

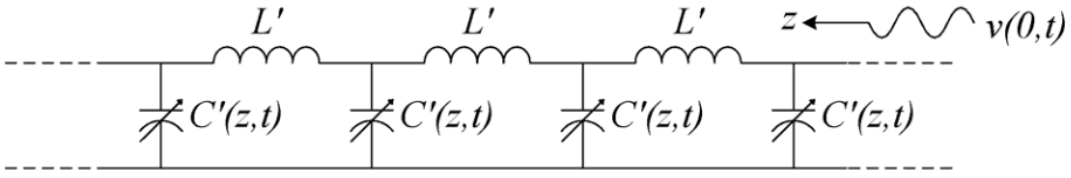

Figure 2-1: Schematic of time varying transmission line (TVTL).

On the contrast, if the signal wave travels in the opposite direction to that of the carrier wave, no solution can be obtained, which implies that no energy is coupled between the signal wave and the waves at the sidebands. The directional dependency of the parametric conversion, as a unique property of time varying transmission line, can be utilized to develop non-reciprocal components at RF front ends. The waves which travel in different directions of the time varying transmission line will result in different frequencies at the two ends of the transmission line,

with one coupling to the up converted and down converted frequency while the other remaining the same. The resulting non-reciprocity is intrinsically broadband, because it is not based on resonance structures like a conventional ferrite circulator. Because the time varying transmission line has only reactance-based components, it has very low loss and low noise characteristics. The waves at the upconverted frequencies can reach to the same or grater magnitude than that of the original signal wave, which occurs when a high carrier to signal frequency ratio is used over a long time varying transmission line. Combining with the solution of time varying transmission line provided in the previous equation, not only frequency conversion but also conversion gain can be obtained using time varying transmission line, which demonstrates its mixing and amplification application in the RF front ends.

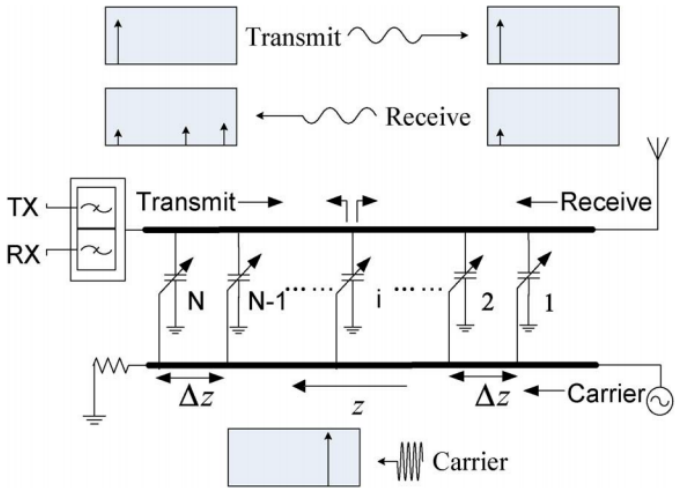

Figure 2-2: Schematic of nonreciprocal design based on TVTL [26].

Based on this concept, the UCLA group has implemented nonreciprocal TVTL for the first time on semiconductor based IC called distributedly modulated capacitor (DMC) [26]. DMC is the transmission line loaded with varactor diode to separate the overlapping signals in time, frequency and space. The schematic is shown in Figure 2-2. When the signal wave propagates in the same direction of the carrier wave on the time-varying transmission line, it will mix and get

amplified by the carrier wave. The signal wave that propagates in the opposite direction of the carrier wave will not mix with it. Consequently, the difference in the propagation direction will result in difference of the signal frequencies, which can be used in the non-reciprocal devices.

Following the DMC work, a circulator design [27] was demonstrated on GaN IC by the same group in UCLA, which achieved greater than 25dB isolation from 600MHz to 1.5GHz with the insertion loss less than 1.5dB for the balanced GaN DMC MMIC circulator. A frequency translational RF receiver [28] and a jamming resilient spread spectrum receiver[29] with RF correlator [30] based on time varying transmission line also obtained superior performances. The monolithically integrated parametric mixer design [31] with time varying transmission line was of particular interest because it demonstrated a relatively low-noise figure over traditional passive mixer while providing a mild conversion gain. Measurement results have shown that the MMIC traveling wave TVTL mixer can achieve a maximum of 2.1dB conversion gain and 2.7dB mean noise figure within the measured frequency band. This demonstrates the great potential of time varying transmission line (TVTL) to be applied in commercial products in markets.

In summary, the time varying transmission line has the intrinsic strength of low loss and low noise. The frequency conversion property can be utilized for making non-reciprocal components. The response of time varying transmission line is broadband and parametric gain can be realized. However, the measured loss and noise figure associated with MMIC implementation of TVTL come from the finite quality factor of lumped components like inductors. The acoustic wave devices have a very high quality factor and can overcome the limitation of MMIC implementation of TVTL. Furthermore, the chip size can be dramatically reduced if TVTL is implemented on the acoustic platform. Therefore, in this work the time varying transmission line concept on the acoustic wave platform is explored, for realizing parametric mixing and amplification effects and making advanced nonlinear acoustic devices.

2.2 Research on Parametric Amplification with Acoustic Waves

Acoustic wave devices have been widely used as delay lines, filters and duplexer with excellent quality factors and low losses. In contrast to the active devices based on electromagnetic wave platform, acoustic waves have drastically slower wave speeds which provide a great opportunity to shrink the physical dimension of active devices. Many works aiming at combining the concept of parametric amplification with the well-developed acoustic wave technologies have already been conducted. These include the coupling happening using external varactor circuits [32], magnetic materials [33] or semiconductors [34]. However, they all have limitations that will impede their applications.

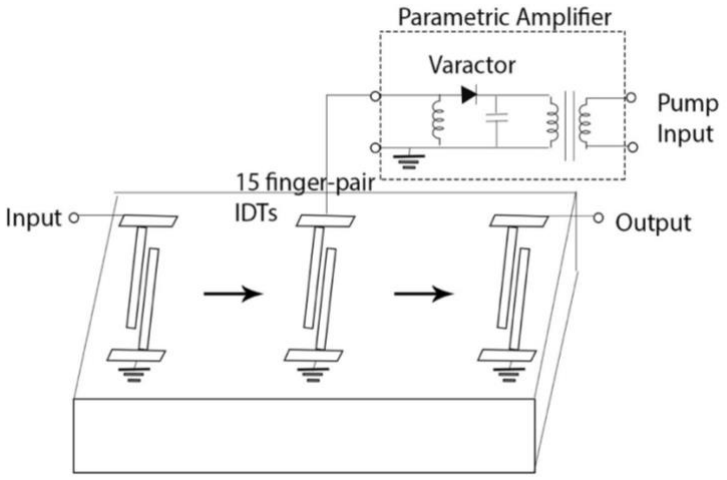

Figure 2-3: Schematic of surface acoustic wave amplifier, adapted from [32].

Parametric surface acoustic wave amplifier can be realized using lumped-element varactor parametric amplifier attached to the electrical port of an interdigital surface acoustic wave transducer as shown in Figure 2-3 [32]. In this work the transducer was placed between the input and output IDTs of the surface acoustic wave delay line. The signal wave was first converted to the electric domain, modulated by the pumping wave on the nonlinear varactor, and then

converted back to the acoustic domain. Terminal gain of 1~2 dB was observed in the forward direction. The isolation between forward direction and backward direction was about 5dB. However, passive loading of the center transducer by the parametric circuit brought relatively high insertion loss, and the chip size remained large due to the varactor circuits.

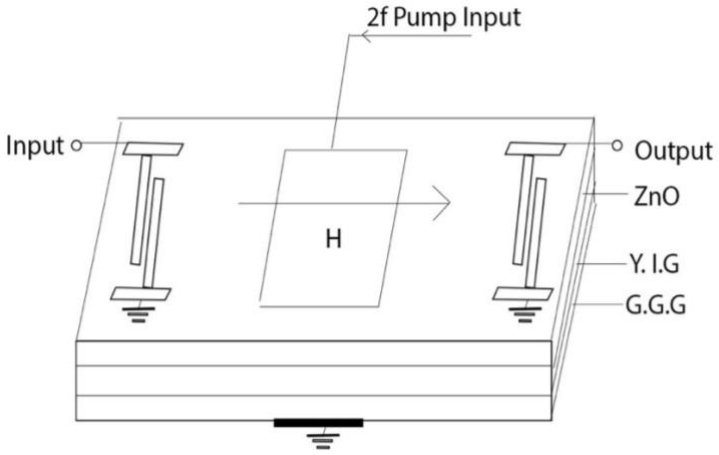

Figure 2-4: Schematic of ZnO-Ga doped yttrium iron garnet (YIG) and GGG structure, adapted from [33].

Interactions of surface acoustic wave with magnetization were investigated on a ZnO-Ga doped yttrium iron garnet (YIG) and GGG structure as shown in Figure 2-4[33]. Nonlinear interaction between surface acoustic wave and magnetization contributed to the parametric effects on the acoustic wave. Parametric amplification of SAW was closely related to the magnetic field strength and input power. The amplification gain was 5.1dB at the optimum magnetic field and input power. However, the coupling between magnetization and acoustic wave induced the energy change from surface wave to leaky bulk wave, thus increased the loss in the device.

The combination of high mobility of semiconductor heterojunction and strongly piezoelectric crystals provided promising hybrids for non-reciprocal devices with surface acoustic wave [34]. The nonlinear interaction between surface acoustic wave on lithium niobate substrate and the free carriers in a semiconductor quantum wall resulted in 13.2dB isolation of opposite SAW

propagation. However, the noise in the device was larger than that of passive devices because the introduction of electrons brought in noise.

Above efforts aiming at combining the concept of parametric amplification with the well-developed acoustic wave technologies have been conducted. However, the nonlinear coupling was either noisy or lossy, which impeded the applications. A method taking advantage of high quality factor of acoustic wave platform should be explored. The success of time varying transmission line implementation on the EM platform suggests the similar parametric mixing and amplification effects on the acoustic platform.

2.3 Analogy Between Electromagnetics and Acoustics

Mathematically there is a direct analogy between electromagnetic waves and acoustic waves. [35] Acoustic wave propagating in the piezoelectric material is analogous to electromagnetic wave propagating in the transmission line, as shown in Figure 2-5. Newton's Law and equation between strain and stress can be written in the similar form with telegrapher's equation:

$$\begin{cases} \frac{\partial \mathrm{T}}{\partial \mathrm{z}} = \rho \frac{\partial \mathrm{v}}{\partial \mathrm{t}} \\ \frac{\partial \mathrm{v}}{\partial \mathrm{z}} = \mathrm{s} \frac{\partial \mathrm{T}}{\partial \mathrm{t}} \end{cases} \tag{2.5}$$

$$\begin{cases} \frac{\partial \mathrm{V}}{\partial \mathrm{z}} = -\mathrm{L} \frac{\partial \mathrm{I}}{\partial \mathrm{t}} \\ \frac{\partial \mathrm{I}}{\partial \mathrm{z}} = -\mathrm{C} \frac{\partial \mathrm{V}}{\partial \mathrm{t}} \end{cases} \tag{2.6}$$

where voltage V, current I, inductance L, and capacitance C in microwave transmission lines is analogous to stress T, particle velocity v, mass density ρ, and compliance s (reciprocal of stiffness c) in acoustic wave waveguides, respectively. The mechanical counterpart in the acoustic wave waveguide derived from the transmission line is shown in the Table 2.1.

Mechanical compliance is of great interest because it is analogous to the capacitance that is pumped and modulated in the time varying transmission line.

Figure 2-5: (a)Acoustic Wave Waveguide (left) (b) Microwave Transmission Line (right).

Acoustic Waveguide	**Transmission line**
Stress: -T [N/m^2]	Voltage: V [v]
Velocity: v [m/s]	Current: I [A]
Density: ρ [Kg/m^3]	Inductance: L [H/m]
Compliance: s [1/Pa]	Capacitance: C [F/m]
Phase Velocity: $1/\sqrt{\boldsymbol{\rho s}}$ [m/s]	Phase Velocity: $1/\sqrt{\mathbf{LC}}$[m/s]
Characteristic Impedance: $\sqrt{(\boldsymbol{\rho/s})}$ [Kg/(m^2.s)]	Characteristic Impedance: $\sqrt{(\mathbf{L/C})}$ [ohm]

Table 2.1: Analogy between acoustic wave waveguides and transmission lines.

Therefore, the same parametric amplification concepts presented in time varying transmission line should also be presented in electro-acoustic platform such as acoustic wave devices. Moreover, acoustic devices will have substantial higher quality factor and smaller sizes than conventional electromagnetic devices due to the inherent low mechanical loss and the short acoustic wavelength at radio frequency. These electro-acoustic platforms can support coupling of acoustic waves across different frequencies using nonlinear piezoelectricity.

In this work, we focus on parametric modulation of acoustic wave using electric field dependent stiffness to couple the energy from electromagnetic wave to propagating acoustic wave. The nonlinear stiffness can be obtained by either material nonlinearity or structure nonlinearity, which will be demonstrated in the following chapter. The mechanical stiffness can be using the nonlinearity of materials, and it can also be tuned using geometrical nonlinearity.

Figure 2-6 shows our proposed nonlinear acoustic transmission line concept. Electric field dependent mechanical stiffness in acoustic transmission line, analogous to voltage dependent capacitors in electromagnetic time varying transmission line, can be exploited to create low-loss parametric amplification to the propagating acoustic waves. Such nonlinear stiffness results from the intrinsic nonlinear piezoelectricity in the material. Leveraging on distributed parametric modulation, acoustic nonlinear transmission line is utilized to accumulate the nonlinear effects thus creates a large output.

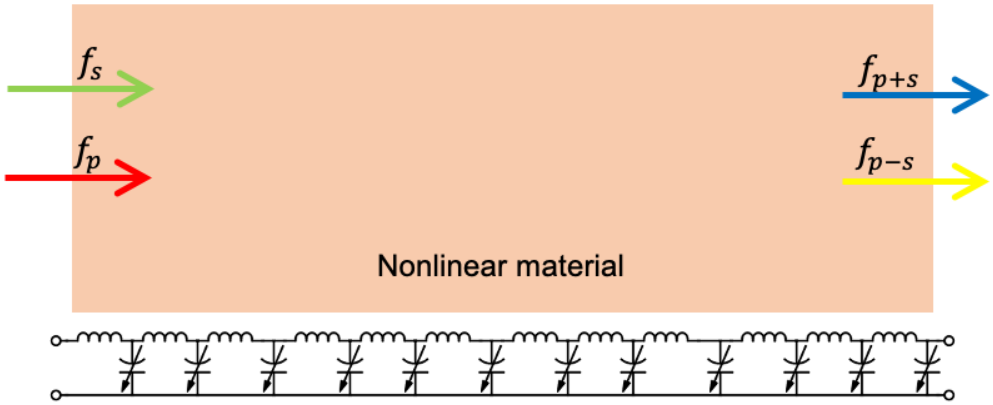

Figure 2-6: Proposed nonlinear acoustic transmission line concept.

By comparing the proposed concept to the past work, this concept takes advantage of high quality factor of acoustic wave for distributed effects, leverages on short wavelength of acoustic wave for device with small footprint, and explores nonlinear material that can achieve parametric amplification without using diodes. The proposed idea will yield a new class of active

acoustic devices providing orders of magnitude improvements in dramatically reduced sizes without degrading performance.

2.4 Proof of Nonlinear Acoustic Transmission Line Concept

The proposed nonlinear acoustic transmission line concept is proved using fully coupled finite element method simulation of surface acoustic wave delay line, with the solid understanding of time varying transmission line and the analogy between electromagnetics and acoustics. The proof of nonlinear acoustic transmission line idea leverages on the simulation effects of two-port surface acoustic delay line. The schematic of nonlinear acoustic transmission line simulation is shown in Figure 2-7.

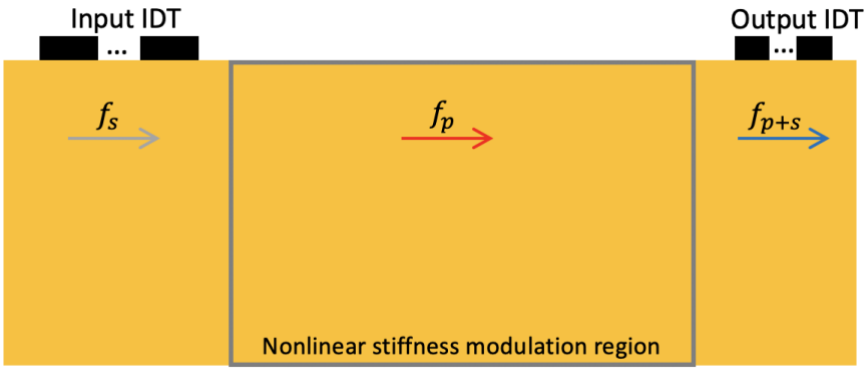

Figure 2-7: Schematic of two-port surface acoustic wave delay line setup to demonstrate the nonlinear acoustic transmission line concept. The middle region is the nonlinear stiffness modulation region where the mechanical stiffness is modulated as a function of time (f_p) and space.

The input interdigital transducers are designed at $f_s = 974MHz$ for exciting the signal surface acoustic wave. The output interdigital transducers are designed at $f_{p+s} = 2434MHz$ for detecting up-converted surface acoustic wave at this frequency. The middle region is the nonlinear stiffness modulation region which represents the nonlinear acoustic transmission

line. The length of the modulation region is $7\lambda_p$. Analogous to time varying transmission line, the mechanical stiffness of the modulation region is modulated by carrier electromagnetic wave which is $f_p = 1460MHz$ in this simulation. The modulation index is 0.1, implying the change of mechanical stiffness in this nonlinear modulation region is 0.1. The displacement of surface acoustic wave in this simulation at time step $2.054 \times 10^{-8}s$ is shown in Figure 2-8(a), with the parametric mixing phenomenon happening in the middle modulation region. The vertical layers in the middle modulation region introduce phase delay to the time varying mechanical stiffness, which contribute to the phase matching condition for parametric modulation between pump and surface acoustic wave. The surface acoustic waves of different wavelength are observed in and after the modulation region, which proves the nonlinear acoustic transmission line concept for demonstrating the parametric mixing effects. A reference two-port surface acoustic wave delay line is simulated where the parametric modulation region is removed. The displacement at the same time step $2.054 \times 10^{-8}s$ is shown in Figure 2-8(b), where the linear propagation of the signal acoustic wave is illustrated. The reference simulation proves that parametric mixing will not happen in the linear material.

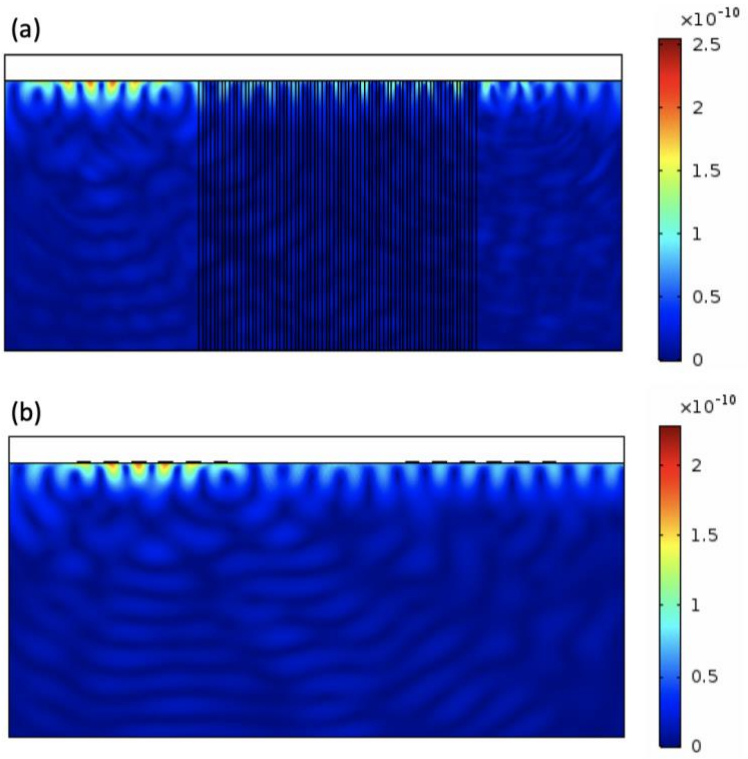

Figure 2-8: Displacement of the surface acoustic wave at time step 2.054×10^{-8}s in the delay line simulation (a) with nonlinear acoustic transmission line (b) without nonlinear acoustic transmission line. Parametric mixing effects is illustrated in (a) and proves the nonlinear acoustic transmission line concept.

To quantify the parametric mixing effects, the induced voltage on the interdigital transducers is plotted in time domain and analyzed in the frequency domain using Fast Fourier Transform as shown in Figure 2-9. Mixing effects are clearly observed in time domain signal as shown in Figure 2-9(a). Frequency domain analysis shows the magnitude of signal surface acoustic wave ($f_s = 974MHz$) and the up-converted surface acoustic wave $f_{p+s} = 2434MHz$, which further proves the parametric concepts using nonlinear acoustic transmission line.

Change of magnitude of up-converted surface acoustic wave is observed as the total length of nonlinear parametric modulation region varies. This change of magnitude corresponds of the

solution of time varying transmission line derived in equation 2.4.3. The induced voltage of the up-converted surface acoustic wave in frequency domain is shown in Figure 2-10, when the length of the nonlinear parametric modulation region is $9\lambda_p$ and $11\lambda_p$, respectively.

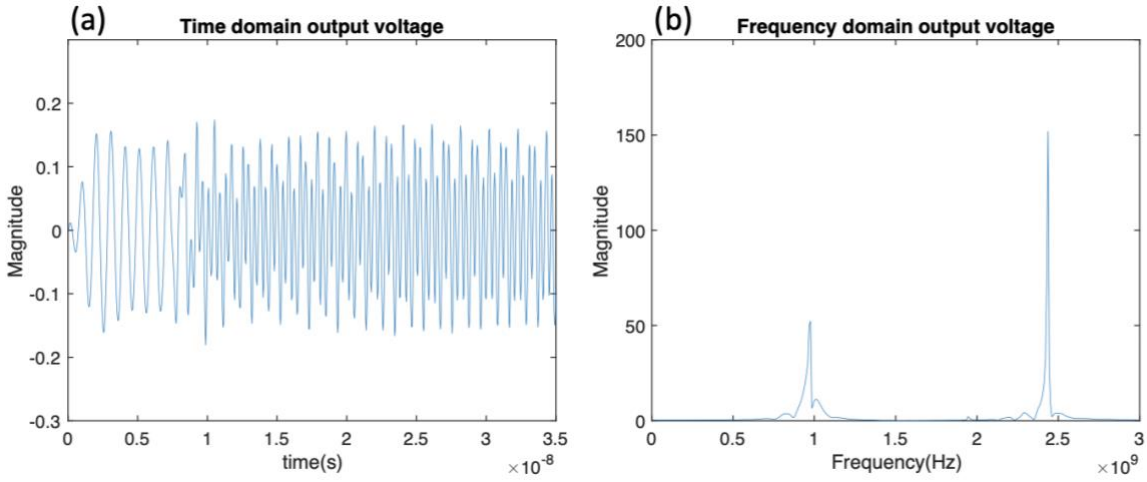

Figure 2-9: Output Voltage in (a)time domain and (b) frequency domain. Parametric mixing and frequency conversion are clearly observed.

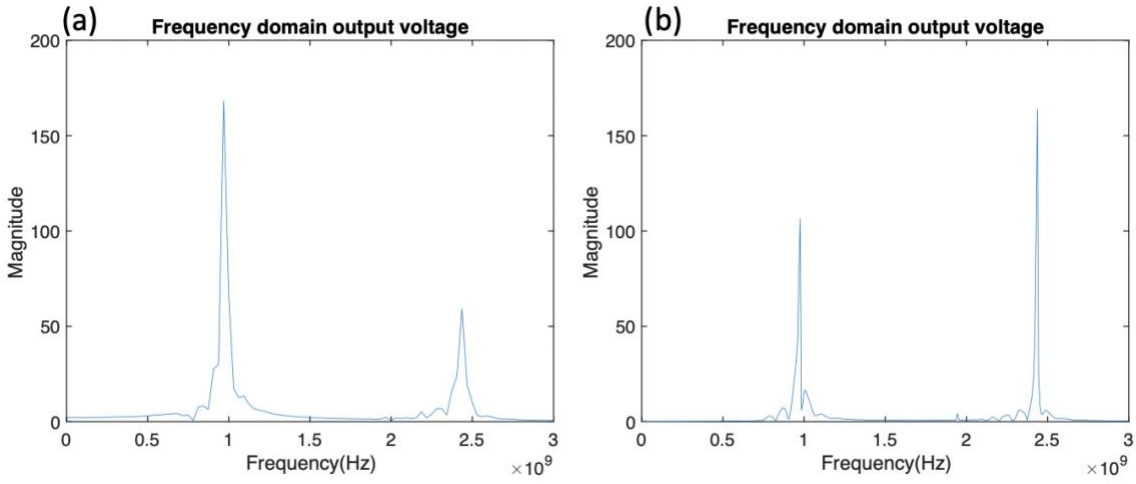

Figure 2-10: Output voltage in frequency domain with length of modulation region (a) $9\lambda_p$ (b) $11\lambda_p$.

The magnitudes of up-converted surface acoustic wave in simulation are compared with those in the theory of time varying transmission line, as shown in Figure 2-11. The magnitudes of up-converted surface acoustic wave show a sine curve with the length of the nonlinear acoustic modulation region, as predicted by the theory. The highest magnitude of the up-converted wave is achieved when length of the modulation region is $10\lambda_p$. The magnitude of the up-converted wave decreases as the length of the modulation region increases after $10\lambda_p$, as predicted by the sine function. The sine function for the up-converted wave and the cosine function for signal wave can be explained by the energy coupling between signal wave and up-converted wave. When the magnitude of the up-converted wave is at a maximum, the magnitude of the signal wave is at a minimum.

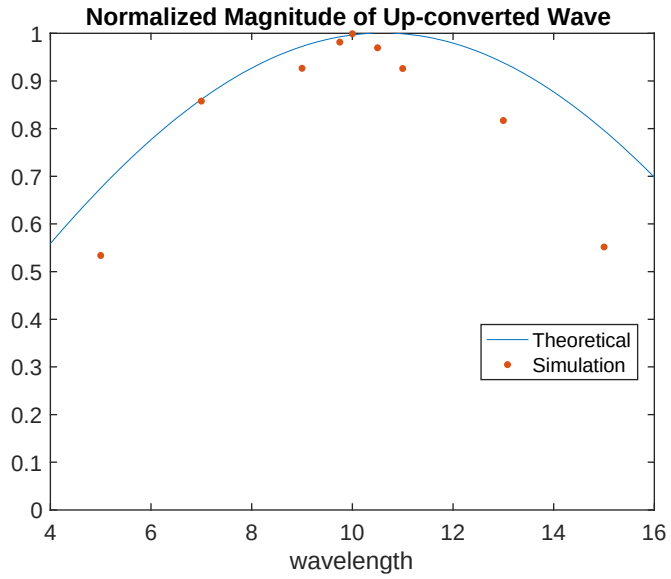

Figure 2-11: Normalized magnitude of up-converted surface acoustic wave vs length of the nonlinear acoustic modulation region in theory (blue curve) and simulation (red dot).

2.5 Conclusion

This chapter introduces an acoustic nonlinear transmission line concept to realize parametric effects on the acoustic platform. This proposed idea utilizes the analogy between electromagnetic waves and acoustic waves, i.e., mechanical compliance in the acoustic waveguide is analogous to the capacitance modulated in the time varying transmission line. Similar parametric mixing phenomenon happening in the time varying transmission line is expected to happen in the nonlinear acoustic waveguide where the mechanical stiffness is modulated by the pump wave and phase matched with the signal wave. The proposed idea is validated using fully coupled finite element method simulation of surface acoustic wave delay line and is matched with analytical equations derived for time varying transmission line.

Chapter 3 Parametric Mixing in Nonlinear Acoustics

In this chapter, practical implementations of acoustic nonlinear transmission line are discussed. Two nonlinear materials, barium strontium titanite (BST) and aluminum nitride (AlN) are introduced, and their nonlinear tuning ranges are explored. Nonlinear constitutive equations demonstrate the coupling concept of nonlinear permittivity to nonlinear mechanical stiffness. Parametric mixing and amplification are observed on the nonlinear acoustic transmission line implementation using BST, which proves the external permittivity coupling method. Besides, a three-port lamb wave delay line is fabricated to prove the nonlinear acoustic transmission line implementation using AlN. Parametric mixing is observed in experiment, and the nonlinear stiffness of AlN is extracted by the equivalent circuit model from experimental data. By comparing the nonlinear stiffness modulation at the same power level, nonlinear acoustic transmission line implementation using AlN is more optimal than that of BST for power efficient parametric mixing and amplification effects. Lastly, an alternative method to realize nonlinear mechanical stiffness by creating structure nonlinearity is introduced, for inspiring future works in this direction.

3.1 Introduction to Nonlinear Materials

The concept of acoustic nonlinear transmission line to realize parametric mixing and amplification is discussed and proved in the previous chapter. Acoustic nonlinear transmission is achieved by modulating the nonlinear mechanical stiffness of the material. However, the nonlinearity in the most piezoelectric materials is negligible and not sufficient to demonstrate the parametric effects. This includes the lithium niobate ($LiNbO_3$) which is used mostly in surface acoustic wave device. Fortunately, a newly researched nonlinear ferroelectric material, barium strontium titanite (BST), has demonstrated large permittivity tuning and has been widely used in used in varactors[36] and tunable thin film bulk acoustic wave resonator

applications [37]. Besides, A popular piezoelectric material for bulk acoustic wave devices and Lamb wave devices, aluminum nitride (AlN), has demonstrated 2.1% stiffness tuning by applying bias voltage [38]. The theory and simulation of nonlinear acoustic transmission line implementation using BST permittivity coupling are discussed in section 3.2 and 3.3. Parametric mixing and amplification effects are observed in BST coupled surface acoustic wave grating. Nonlinear acoustic transmission line implementation using AlN is discussed on section 3.5, with parametric mixing effects observed in AlN lamb wave delay line.

3.2 Nonlinear Constitutive Equation

The tunability of BST permittivity with applied dc voltage [36] is shown in Figure 3-1. The permittivity of BST can be tuned from 250 to 100 by bias electric field. The change of permittivity can be coupled to mechanical stiffness, which will be used in our proposed nonlinear acoustic transmission line implementation for parametric mixing and amplification application. The change of mechanical stiffness can be demonstrated and calculated by nonlinear coupling constitute equations. [6]

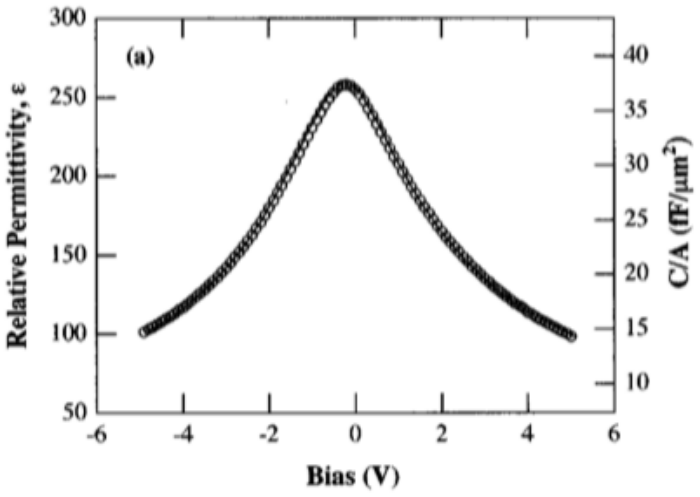

Figure 3-1: Relative permittivity as a function of applied dc voltage. Figure from [36].

The derivation of nonlinear constitutive equations is briefly summarized here. The derivation begins with Landau Theory Polarization Expansion appended with elastic energy and the energy of electrometrical coupling:

$$F = F_0 + \frac{\alpha}{2}P^2 + \frac{\beta}{4}P^4 + \frac{C}{2}S^4 - qP^2S - \frac{m}{2}P^2S^2 - PE \tag{3.1}$$

Here, F represents landau free-energy characterization of a ferroelectric, F_0 is independent of both polarization and strain, S represents strain. Using the relationship $E = \frac{\partial F}{\partial P}$ and $T = \frac{\partial F}{\partial S}$, the equations for electric field (E) and stress (T) are obtained:

$$E = \frac{\partial F}{\partial P} = \alpha P + \beta P^3 - 2qPS - mPS^2 \tag{3.2}$$

$$T = \frac{\partial F}{\partial S} = cS - qP^2 - mP^2S \tag{3.3}$$

Applying the initial state of ferroelectric matrial (E=E_{dc}, T=0), and neglecting the nonlinear electrostriction controlled by m, the relationship of E_{dc} and $S_{dc}$with polarization is written as:

$$E_{dc} = \alpha P_{dc} + \beta^* {P_{dc}}^3 \tag{3.4}$$

$$S_{dc} = q{P_{dc}}^2/c \tag{3.5}$$

where $\beta^* = \beta - 2q^2/c$.

Substituting dc component and ac component of the electric field, polarization, strain and stress into equation 3.4 and 3.5 and neglecting high-order ac terms, the nonlinear constitute coupling equations of E, P, S, T are obtained:

$$E = \left(\alpha + 3\beta^* {P_{dc}}^2\right)P - 2qP_{dc}S \tag{3.6}$$

$$T = -2qP_{dc}P + (C - m{P_{dc}}^2)S \tag{3.7}$$

Substituting P in equation 3.6 and 3.7 using $P = D - \varepsilon^b E$ and writing the nonlinear constitutive equations in the form of linear constitutive equations, the nonlinear constitutive equations can be written as:

$$D = eS + \varepsilon^S E \tag{3.8}$$

$$T = c^E S - eE \tag{3.9}$$

where

$$\varepsilon^S = \varepsilon^b + \chi_f \tag{3.10}$$

$$\chi_f = \frac{1}{\alpha + 3\beta^* {P_{dc}}^2} \tag{3.11}$$

$$e = 2\chi_f q P_{dc} \tag{3.12}$$

$$c^E = c - (m + 4q^2\chi_f){P_{dc}}^2 \tag{3.13}$$

Appying the common parameters of barium strontium titanite and tuning range of electric field to the above nonlinear constitutive equation, the stiffness (c^E) can be tuned by 4% with the electric field around $7*10^7 V/m$. The stiffness tuning of barium strontium titanite was also be observed and proved in the resonance frequency shifting of tunable thin film Bulk Acoustic Wave Resonator based on Barium Strontium Titanite thin film [37].

3.3 BST Coupled Nonlinear Acoustic Transmission Line

Although BST has not demonstrated any applications for travelling wave excitation and propagation, a novel way to realize acoustic nonlinear transmission line is to couple the

nonlinear permittivity to the mechanical stiffness of linear piezoelectric material like lithium niobate where surface acoustic wave has low propagation loss. As shown in Figure 3-2, BST thin film is flipped on the acoustic wave grating, and the electric displacement field in the BST will be coupled to the lithium niobate because of proximity effects, and the nonlinear permittivity that can change 60% as shown in Figure 3-1 can be coupled to the mechanical stiffness of lithium niobate, which will make the linear piezoelectric material nonlinear. In this way, composite nonlinear piezoelectric material is realized.

Zoomed in region of Figure 3-2 is the equivalent transmission line circuit model of the surface acoustic wave grating. The grating region is divided into the linear sections (i.e., with metal) and nonlinear sections (i.e., without metal). Linear surface acoustic wave grating region is represented by the ordinary transmission line model with inductors and capacitors. Nonlinear surface acoustic wave grating region is represented by the time varying transmission line model, as electrical field dependent stiffness is analogous to the voltage dependent varactors.

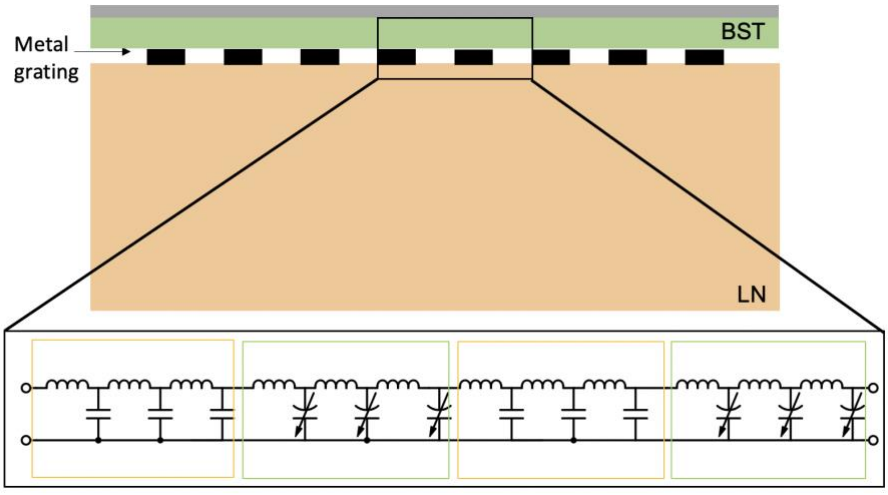

Figure 3-2: Nonlinear acoustic transmission line implementation. Zoomed in is the equivalent transmission line circuit model of the surface acoustic wave grating.

In this way, composite nonlinear piezoelectric material is realized. Tunability of mechanical stiffness of the proposed nonlinear acoustic transmission line implementation is estimated by the piezoelectric constitutive equation:

$$c^D = c^E + \frac{e^2}{\varepsilon} \tag{3.13}$$

where

$$\varepsilon = (\varepsilon_{BST} + \varepsilon_{LN})/2 \tag{3.14}$$

Theoretically, applying 30% permittivity change of the BST thin film to equation (3.13) can obtain 1.5% mechanical stiffness tunability using the configuration in Figure 3-2. Following simulations show that parametric mixing can be realized by this nonlinear acoustic transmission line implementation.

The method to implement nonlinear acoustic transmission line using BST and demonstrate parametric mixing is proved using fully coupled FEM simulation and equivalent circuit model. As shown in Figure 3-3, the equivalent circuit model is built based on the analogy of acoustic wave grating and transmission line, and it consists of two sections of periodic distributed transmission line. The parameters are different in the different transmission line section because acoustic wave will have different velocities under different boundary conditions (i.e., v_m for metal boundary and v_o for open boundary)[39].

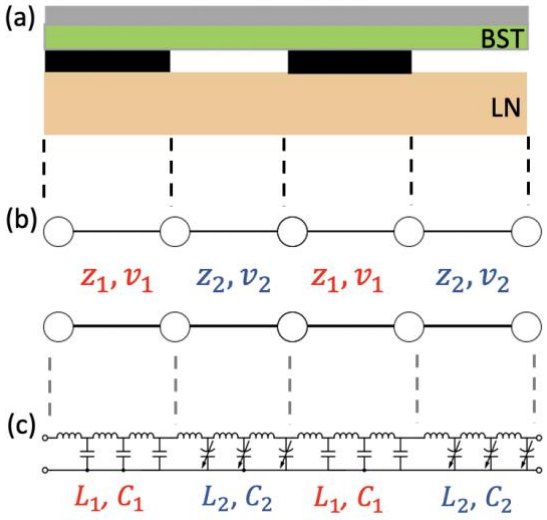

Figure 3-3: (a) Acoustic wave grating and its (b) linear equivalent circuit model and (c) nonlinear equivalent circuit model.

The ratio of characteristic impedance (Z_1, Z_2) and phase velocity (v_1, v_2) of two transmission line sections in the linear model is shown in equation (3.15) and (3.16). In circuit simulation, this ratio is realized by setting different dielectric permittivity of the substrate and physical dimension of the microstrip line.

$$\frac{Z_1}{Z_2} = \frac{v_m}{v_o} \tag{3.15}$$

$$\frac{v_1}{v_2} = \frac{v_m}{v_o} \tag{3.16}$$

For nonlinear simulation, the second microstrip line is replaced by a cascaded branch of series inductor L_2 and parallel varactor C_2, using equation (3.17) and (3.18). The capacitance change in the circuit model is equivalent with the mechanical stiffness change in nonlinear acoustic grating. Note the unit for L_2 and C_2 is H/m and F/m, respectively.

$$L_2 = \frac{Z_2}{v_2} \tag{3.17}$$

$$C_2 = \frac{1}{Z_2 v_2} \tag{3.18}$$

For the periodic structures above, similar passband and stopband phenomenon that exists in the periodic transmission model is expected to exist in the acoustic wave grating. Figure 3-4 shows the linear simulation results of both the FEM model and the circuit model. Similar passband and stopband are predicted by 30% BST permittivity change in FEM simulation (solid line) and by 0.8% capacitance change in equivalent circuit simulation (dashed line). This result matches with theoretical calculation in equation (3.13) and is used in the nonlinear simulation in the following part. The stopband phenomenon in the periodic grating can be used to terminate unwanted mixed frequency in the nonlinear configuration, and it will maximize the conversion at the desired mixed frequency. Periodic effects are also utilized in the periodically poled lithium niobate for optical parametric occilation[40-41], where the quasi-phase matching is implemented by a periodic modulation of the nonlinear susceptibility.

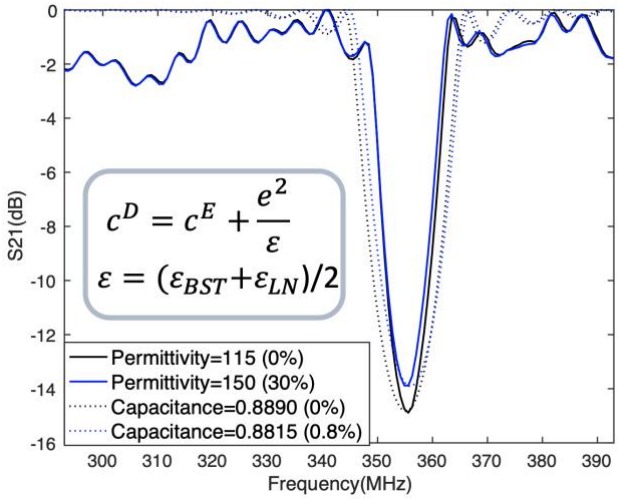

Figure 3-4: Acoustic wave grating using FEM simulation (solid line) and equivalent circuit simulation (dashed line). The inset shows a zoomed-in view at the stopband.

To simulate parametric effects, two surface acoustic waves at frequency f_s and f_p excited by two sets of input interdigital transducers (IDTs) are launched into the middle nonlinear grating whose total length is $10\lambda_p$. The simulation setup is shown in Figure 3-5. The thickness of metal is 250nm. The thickness of BST is 1500nm. The permittivity of BST is tuned by 30% by the normalized magnitude of electric field $|E|$ due to the symmetry of BST, and the nonlinearity will be coupled back to the signal acoustic wave, resulting in the parametric mixed frequencies in the output. This symmetry tuning rectifies the modulation frequency from f_p to f_{2p} and results in two sidebands at f_{2p-s} and f_{2p+s}.

The parametric mixing phenomenon is observed in the Fast Fourier Transform of the displacement at output probe, as shown in Figure 3-6 (solid line). Frequency domain analysis shows the signal surface acoustic wave ($f_s = 109MHz$), the up-converted surface acoustic wave ($f_{2p+s} = 495MHz$), and the down-converted surface acoustic wave ($f_{2p-s} = 277MHz$), which further proves the parametric mixing effects using BST implementation of nonlinear acoustic grating. Similar parametric effects are observed using equivalent circuit simulation as shown in Figure 3-6(dashed line). The slight discrepancy is due to the propagation loss of the SAW at high frequencies.

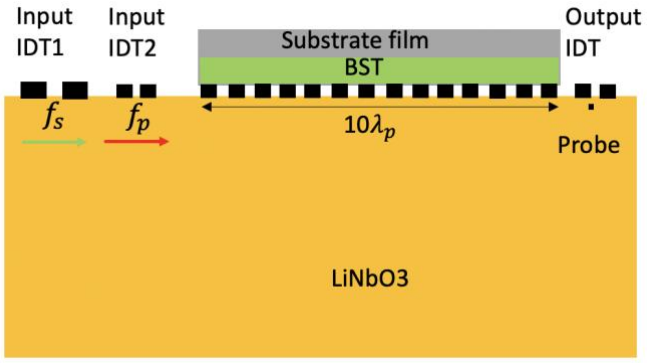

Figure 3-5: Simulation setup of nonlinear acoustic transmission line implementation using BST.

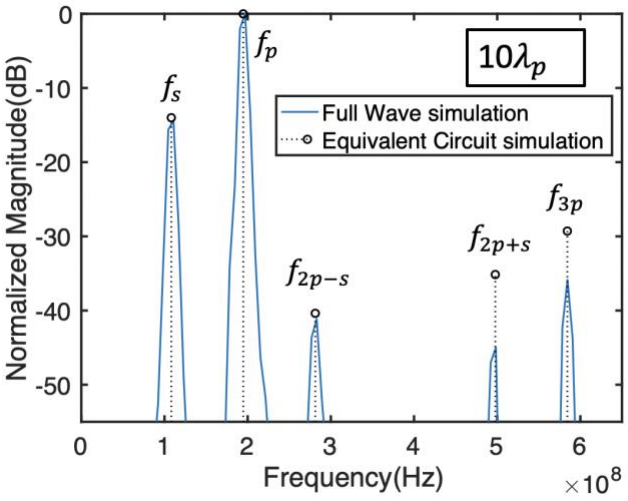

Figure 3-6: Parametric mixing of waves at output port in the full-wave simulation and equivalent circuit simulation. f_p is rectified to f_{2p} and results in two sidebands at f_{2p-s} and f_{2p+s}, because permittivity of BST is tuned by absolute value of electric field $|E|$.

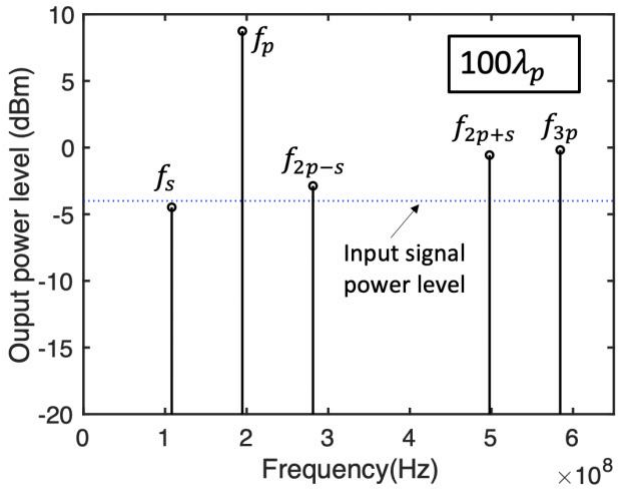

Figure 3-7: Parametric amplification realized in the converted side bands.

The reason we develop circuit model is that the circuit simulation is much more time-efficient than finite element simulation, and it supports simulation of arbitrary long structures. Figure 3-7 shows that parametric amplification is achieved if the nonlinear acoustic grating length is increased to $100\lambda_m$ and permittivity tunability of is increases to 50% (achievable in commercial BST thin film). The result proves that the proposed BST coupled nonlinear acoustic grating configuration has promise for realizing parametric amplification. This 100 λ_m grating configuration cannot be simulated using finite element simulation, because it takes too much computation resources and will have convergence issue. Therefore, the circuit model is a very powerful tool, and we use it for all the following simulations.

3.4 Parametric Mixing in AlN Lamb Wave Delay Lines

Surface acoustic wave and bulk acoustic wave have been widely studied for radio frequency filters, diplexers and antennas [42-43]. Recently the Lamb wave platform is under heat discussions and has triggered a lot of attention [44]. The Lamb wave technology has the following strengths: 1) lithographically defined resonance frequency, 2) CMOS circuit compatibility, 3) higher phase velocity (i.e., up to 10000 m/s for fundamental symmetrical Lamb mode S_0, which is very promising for high frequency operation). Besides, for the parametric mixing purpose in this work, the Lamb wave technology is very promising, because the Lamb wave can be excited in the AlN thin film where nonlinear mechanical stiffness is reported in literature, and it can be utilized for delay line applications. External nonlinearity coupling is not required if parametric mixing is demonstrated on the AlN Lamb wave platform.

Figure 3-8 (a) shows the schematic of A three-port lamb wave delay line. The propagation direction of Lamb wave is parallel to the surface of the AlN plate [45]. It is assumed that the lateral dimensions of the plate is large compared to its thickness and both surfaces are traction free, i.e., infinite extent in x and z direction and free surface boundary condition in y=0 and

y=H. Applying the conditions to the wave equation results in two sets of guided waves in the plate with symmetry and antisymmetry about its midplane, i.e., symmetric mode (S_0, S_1, S_2…) and antisymmetric mode (A_0, A_1, A_2…)[46]. In particular, when the wavelength of the propagating wave in the frequency of interests is long compared to the plate thickness H, as is the case for all the Lamb wave devices in this dissertation, the speed of the symmetric waves approaches the value c_p in the zero-frequency limit,

$$c_p = \sqrt{\frac{E_p}{\rho}} \tag{3.19}$$

where

$$E_p = \frac{E}{1-\nu^2} \tag{3.20}$$

E is the elastic modulus and ν is Poisson's ratio of the material. And the dispersion curve is almost flat for fundamental symmetric wave S_0 at low frequency (i.e., frequency interested in this work). The displacement components of the S_0 wave satisfies the condition:

$$\left|\frac{u_y}{u_x}\right| = o\left(\frac{\omega H}{v_p}\right) \tag{3.21}$$

ω is the frequency and H is the plate thickness.

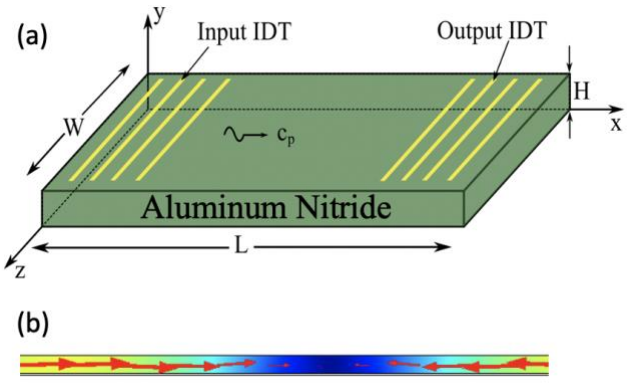

Figure 3-8: (a) Schematic and (b)fully coupled FEM simulation of a Lamb wave delay line built on AlN. The Lamb wave propagates from left to right. The color represents the magnitude of the displacement and the arrows represent the direction. Figures from[47].

Equation 3.21 implies that at relatively low frequencies, the wave is almost longitudinal, as shown in the S_0 Lamb mode displacement simulation in Figure 3-8(b). In fully coupled FEM simulation, the Lamb wave is launched and received using input IDTs (15 pairs) and output IDTs (15 pairs) made with 100nm Al. The thickness of AlN thin film is 400nm, which is much thinner than the Lamb wave acoustic wavelength (18.4um) at around 460MHz.

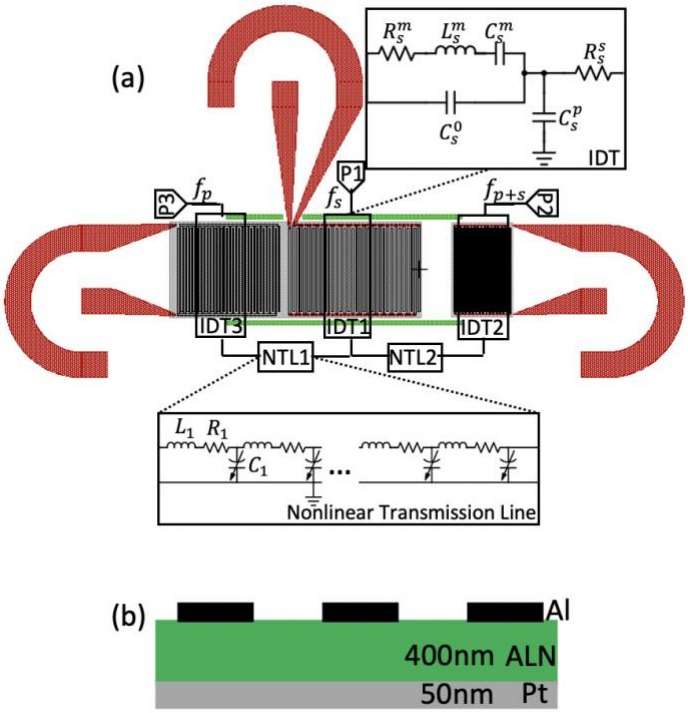

Figure 3-9: (a)Design of the parametric Lamb wave device and its equivalent circuit model. (b)Cross section of the interdigital transducers.

To demonstrate the parametric mixing on the Lamb wave platform, a three-port Lamb wave delay line[48] is designed as shown in Figure 3-9. The parametric mixing concept relies on two

Lamb waves propagating in the AlN thin film in the same direction. The two waves are a high-power pump Lamb wave at frequency f_p and a low-power signal Lamb wave at frequency f_s. The nonlinear mechanical stiffness is modulated by the propagating high-power pump Lamb wave, thus the signal wave is mixed up in frequency f_{p+s} and mixed down in frequency f_{p-s}. Three sets of interdigital transducers are used to excite pump Lamb wave (left IDTs, port 3), signal Lamb wave (middle IDTs, port 1), and receive up-converted Lamb wave (right IDTs, port 2), as shown in Figure 3-9(a). Each set of interdigital transducers has 34 finger pairs where each finger pair is composed of a signal finger and a ground finger. The width and spacing of each IDT finger are equal to a quarter of an acoustic wavelength. The wave speed of the Lamb wave here is approximately 8409 m/s.

The equivalent circuit model is also shown in Figure 3-9(a). For this model, each port is modeled as one modified Butterworth Van Dyke (mBVD) model [49]. The ports are labeled as P1 (frequency =f_s), P2 (frequency =f_{p+s}), P3 (frequency =f_p). The model for P1(frequency =f_s) is shown in the top right of Figure 3-9(a), where R_s^m, C_s^m, L_s^m represent the motional resistance, capacitance and inductance of the interdigital transducers respectively, and R_s^s, C_s^0, C_s^p represent the static resistance, IDT mutual capacitance, and parasitic capacitance respectively. The subscript s is used to represent the interdigital transducer set for signal frequency f_s. Same models are used for P2 (frequency =f_{p+s}) and P3 (frequency =f_p) and are not shown in the Figure 3-9(a). Three sets of interdigital transducers are connected through lossy transmission line labeled as NTL1 and NTL2. NTL1 and NTL2 are consists of cascaded branches of series inductor (L_1), resistor (R_1) and parallel nonlinear varactor (C_1). The number of branches is determined by the physical distance between each port, with 32 branches per acoustic wavelength. The inductor and capacitor values are determined by equation 3.17 and 3.18.

The cross section of the Lamb wave interdigital transducers is shown in Figure 3-9(b). The fabrication process of the Lamb wave delay line is brief summarized as follow: 1) starting with a blank (100) Si substrate with resistivity greater than 10 kΩ. cm; 2) 50nm patterned Pt was deposited; 3) 400nm AlN was sputtered; 4) vias was wet etched; 5) 100nm patterned Al was deposited; 6) release vents were reactive etched using cl2 based plasma; 7) the Lamb wave devices were released by an isotropic etch using XeF_2.

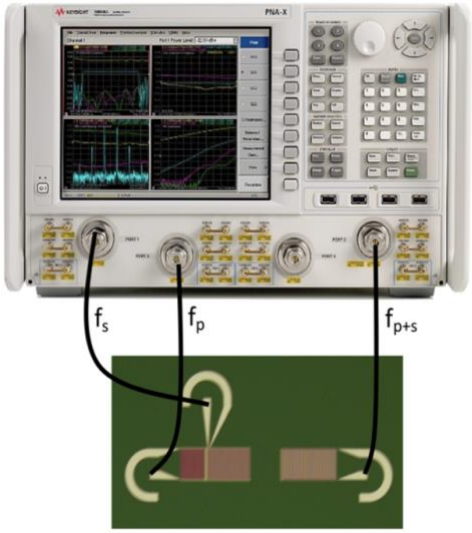

Figure 3-10: Lamb wave three port delay line under optical microscope and measurement setup.

Parametric effects by nonlinear stiffness of AlN thin film have been demonstrated in the Lamb wave device conversion gain measurement. The optical image of the fabricated Lamb wave delay line (before XeF_2 release) is shown in Figure 3-10. The Lamb wave device has three sets of IDTs which excite the signal Lamb wave at 460MHz (middle IDT), pump Lamb wave at 587MHz (left IDT), and receive up-converted Lamb wave at 1047MHz (right IDT), respectively. Each of the IDTs are connected to ground-signal-ground (GSG) pads with a 150um pitch. When the signal Lamb wave travels in the same direction with pump Lamb wave, the signal Lamb wave is modulated by the strong pump Lamb wave through the nonlinearity of AlN. This nonlinearity

results in mixing of the Lamb waves generated by parametric effects and the upconverted Lamb wave is picked up by the receiving port. The mixing performance is characterized using conversion factor (CF), which is the ratio of received upconverted power to the input signal power:

$$CF = 10log_{10}(P_{p+s}/P_s) \tag{3.22}$$

The Lamb wave devices are tested using the mixer mode of a vector network analyzer (VNA) as shown in Figure 3-10. The signal power is -10dBm and pump power varies from -5dBm to 5dBm. The conversion factor plot is obtained by sweeping the signal frequency from 440MHz to 480MHz.

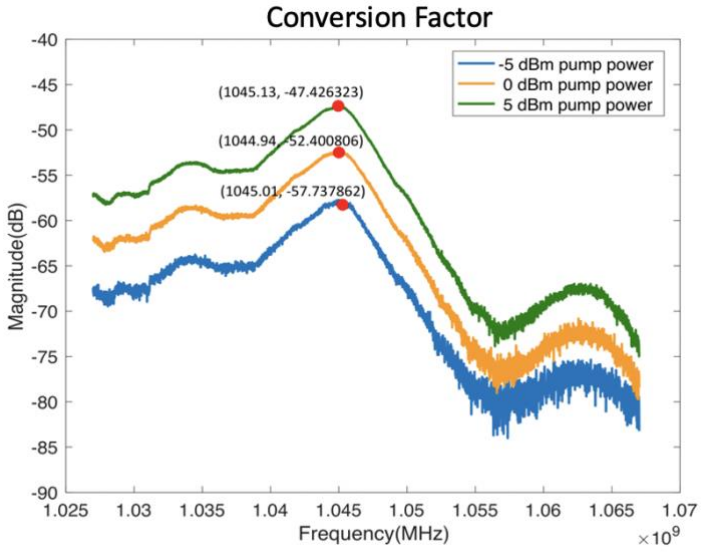

Figure 3-11 Conversion factor of the Lamb wave delay line for -5dBm, 0dBm and 5dBm power levels.

Conversion factor with pump powers of -5dBm, 0dBm and 5dBm are plotted in Figure 3-11. Conversion factor reaches -47dB when the pump power is 5dBm. The frequency conversion is caused by the nonlinear elastic compliance in the material, i.e., for a linear material frequency conversion would not happen and the conversion factor would just be the noise floor. This

experiment serves as proof of the nonlinearity in AlN thin films and demonstrates the parametric effects in Lamb wave devices. Since the fabricated Lamb wave devices do not have a resonator structure and do not accumulate the parametric effects, low conversion factor is expected. This experiment provides the evidence of the nonlinearity of AlN, in which the nonlinear mechanical stiffness modulation is extracted by the equivalent circuit model shown in Figure 3-9(a).

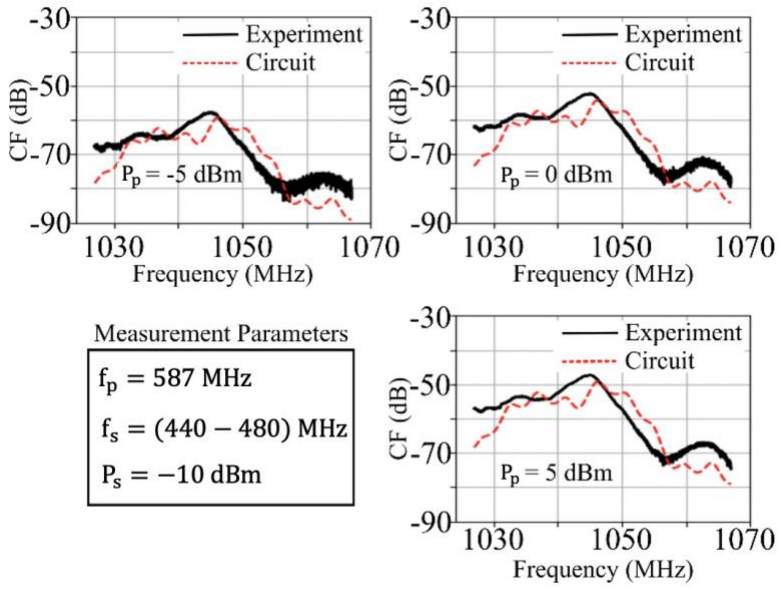

Figure 3-12: Simulated using equivalent circuit model (red dotted line) and measured (black solid line) conversion factor. Figures from [48].

Figure 3-12 shows the circuit model data with the experimental data. For the circuit model, the material's compliance modulation (ξ) is determined by fitting the circuit model to the experimental data. The circuit model shows similar trends to the experimental data for all three power levels. As the pump power increases from -5dBm to 0dBm and 5dBm, the conversion factor increases due to an increase in AlN compliance modulation. The increase in AlN nonlinearity contributes to more power conversion to the mixed frequency, i.e., the up-

converted frequency in this case. The slight discrepancy of the frequency response between circuit model and experimental data is caused by fabrication imperfections and device specific fluctuations that are not captured by the mBVD model.

The mechanical stiffness modulation of AlN nonlinear acoustic transmission line is larger than that of BST coupled nonlinear acoustic transmission line at the same power level. This is observed by comparing the circuit model nonlinearity of Figure 3-5 and Figure 3-9. The BST coupled nonlinear acoustic transmission line reports a 0.8% composite nonlinear stiffness which is achieved by 30% BST permittivity modulation under electric field of $1.5 \times 10^7 V/m$. Considering 2um grating width and 50 Ohm match, the required pumping power is approximately 40dBm. The required pump power for AlN nonlinear acoustic transmission line to achieve 0.8% stiffness modulation is 17dBm, which is extracted by circuit model from the experimental data. Therefore, AlN is a very promising material for demonstrating power-efficient nonlinear parametric mixing and amplification effects. A follow up work about parametric Q-enhancement on AlN Lamb wave resonator is included in Chapter 4.

3.5 Structure Nonlinearity Implementation

In this section, an alternative method to generate nonlinear mechanical stiffness is introduced. This method is realized by creating structure nonlinearity on the piezoelectric material. Specifically, this method proposes to dig holes on piezoelectric substrate to couple the parallel and perpendicular stiffness, therefore mechnical stiffess becomes a function of strain, and can be applied to couple the electromagnetic energy to the propagating acoustic wave energy. The schematic of structure nonlinearity is shown in Figure 3-13(a).

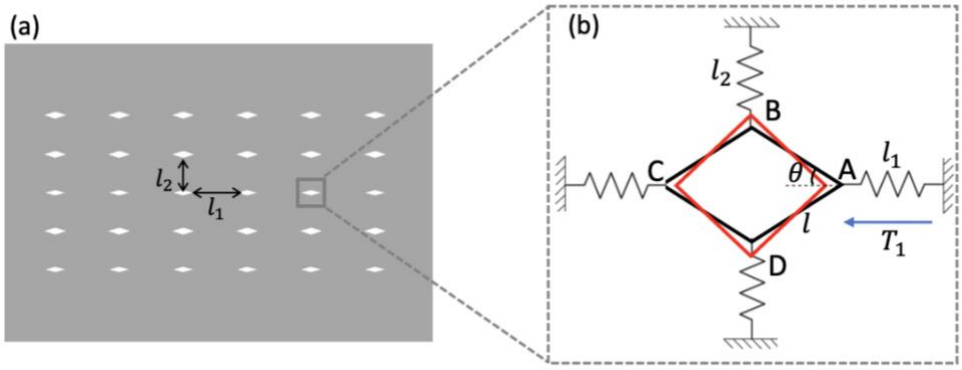

Figure 3-13: (a) Schematic of structure nonlinearity and (b) simplified rod and spring model.

To derive the nonlinearity of this structure, a simplified rod and spring model is developed to represent this nonlinear structure as shown in Figure 3-13(b). In this figure, black lines represent the original state of hole, and the red lines represent the state after applying stress T_1. The springs in the figure represent the surronding material, and the rods represent the edges of the hole.

The nonlinear mechanical stiffness is calculated by analyzing the force of A and B:

$$\begin{cases} T_1 - 2Tcos\theta = c_{11}S_1 \\ 2Tsin\theta = c_{22}S_2 \\ \Delta xcos\theta = S_1 l_1 cos\theta = S_2 l_2 sin\theta = \Delta ysin\theta \end{cases} \tag{3.23}$$

where T represents the stress on the rod between A and B, Δx represents the displacement of point A, Δy represents the displacement of point B, l_1 is the initial spring length of A, l_2 is the initial spring length of B, and θ represents the angle between rod and horizontal direction as shown in Figure 3-13(b), l is the length of the edge between A and B. The physical meaning of l_1 and l_2 is the distance between two nearby holes in the horizontal direction and vertical direction, respectively.

From equation 3.23, T_1 can be written as a function of S_1:

$$T_1 = (c_{11} + c_{22}\frac{l_1}{l_2}cot^2\theta)\, S_1 = c_{11}'S_1 \tag{3.24}$$

To find the equation of c_{11}' and S_1, θ is written as $\theta = \theta_0 + \Delta\theta$ and c_{11}' is expanded near θ_0. For simplicity, second and high order derivatives are neglected.

$$c_{11}' = \left(c_{11} + c_{22}\frac{l_1}{l_2}cot^2\theta_0\right) - \left(\frac{2c_{22}l_1 cos\theta_0}{l_2 sin^3\theta_0}\right)\Delta\theta \tag{3.25}$$

To find the relation between $\Delta\theta$ and S_1, following equations using geometrical relation can be derived with the assumption that $\Delta\theta$ is very small:

$$\Delta\theta = \frac{\Delta x}{l}\left(sin\theta_0 + \frac{cos\theta_0}{\tan(\theta_0+\Delta\theta)} + cos\theta_0\Delta\theta\right) \tag{3.26}$$

After linearizing the equation,

$$\Delta\theta = \frac{\Delta x}{lsin\theta_0} = \frac{S_1 l_1}{lsin\theta_0} \tag{3.27}$$

Finally, the nonlinear equation between stress(T) and strain(S) is derived:

$$T_1 = \left(c_{11} + c_{22}\frac{l_1}{l_2}cot^2\theta_0\right)S_1 - \left(\frac{2c_{22}{l_1}^2 cos\theta_0}{ll_2 sin^4\theta_0}\right){S_1}^2 \tag{3.28}$$

ξ can be defined as the modulation index to demonstrate the degree how the stiffness can be modulated:

$$\xi = \left(\frac{2c_{22}{l_1}^2 cos\theta_0}{ll_2 sin^4\theta_0}\right)/\left(c_{11} + c_{22}\frac{l_1}{l_2}cot^2\theta_0\right) \tag{3.29}$$

By substituting physical value of parameters in equation 3.29, the plots between modulation index ξ and strain S with different hole geometry and hole gaps can be generated.

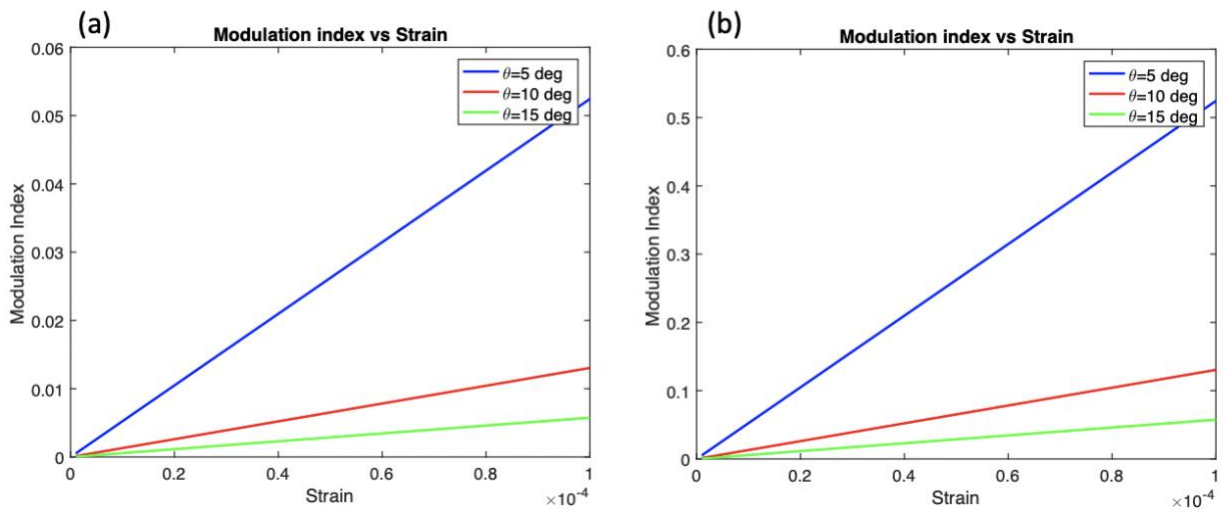

Figure 3-14 Plots of modulation index ξ vs strain S with different angles ($\theta = 5°, 10°, 15°$) and different hole sizes of (a) $l = 1.5um$ and (b) $l = 0.15um$. Hole separation l_1 and l_2 are set to 3um for all cases.

Figure 3-14 shows the modulation index ξ vs strain S with different angles ($\theta = 5°, 10°, 15°$) and different hole sizes of (a) $l = 1.5um$ and (b) $l = 0.15um$. Hole separation l_1 and l_2 are set to 3um for all cases. As shown in Figure 3-14 (a), the modulation index ξ is linearly proportional to strain S, i.e., the modulation index ξ increases as strain S increases. The slope for modulation index ξ vs strain S is different for holes with different angles. Hole geometry of $\theta = 5°$ (sharper angle) demonstrates a larger increasing slope than that of $\theta = 10°$, followed by than that of $\theta = 15°$. Figure 3-14(b) shows a similar trend of modulation index ξ vs strain S for different hole angles ($\theta = 5°, 10°, 15°$), i.e., geometry with sharper holes has larger modulation index ξ. Besides, by comparing Figure 3-14(a) and Figure 3-14(b), geometry with smaller holes provides larger modulation index ξ at the same strain S level and the same hole angle θ.

A conclusion can be drawn from mathematical simulations that material with sharper and smaller holes will provide larger modulation index ξ for acoustic parametric mixing and amplification. However, the criteria that limits the modulation index is the fabrication

resolution, i.e., small hole angle is hard to achieve when hole size is very small (ex, 1.5um for Figure 3-14(a)). This fabrication limitation prevents the device from obtaining large nonlinearity. The theoretical discussion and mathematical simulation of structural nonlinearity are included in this section, for inspiring future works of this direction.

3.6 Conclusion

In this chapter, practical implementations of acoustic nonlinear transmission line using nonlinear materials including BST and AlN are discussed. Nonlinear permittivity coupling to mechanical stiffness method is illustrated in nonlinear constitutive equations. This method is applied to BST coupled surface acoustic wave grating and parametric mixing and amplification are observed. Nonlinear acoustic transmission line implementation using AlN is proved on the Lamb wave platform. A three-port Lamb wave delay line is fabricated, and parametric mixing and frequency conversion have been observed. Comparing to BST implementation, AlN implementation demonstrates a higher nonlinear stiffness modulation than BST implementation and is more optimal for power efficient parametric mixing and amplification purpose. Moreover, another method to realize nonlinear stiffness (i.e., structure nonlinearity) is introduced and its limitation is discussed, for inspiring future works.

Chapter 4 Parametric Q-enhanced Acoustic Resonator

In this chapter, a non-degenerate phase independent parametric quality factor (Q)-enhancement technique is explored and demonstrated on AlN Lamb wave resonators. Unlike other active Q-enhancement techniques which require precise phase control of the electronic feedback loop, this technique is implemented by parametrically pumping AlN material stiffness to realize a negative resistance seen at the signal path. The negative resistance is dependent on the nonlinear material modulation and multi-resonance coupling in the device. A nonlinear circuit model is developed to simulate the parametric coupling of each resonance and extract the nonlinearity of AlN from experimental data. With proper pump frequency and pump power, the device quality factor is boosted in both simulation and experiment. The demonstrated Q-enhancement method is simple to implement and can be applied to other types of resonators that have nonlinear behavior and support multi-resonance operation.

4.1 Introduction to Q-enhancement

Acoustic wave resonators have been widely used for filters and diplexers in radio frequency mobile device front-ends due to their excellent performance (i.e., low insertion loss and high quality factor) and small footprint compared to their electronic counterparts [50-53]. The importance of acoustic duplexers is shown in chapter 1.1. They are used to isolate transmitting and receiving signals at closely spaced frequency bands and protect the receiver. The filter's performance depends on the quality factor.

Quality factor (Q) is a measure of loss of a resonant circuit, i.e., lower loss implies a higher Q. If the quality factor of the resonator degrades, the insertion loss of the filter made of resonators increases. Quality factor is defined as

$$Q = \omega \frac{average\ energy\ stored}{energy\ loss/second} = \omega \frac{W_m + W_e}{P_{loss}} \quad (4.1)$$

Among various acoustic wave devices, the Lamb wave resonator recently gained attention because it has both fundamental strengths of commercial surface acoustic wave (SAW) resonators and bulk acoustic wave (BAW) resonators: lithographically defined resonance frequency and CMOS circuit compatibility [54-55]. The fundamental Symmetric Lamb wave mode propagating in aluminum nitride (AlN) thin films exhibits a very high phase velocity of up to 10000 m/s, and thus supports higher frequency operation than the surface acoustic wave [49, 56-57]. However, for the center frequency considered in this work(>300MHz), Lamb wave resonator suffers from damping and Q degradation, mainly caused by large anchor loss [58-59].

It has been demonstrated that Q-enhancement methods can be applied to an acoustic resonator to boost the device's Q [60]. Passive Q-enhancement technique can be attained lithographically without adding to the power requirement to the system, however, it relies on the specific device geometry to reduce the energy leakage [61] or confine energy using periodically repeating mechanical structures [62]. Active-feedback Q-enhancement technique with external electronics can break the intrinsic fundamental limit of the material quality factor, but it requires precise gain and phase control [63-64] and may introduce additional noise. Parametric pumping is a technique for feeding energy into a dynamical system by modulating the reactive parameter of the system [65]. Degenerate parametric Q-enhancement has been studied extensively in low-frequency micromechanical resonator systems. It is achieved by modulating the spring constant at exactly twice the resonant frequency, and it requires precise in-phase condition between the pump and intrinsic resonance [66-69]. Non-degenerate parametric enhancement, on the other hand, is phase and frequency independent. However, significant efforts investigating acoustic parametric Q-enhancement for radio frequency above 300MHz have not been reported, as nonlinear compliance in most piezoelectric material is negligible for practical applications.

Recently researchers have reported observing frequency conversion [48, 70] in AlN Lamb wave devices. This suggests that AlN has the potential to demonstrate parametric Q-enhancement effects.

In this chapter, a non-degenerate phase independent parametric pumping technique is proposed to improve the Q of an AlN Lamb wave resonator. The proposed technique utilizes a negative resistance, which originates from the parametric amplification effect[10, 71] and has been recently applied in microwave LC resonators[72-73]. For Q-enhancement, the AlN's mechanical stiffness is modulated, thus realizing a negative resistance seen at the signal path. To reduce damping of the acoustic resonator, a Lamb wave resonator supporting harmonics operation has been designed, fabricated, and tested. A multi-resonance coupled nonlinear model is developed to simulate the parametric coupling of each resonance and extract the nonlinearity of AlN. Parametric mixing and Q-enhancement have been demonstrated both in the simulation and the experiment. This multi-resonance coupled nonlinear model and Q-enhancement technique can be applied to other types of resonators that have nonlinear behavior and support multi-resonance operation.

4.2 Operating Principles and Fabrication

Figure 4-1 shows the concept of negative resistance parametric Q-enhancement. The negative resistance technique has been recently applied in microwave LC resonators to achieve Q-enhancement. An in-depth mathematical derivation can be found in [73]. For simplicity, the three-wave mixing circuit model shown in Figure 4-1(a) is considered. Assume that only power at pump frequency (f_p), signal frequency (f_s) and idler frequency (f_{p-s}) can go in/out of the varactor (i.e., capacitor with a voltage tunable capacitance). Manley-Rowe relation[74]

$$\frac{P_s}{f_s} + \frac{P_p}{f_p} = 0 \tag{4.2a}$$

$$\frac{P_{p-s}}{f_{p-s}} + \frac{P_p}{f_p} = 0 \tag{4.2b}$$

predicts that when pump power (P_p is positive) is supplied to a nonlinear reactance $C(V)$, P_s and P_{p-s} will be negative. This indicates that pump power supplied to the nonlinear capacitance will deliver power to the signal path and thus, realize signal power gain. Voltage across the varactor can be written in the form of

$$V(t) = V_p \cos(\omega_p t) + V_s \cos(\omega_s t) + V_{p-s} \cos(\omega_{p-s} t), \tag{4.3}$$

where V_p, V_s, V_{p-s} is the voltage amplitude at pump frequency f_p, signal frequency f_s and idler frequency f_{p-s} respectively. LC tanks in the circuit (i.e., series combination of L_p and C_p, series combination of L_s and C_s, series combination of L_{p-s} and C_{p-s}) conceptually isolate signal power, pump power and idler power for each path. Specifically, when the nonlinear capacitance is modulated by the large pump power, (i.e., $V_p \gg V_s, V_{p-s}$), as in Figure 4-1(b), the capacitance variation can be approximated as

$$C(V) = C_0 + C_1 V(t) \approx C_0 + C_1 V_p \cos(\omega_p t) \triangleq C(t) = C_0 + 2\xi C_0 \cos(\omega_p t), \tag{4.4}$$

where ξ is the nonlinear modulation of the capacitance, C_0 is the static capacitance. The current flow into the nonlinear capacitor can be written in the form of

$$I = \frac{d}{dt}[C(t).V(t)]$$

$$= \frac{d}{dt}[\left(C_0 + \xi C_0\left(e^{j\omega_p t} + e^{-j\omega_p t}\right)\right).(V_s e^{j\omega_s t} + {V_s}^* e^{-j\omega_s t} + V_{p-s} e^{j\omega_{p-s} t} + {V_{p-s}}^* e^{-j\omega_{p-s} t})]$$

$$= I_s e^{j\omega_s t} + {I_s}^* e^{-j\omega_s t} + I_{p-s} e^{j\omega_{p-s} t} + {I_{p-s}}^* e^{-j\omega_{p-s} t} \tag{4.5}$$

By picking the $e^{j\omega_s t}$ term and the $e^{-j\omega_{p-s} t}$ term, a small-signal admittance matric can be written in the form of

$$\begin{bmatrix} I_s \\ {I_{p-s}}^* \end{bmatrix} = \begin{bmatrix} j\omega_s C_0 & j\omega_s \xi C_0 \\ -j\omega_{p-s}\xi C_0 & -j\omega_{p-s} C_0 \end{bmatrix} \begin{bmatrix} V_s \\ {V_{p-s}}^* \end{bmatrix} \tag{4.6}$$

By eliminating both ${I_{p-s}}^*$ and ${V_{p-s}}^*$, the equivalent admittance of the nonlinear capacitor at signal frequency f_s is given as

$$Y_{var} = \frac{I_s}{V_s} = j\omega_s C_0 - \frac{\omega_s \omega_{p-s} \xi^2 C_0^2}{Y_{p-s}^* - j\omega_{p-s} C_0}, \tag{4.7}$$

where Y_{p-s} is the admittance of the idler path (the series combination L_{p-s}, C_{p-s} and R_{p-s} in Figure 4-1(b)) and can be written in the form of $Y_{p-s} = G_{p-s} + jB_{p-s}$ (i.e., a real valued conductance G_{p-s} in parallel with a susceptance B_{p-s}) through series circuit to parallel circuit conversion. Note that the term $Y_{p-s}^* - j\omega_{p-s} C_0$ is equal to G_{p-s} when Y_{p-s}^* is made to resonate with C_0 at f_{p-s}. G_{p-s} accounts for the resonator loss at f_{p-s} due to finite quality factor Q_{p-s} and can be expressed as $G_{p-s} = \omega_{p-s} C_0 / Q_{p-s}$. Thus, in the view of signal frequency f_s, the equivalent circuit becomes Figure 4-1(c). The signal path sees a negative conductance G in parallel with a normal capacitor C_0, which reduces the loss of signal resonator and enhances the quality factor. The negative conductance G can be written in the form of

$$G = -\frac{\omega_s \omega_{p-s} \xi^2 C_0^2}{G_{p-s}} = -\omega_s \xi^2 C_0 Q_{p-s}\,. \tag{4.8}$$

The negative conductance G can be further normalized by the signal conductance G_s, where G_s represents signal resonator loss at f_s and can be expressed as $G_s = \omega_s C_0 / Q_s$. Note that G_s and G_{p-s} in this derivation are not the inverse of R_s and R_{p-s}. G_s represents the parallel conductance of a parallel resonant circuit [74] and should be obtained through series to parallel conversion of the signal path. The normalized negative conductance G/G_s thus becomes

$$\frac{G}{G_S} = -\frac{\omega_s \xi^2 C_0 Q_{p-s}}{G_S} = -\xi^2 Q_s Q_{p-s}\,. \tag{4.9}$$

where Q_s and Q_{p-s} represent the quality factor of the signal resonance and the idler resonance, respectively. This proves that the normalized negative conductance is proportional to ξ^2, Q_s and Q_{p-s}. The negative-resistance Q-enhancement concept is equivalent to the Q-enhancement in the mechanical system shown in Figure 4-1(d), where the damping is reduced by the negative resistance technique. In summary, this technique is subject to the following conditions: 1) the nonlinear capacitor is shared by signal, pump, idler path, and is modulated by large pump power, 2) the idler path is in resonance with the static capacitance at the idler frequency f_{p-s}.

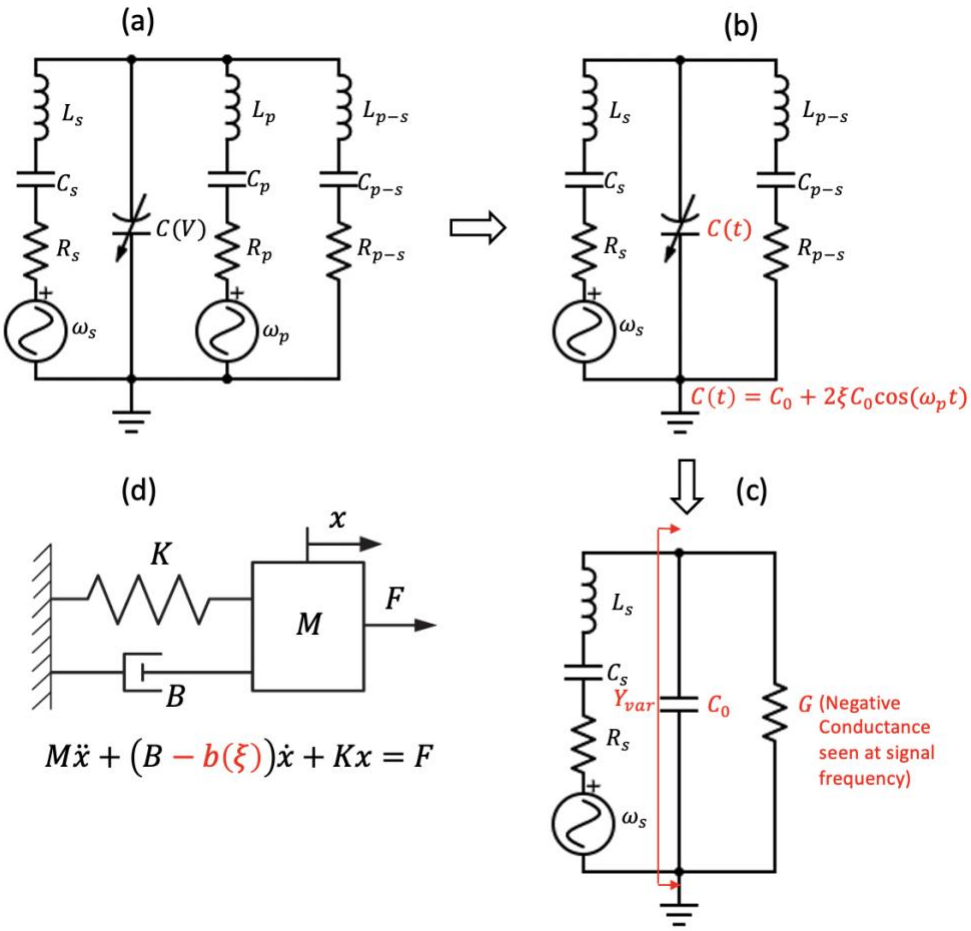

Figure 4-1: Negative-resistance Parametric Q-enhancement concept. (a) Three-wave mixing circuit model, (b) time-varying and parametric pumped nonlinear capacitor, (c) the negative conductance seen at the

signal frequency, (d) analogy of signal path to a mechanical system with reduced damping. M is the mass of the system, B is damping, K is stiffness.

Acoustic waves are analogous to electromagnetic waves[75]. Capacitance in electromagnetic waves is analogous to mechanical compliance (reciprocal of mechanical stiffness) in acoustic waves. Therefore, nonlinear mechanical stiffness in an acoustic material, like AlN, is analogous to a varactor in the resonator model, and can be exploited to create parametric Q-enhancement behavior shown in LC resonators. Figure 4-2 shows the two-port Lamb wave resonator designed for demonstrating the parametric effects. 400 nm AlN film is used because the thickness is much shorter than operating wavelength of the resonator (18.4 μm), therefore the first order symmetric mode (S_0) is the primary operating mode in the resonator [56] and it has a higher phase velocity compared to that in thicker AlN film. Higher harmonics like the 2^{nd} and 3^{rd} harmonic of the S_0 mode (frequency equal to, or close to if dispersive, twice and triple of the fundamental mode resonance) are also supported in the resonator. The parametric Q-enhancement concept relies on coupling the signal resonance (fundamental mode resonance) and the idler resonance (2^{nd}-order mode resonance). When the pump power P_p induces a time varying nonlinear mechanical compliance in AlN, signal power P_s and idler power P_{p-s} are coupled by the parametrically pumped compliance. Because the idler is at resonance, the signal path sees a negative conductance, which enhances the quality factor of the signal resonance. To launch signal power and pump power, two sets of interdigitated transducers (IDTs) (34 fingers each) with the grounded bottom electrode convert electrical energy into acoustic energy and, conversely, acoustic energy into electrical energy through the piezoelectric effect. As shown in Figure 4-2(a), the upper set of IDTs (in blue) is responsible for exciting the signal resonance at f_s, the lower set of IDTs (in green) feeds the pump power at f_p.

Figure 4-2(b) shows the zoomed in IDT cross section and the schematic of the coupled multi-resonance model. Each circuit element is the parallel combination of all sub elements that appear between the top metal fingers and the bottom electrode. The coupled multi-resonance model is built based on transmission line theory[74]. Acoustic wave propagation in a piezoelectric material is analogous to EM wave propagation in a transmission line waveguide, which can be modeled as cascaded sections of series inductors (L_{m1}, L_{m2} , L_{m3}…) and parallel capacitors (C_{m1}, C_{m2} , C_{m3}…). Acoustic wave resonators have edge reflectors that can be modeled as open boundaries to the transmission line model. Series resistors (R_{m1}, R_{m2} , R_{m3}…) are added to the model to represent the loss of resonance. When only one resonance is of interest, this multi-resonance model can be degenerated to the mBVD (modified Butterworth Van Dyke) model [50, 76] by keeping only one section of resistor (R_{m1}), inductor (L_{m1}) and capacitor (C_{m1}). Capacitance between the IDT fingers (C_0), static resistance (R_s) and capacitance between top IDT and bottom grounded electrode (C_p) are included in the model. For nonlinear simulation, capacitors are replaced by varactors to represent the nonlinearity of AlN. Circuit parameters of the coupled multi-resonance model can be found in the next subsection.

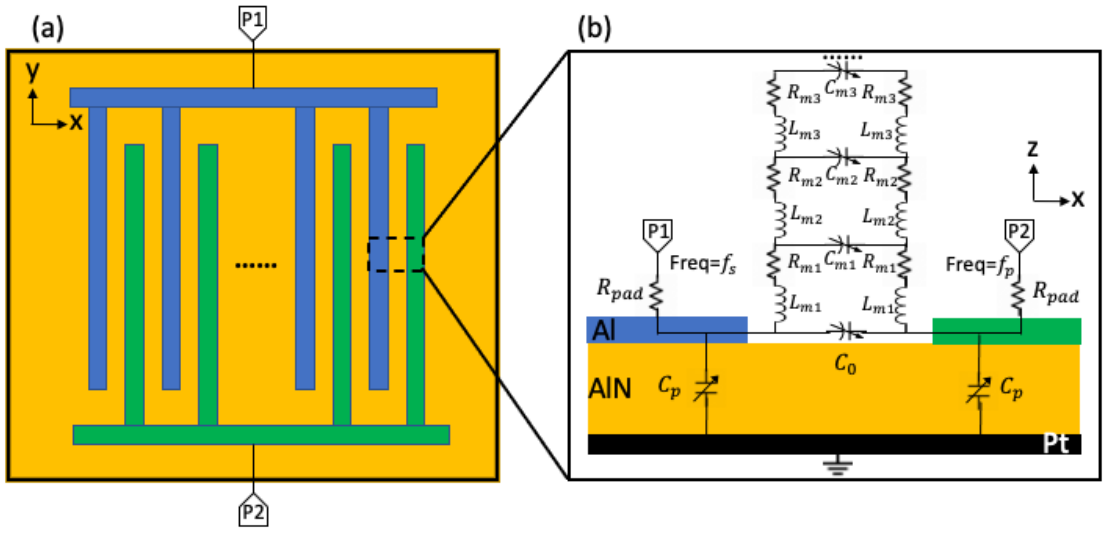

Figure 4-2: Lamb wave resonator. (a) Top view of the resonator design, (b) zoomed in IDTs cross sectional view and coupled multi-resonance circuit model overlaying the device.

The fabrication process of the Lamb wave resonator is shown in Figure 4-3 and is as follows: (1) deposit patterned 50 nm platinum (Pt) as the bottom electrode on the Si wafer with resistivity greater than 10 kΩ. cm; (2) deposit 400 nm of AlN; (3) wet etch the vias and deposit 100 nm patterned Al as the IDTs; (4) plasma etch the release vents and release the resonator by a XeF_2 isotropic etch. Fabrication details can be found in appendix of ref[77].

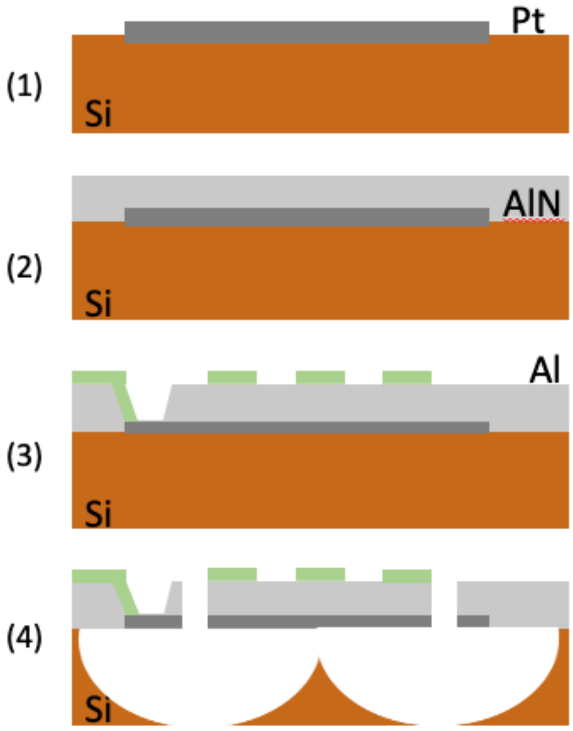

Figure 4-3: Fabrication diagram for the Lamb wave resonators.

Figure 4-4(a) shows an optical image of the fabricated Lamb wave resonator. The blue area under the IDTs is where the Si has been etched. Slotted release vents are applied to support a wider resonator, which allow for more IDT fingers to lower the motional resistance R_m. Lowered

R_m makes the resonator easy to be integrated with existing 50 Ω systems. However, slotted release vents increase the number of anchors in the resonator to 30. Multiple anchors result in insufficient confinement in the anchor direction and greatly increase the anchor loss and spurious modes. Figure 4-4(b) shows the zoomed in dashed region of Figure 4-4(a), with the IDT dimensions labeled. The IDT width (4.6 μm) is designed based on the fundamental mode signal resonance frequency (467 MHz) and wave speed of the device (approximately 8574 m/s). Each set of the IDTs is connected to three pads designed for ground-signal-ground (GSG) probes with 150 μm pitch.

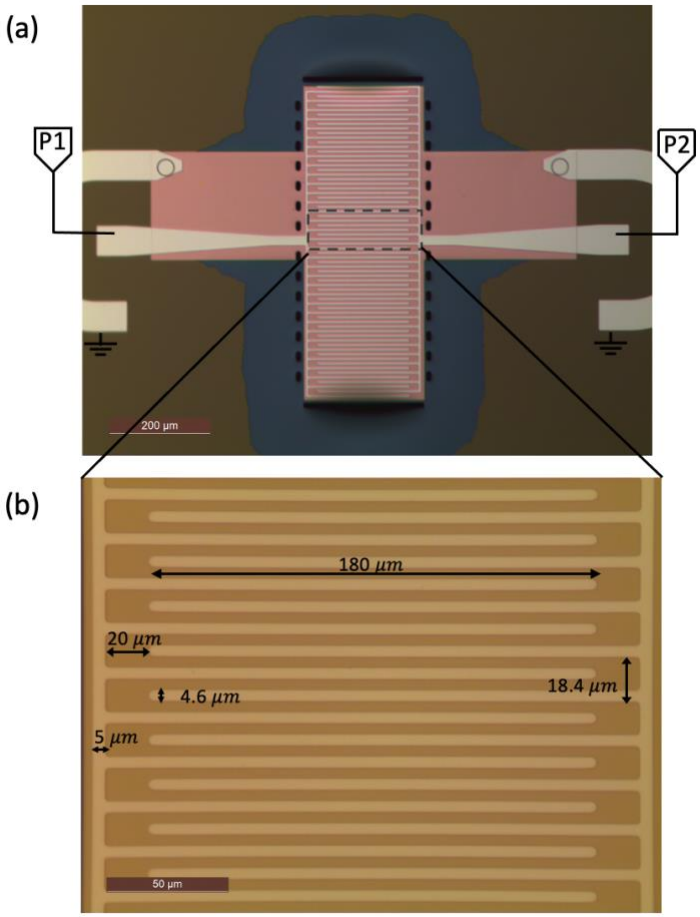

Figure 4-4: (a) Optical image of the Lamb wave devices after fabrication. The blue area under the IDTs is where the Si has been etched. (b) Zoomed in dashed region of (a) with IDT dimensions.

4.3 Multi-resonance Coupled Circuit model

The complete nonlinear multi-resonance coupled circuit model is shown in Figure 4-5. This multi-resonance model is built based on the mBVD model for Lamb wave device and transmission line resonator model. For mBVD model, it has been used in the Lamb wave delay line model in the chapter 3 and corelated well with experiment data. For the transmission line resonator model, acoustic wave propagation can be modeled by transmission line, therefore the acoustic resonator with edge reflector can be modeled as open boundary to the transmission line model. Ideally the transmission line resonator model can simulate infinite number of resonances. In our model three branches of the transmission line model is kept, as first three resonances are of great interests. To combine the transmission line resonator with the mBVD model, the motional arm in the mBVD model is cascaded into three sections and matched with the dispersive behavior in the resonator. The multi-resonance coupled model can be degenerated to the mBVD model if only one resonance is interested. The motional inductor (L_m), capacitor (C_m) and resistor (R_m) of the 1^{st} resonance and the capacitor between top IDT and bottom grounded electrode (C_p) are calculated using the equations from two port mBVD model [50, 76]:

$$\mathrm{C_p} = \mathrm{n}\varepsilon_{33}\varepsilon_0 \frac{\mathrm{WL}}{\mathrm{T}} \tag{4.10a}$$

$$R_m = \frac{\pi^2}{4}\frac{1}{\omega_s k_t^2 Q}\frac{1}{C_p} \tag{4.10b}$$

$$L_m = \frac{\pi^2}{4}\frac{1}{\omega_s^2 k_t^2}\frac{1}{C_p} \tag{4.10c}$$

$$C_m = \frac{4}{\pi^2}k_t^2 C_p \tag{4.10d}$$

where L, W and T refer to the length, width, and thickness of each IDT finger; n is the number of fingers; ε_{33} is the AlN material relative dielectric constant; ω_s is the device resonance frequency; Q is the quality factor at the resonance frequency; k_t^2 is the equivalent electromechanical coupling coefficient for AlN.

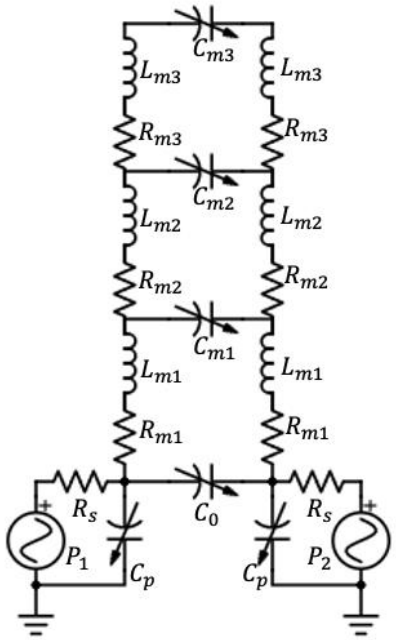

Figure 4-5: Complete nonlinear multi-resonance coupled circuit model for Lamb wave resonator.

L_{m1}	C_{m1}	R_{m1}	L_{m2}	C_{m2}	R_{m2}	L_{m3}	C_{m3}	R_{m3}	C_0	C_p	R_s
0.2 uH	79.8 fF	5.9 Ω	0.8 uH	21.9 fF	16.4 Ω	1.0 uH	19.1 fF	0.8 Ω	0.3 pF	9 pF	24.5 Ω

Table 4.1: Circuit parameters for the Lamb wave multi-resonance coupled model.

The motional inductor (L_m), capacitor (C_m) and resistor (R_m) of the 1^{st} resonance are then cascaded into three sections ($L_{m1}, C_{m1}, R_{m1}; L_{m2}, C_{m2}, R_{m2}; L_{m3}, C_{m3}, R_{m3}$) to form three resonances. These parameters are optimized to capture the dispersive behavior (harmonic frequencies shifting behavior) in the linear S-parameter experiment. The resonance frequency of each resonance in the linear circuit model is essential, as the entire linear circuit model is

directly applied to nonlinear simulations for parametric mixing and parametric Q-enhancement. Slight off in the frequency of each resonance between S-parameter simulation and experiment will result in mismatch of nonlinear behaviors. The feedthrough capacitor (C_0) and the static resistance (R_s) are determined by experimental data. The nonlinear capacitors change capacitance based on the AlN material compliance modulation (ξ), which is extracted from parametric mixing experiment. Table 4.1 shows the detailed circuit parameters for the Lamb wave multi-resonance coupled model.

4.4 Parametric Q-Enhancement and Discussion

The Lamb wave resonator was first tested linearly by connecting P1 and P2 of the device to the ports of the vector network analyzer (VNA). S-parameters were measured to obtain the precise frequency of the 1^{st} resonance and 2^{nd} resonance. The linear measurement is essential for determining the pump frequency in the Q-enhancement measurement, in order to satisfy the frequency relation and idler resonance requirement.

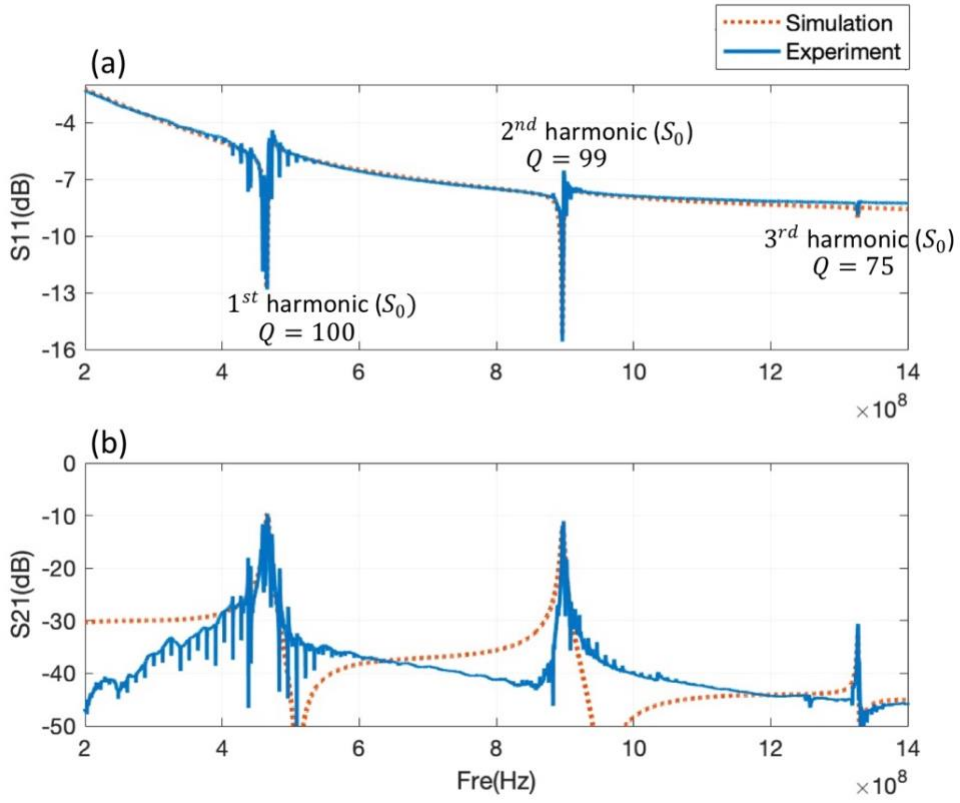

Figure 4-6: Magnitude of S parameter (a) reflection coefficient and (b) insertion loss for the Lamb wave resonator linear measurement. The blue solid line is the measurement result, and the red dashed line is from the circuit model.

Figure 4-6 shows the experimental (solid blue line) and circuit simulated (dashed red line) magnitude of the (a) reflection coefficient and the (b) insertion loss in the Lamb wave resonator for the 1^{st}, 2^{nd} and 3^{rd} resonance. The multi-resonance coupled circuit model agrees well with the experimental result, especially for the range of the resonance frequency. The dip in the reflection coefficient represents the frequency that the least amount of power is reflected back to the VNA. The peak in the insertion loss represents the frequency that maximum amount of power is delivered to from P1 to P2. The 1^{st} resonance has a minimum insertion loss of 10 dB at 467 MHz and serves as the signal resonance f_s. The 2^{nd} resonance has a minimum insertion loss of 11 dB at 897 MHz and serves as the idler resonance f_{p-s}. Ideally, if the 2^{nd} resonance f_{p-s} lies

exactly at twice of the 1^{st} resonance f_s, pump frequency f_p will lie at 3^{rd} resonance. This is optimal because insertion loss is the lowest at resonance (i.e., more pump power can go into the device). However, because of dispersion, the pump frequency ($f_p = f_s + f_{p-s}$ = 1364 MHz) is off from 3^{rd} resonance (1327 MHz) and has 45 dB of insertion loss. The insertion loss at f_p sets the requirement for high pump power in the Q-enhancement measurement.

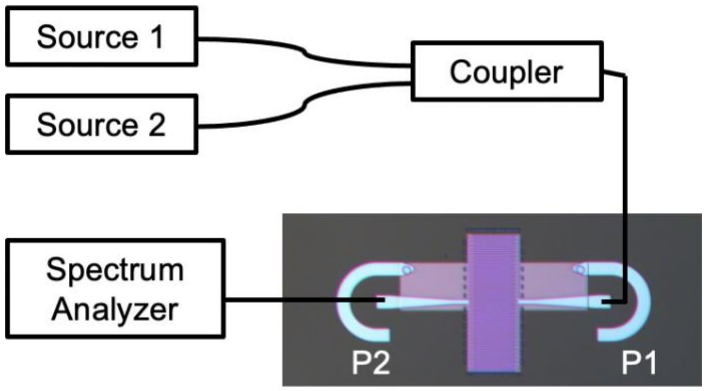

Figure 4-7: Setup of parametric frequency mixing measurement.

The parametric frequency mixing experiment was conducted using a spectrum analyzer, two signal sources and a coupler. The experimental setup is shown in the Figure 4-7. The purpose of this experiment is to demonstrate the nonlinearity of the device and extract the nonlinear coefficient for the circuit model. The signal power P_s at 467 MHz and the pump power P_p at 1364 MHz were generated from two signal sources, combined by a directional coupler, and fed together into port 1 of the resonator. Port 2 of the resonator was connected to a spectrum analyzer to observe output frequencies from the resonator. Resolution bandwidth of the spectrum analyzer is set to 1.3 kHz to lower the noise level.

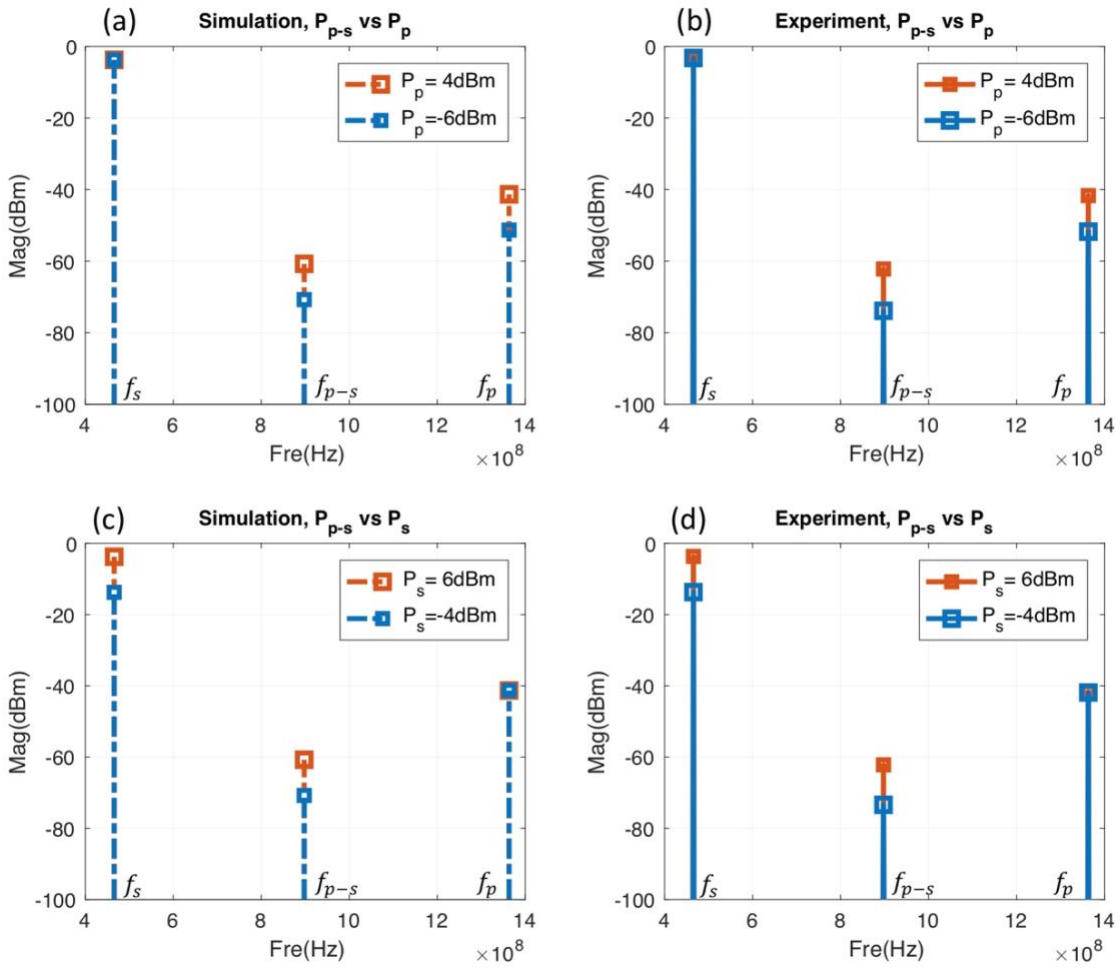

Figure 4-8: Parametric frequency mixing results. (a) Simulation and (b) measurement results of mixing power P_{p-s} vs different pump power (P_p = -6 dBm and P_p = 4 dBm), signal power P_s is fixed at 6 dBm. (c) Simulation and (d) measurement results of mixing power P_{p-s} vs different signal power (P_s = -4 dBm and P_s = 6 dBm), pump power P_p is fixed at 4 dBm.

Figure 4-8 shows experimental (right) and simulation(left) data of parametric frequency mixing phenomenon in the Lamb wave resonator. The frequency mixing is caused by nonlinear compliance in the AlN, i.e., frequency mixing would not occur in a linear material. The data presented in Figure 4-8(a)-Figure 4-8(b) shows the mixing power P_{p-s} vs two different pump powers P_p = -6 dBm, 4 dBm when the signal power P_s is fixed at 6 dBm while Figure 4-8(c)-Figure 4-8(d) shows the mixing power P_{p-s} vs two different signal powers $P_s = -4$ dBm, 6 dBm

when pump power P_p is fixed at 4 dBm. In Figure 4-8(b), mixing power P_{p-s} increases by approximately 10 dB when pump power P_p is increased by 10 dB. Similarly, mixing power P_{p-s} increases by approximately 10 dB when signal power P_s increases by 10 dB, as shown in Figure 4-8(d). The linear dependency of mixing power P_{p-s} on input power is explained and discussed in [48]. To briefly summarize, when material's compliance modulation (ξ) is small, ξ is linearly proportional to the input amplitude, thus mixing power is also linearly proportional to the input power. The developed coupled multi-resonance circuit model shows similar trends to the experimental data for all the power conditions, as shown in Figure 4-8(a)& Figure 4-8(c). The nonlinear parameter of the AlN was extracted by fitting the circuit model to the experiment data and used for all the nonlinear simulations presented in this paper. The compliance modulation (ξ) for the resonator at P_s = 6 dBm was estimated to be 0.3%, which is comparable to AlN changes under large power in previous publications [38, 48].

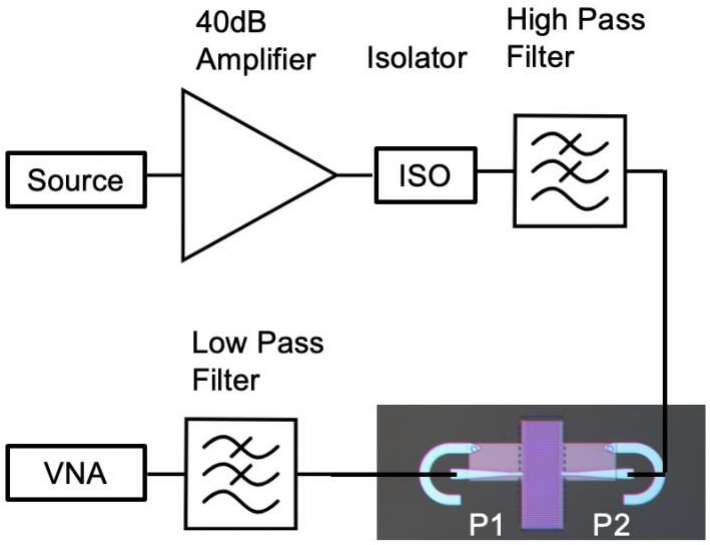

Figure 4-9: Setup of parametric Q-enhancement measurement.

The parametric Q-enhancement phenomenon was simulated using the coupled multi-resonance circuit model and measured using the experimental setup shown in Figure 4-9. Port 1 of the resonator is connected to the vector network analyzer (VNA) to measure the response of signal resonance. Port 2 of the resonator is connected to the pump path to feed pump power P_p at pump frequency f_p. Pump power is generated from the signal source and amplified by the 40 dB power amplifier. An isolator is used to protect the power amplifier from large power reflected from the resonator. The high pass filter (pass band frequency > 1 GHz) isolates the signal path and the pump path, therefore the pump path won't load the signal path. The low pass filter (pass band frequency <625 MHz) in the signal path provides 38 dB insertion loss to pump frequency at 1364 MHz so that large pump power won't saturate the VNA. The influence of LPF to the signal resonance response is calibrated out while using the calibration kit. After calibration, the vector network analyzer measures signal resonance response of the device for different pump frequencies and pump powers. As discussed in the linear measurement, the required pump frequency f_p is off from 3^{rd} resonance and has a relatively high insertion loss (i.e., S21 at f_p = -45 dB, S21 at f_s = -10 dB), thus the signal power is lowered to -30 dBm in this experiment. The IF bandwidth is set to 1 kHz and averaging is set to 10.

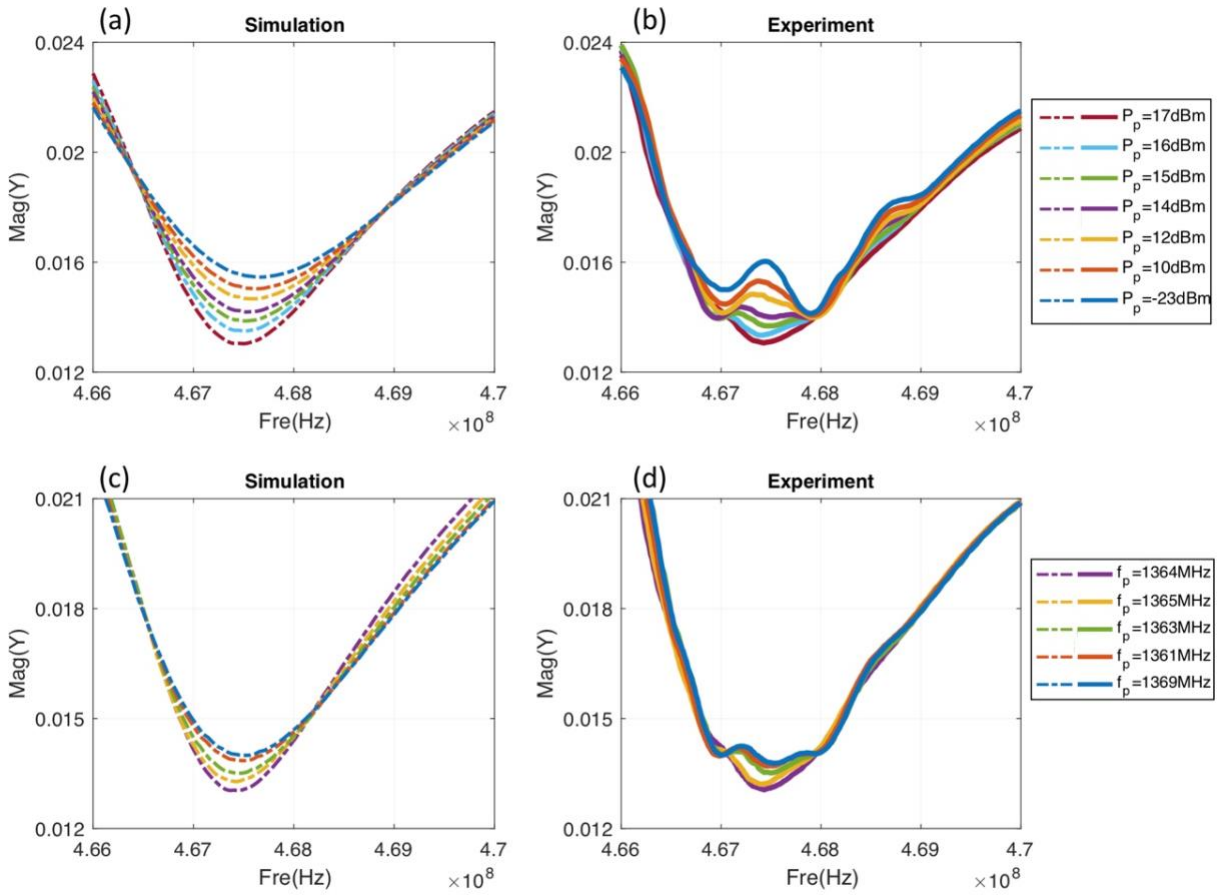

Figure 4-10: Parametric Q-enhancement simulation and experiment results. (a) Simulated and (b) measured magnitude of admittance mag(Y) vs different pump power P_p. The pump frequency is fixed at f_p = 1364 MHz. (c) Simulated and (d) measured magnitude of admittance mag(Y) vs different pump frequency f_p. The pump power is fixed at P_p = 17 dBm.

Figure 4-10(a) and Figure 4-10(b) show simulated and measured magnitude of admittance for parallel resonance under different pump power. The pump frequency is fixed at the optimal frequency f_p = 1364 MHz. P_p = -23 dBm is used as the reference case. Q-enhancement starts to be observed when pump power reaches 10 dBm, and then increases with pump power. The increase of Q with pump power can be explained using the conclusion of the parametric mixing experiment. Material compliance modulation ξ increases with pump amplitude, thus signal path sees an increased negative conductance (from Equation 4.9) and increases the quality factor.

Pump power is raised until P_p = 17 dBm because the device has poor power handling off the resonance frequency. The circuit model predicts similar trends as the experimental data, i.e., Q is enhanced with increasing pump power. The in-band hump in Figure 4-10(b) is attributed to device specific IDT geometry fluctuations due to fabrication. This fabrication imperfection is not captured by the circuit model, which results in admittance shape difference between simulation result and experiment data.

Figure 4-10(c) and Figure 4-10(d) show the simulated and measured magnitude of admittance for different pump frequency. The pump power is fixed at the P_p = 17 dBm. Q-enhancement shows a dependency on the pump frequency because the proposed method relies on the idler resonance, which has a narrow bandwidth. Q is at a maximum when pump frequency is optimal at 1364 MHz, while Q is lowered when the pump frequency is away from 1364 MHz. The simulation predicts similar Q-enhancement dependency on pump frequency because the multi-resonance behavior is captured by the circuit model. These simulation and measurement results verify the proposed parametric Q-enhancement method.

To quantify the Q enhancement, quality factor is extracted using 3dB bandwidth method[78], i.e., the measured Q is extracted from the admittance plot by dividing the resonance frequency by the 3dB bandwidth, as defined by Equation 4.11. Quality factor is verified using phase slope method [79] as defined by Equation 4.12 and parallel resonant circuit fitting method [74]. These extraction methods give same quality factor values. Figure 4-11(a) shows extracted quality factor under different pump power. The pump frequency is fixed at f_p = 1364 MHz. Quality factor increases linearly as pump power increases from 10dBm to 17dBm, as predicted by Equation 4.9. Material compliance modulation ξ increases linearly with pump amplitude, thus the negative resistance and quality factor increases linearly with pump power. Figure 4-11(b) shows extracted quality factor with different pump frequency. The pump power is fixed at P_p = 17 dBm.

Quality factor has a dependency on the pump frequency because the proposed method relies on the idler resonance that has a narrow bandwidth.

Table 4.2 summarizes Q and $f \times Q$ enhancement with increasing pumping power. Q is boosted 1.7 times (i.e., from 100 to 168) when 17 dBm pump power is supplied. 17 dBm pump power is used in this work because the device has a very high insertion loss (S21 = -45 dB) at the pump frequency f_p due to dispersion. The required pump power will be much lowered if the device is less dispersive through certain dispersion compensation and has a reduced insertion loss at the pump frequency f_p. It is also worth noting that if the method is applied to AlN Lamb wave resonators with higher quality factor (e.g., 1000), the normalized negative conductance seen by the signal path (from Equation 4.9) is increased, and thus the quality factor will be further enhanced. This method can be readily applied to high-Q AlN Lamb wave resonator with even greater Q-enhancement expected.

$$\mathrm{Q} = \frac{1}{\text{3dB fractional BW}} \tag{4.11}$$

$$\mathrm{Q} = \frac{\omega_0}{2} \times \left|\frac{\partial \varphi}{\partial \omega}\right|_{\omega_0} \tag{4.12}$$

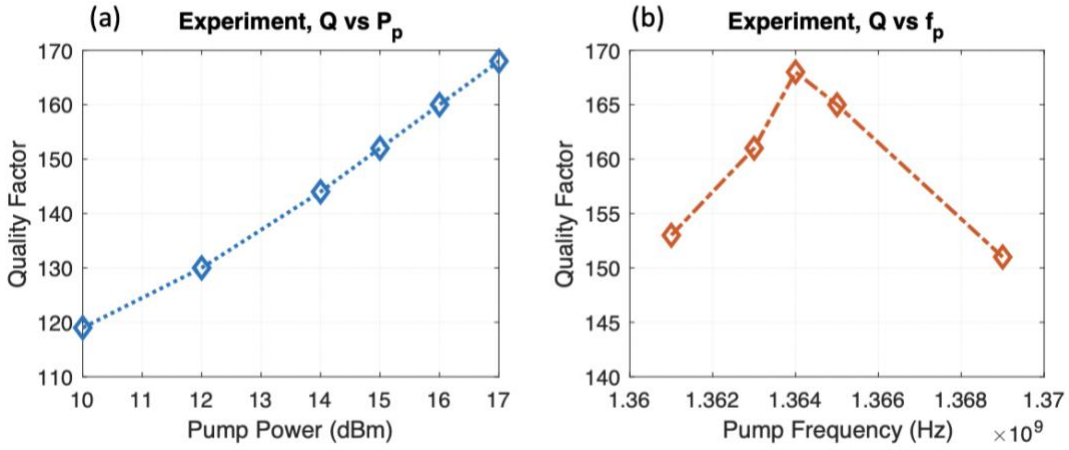

Figure 4-11: Extracted quality factor from measured data. (a) Quality factor vs different pump power P_p. The pump frequency is fixed at f_p = 1364 MHz. (b) Quality factor vs different pump frequency f_p. The pump power is fixed at P_p = 17 dBm.

P_p (dBm)	-23	10	12	14	15	16	17
Q	100	119	130	144	152	160	168
$f \times Q$ (Hz)	4.67×10^8	5.56×10^8	6.07×10^8	6.73×10^8	7.10×10^8	7.48×10^8	7.85×10^8

Table 4.2: Q and $f \times Q$ enhancement with increasing pumping power.

4.5 Future work and Conclusion

The parametric Q-enhancement has been demonstrated on the AlN Lamb wave platform. To enhance filter's performance in terms of lower insertion loss, following work includes cascading parametric Q-enhanced resonators for enhanced acoustic filters. Figure 4-12 shows an acoustic ladder filter made of parametric Q-enhanced acoustic resonators. Each stage of the parametric enhanced filter has reduced in-band insertion loss, therefore within the given insertion loss margin, more Q-enhanced stages can be cascaded to realize filters with improved out of band rejection.

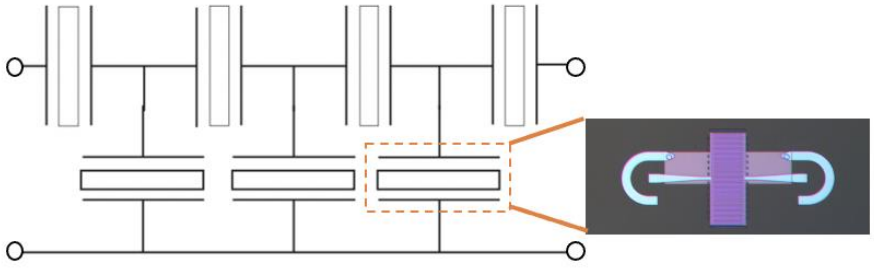

Figure 4-12: Acoustic ladder filter made of parametric Q-enhanced acoustic resonators.

Besides, the proposed Q-enhancement technique and multi-resonance coupled circuit model can be applied to other types of resonators that have nonlinear behavior and support multi-resonance operation. The scandium-doped AlN (ScAlN) film, which can be sputter-deposited such as undoped AlN film, were used to demonstrate high performance resonator with enhanced electromechanical coupling (k_t^2)[80-81]. This k_t^2 is double the value of what has been achieved on similar resonators made of AlN films. Therefore, ScAlN resonators can be cascaded to enhance filter's performance in terms of wider bandwidth. However, the quality factor of the ScAlN resonator is limited, as compared to the AlN resonator. If the parametric Q-enhancement technique is applied to the ScAlN resonator, the quality factor will be boosted, and the Q-enhanced ScAlN resonator will be promising for enhanced filter with lower insertion loss and wider bandwidth.

For conclusion, in this chapter a non-degenerate phase independent parametric Q-enhancement method is explored and demonstrated on an AlN Lamb wave resonator. The conditions to apply the parametric Q-enhancement method is clearly stated. A multi-resonance coupled nonlinear model is developed to simulate the parametric coupling of each resonance and extract the nonlinearity of the AlN from the experimental data. The nonlinear model we developed for multi-resonance acoustic device is a universal model that can be applied for designs of filters and waveguides built on acoustic wave platforms. Parametric mixing effects and Q-enhancement behavior have been demonstrated in both circuit simulation and experiment. The proposed Q-enhancement technique and multi-resonance coupled circuit model can be applied to other types of resonators that have nonlinear behavior and support multi-resonance operation. This work advances the emerging nonlinear field and takes a critical step in its practical application in radio frequency acoustic parametric Q-enhancement.

Chapter 5 Conclusion

This dissertation works on developing parametric mixing and amplification on the nonlinear acoustic wave platform. The challenges addressed are the increasing complexity of mobile RF front-end because of advanced communication standards, and the need for developing high performance next device generation RF front-end which will be more efficient and smaller than presently available. Specifically, acoustic wave technologies in the active domain are investigated in this dissertation, which obtain great leverage on the short wavelength of acoustic waves at RF to minimize the footprint of transmission lines, and the high quality factor of mechanical resonances and acoustic wave propagation to reduce the noise associated with energy loss. This dissertation is to yield a new class of acoustic RF front-end which includes nonlinear acoustic components such as acoustic mixers that provide orders of magnitude improvement in sizes, and acoustic resonators with enhanced and amplified performance.

In chapter 2 the proposed concept of acoustic nonlinear transmission line is investigated for power efficient acoustic parametric amplification. Firstly, the past works on electromagnetic time varying transmission line and its implementation on the nonlinear components are introduced. Then the acoustic nonlinear transmission line idea is proposed using the analogy between electromagnetic wave and acoustic wave, i.e., mechanical compliance in the acoustic waveguide is analogous to the capacitance modulated in the time varying transmission line. Similar parametric mixing phenomenon is expected to happen in the nonlinear acoustic waveguide where the mechanical stiffness is modulated by the pump wave. The proposed idea is first validated using multi-physics finite element simulation, and then matched with analytical equations derived for time varying transmission line.

In chapter 3 practical implementations of acoustic nonlinear transmission line are investigated. Nonlinear constitutive equations demonstrate the coupling concept of nonlinear permittivity to

nonlinear mechanical stiffness. This external permittivity coupling method is proved by BST coupled surface acoustic wave grating where parametric mixing and amplification are observed. Besides, nonlinear acoustic transmission line implementation using AlN is proved on the Lamb wave platform by a three-port Lamb wave delay line. Parametric mixing and frequency conversion are observed in experiment, and the nonlinear stiffness of AlN is extracted by the equivalent circuit model from experimental data. Comparing to BST implementation, AlN implementation demonstrates a higher nonlinear stiffness modulation and is more optimal for power efficient parametric mixing and amplification purpose.

In chapter 4 a non-degenerate phase independent parametric Q-enhancement technique is explored and demonstrated on AlN Lamb wave resonators. This technique is implemented by parametrically pumping AlN material stiffness to realize a negative resistance seen at the signal path. The conditions to apply the parametric Q-enhancement technique is clearly stated. A nonlinear circuit model is developed to simulate the parametric coupling of each resonance and extract the nonlinearity of AlN from experimental data. The device quality factor is boosted in both simulation and experiment with proper pump frequency and pump power. The proposed Q-enhancement technique and multi-resonance coupled circuit model can be applied to other types of resonators that have nonlinear behavior and support multi-resonance operation.

This dissertation presents a complete study of parametric mixing and amplification on the nonlinear acoustic platform. This includes the theory and concept of nonlinear acoustic transmission line, practical implementations using nonlinear materials, and applications of acoustic parametric mixing and amplification. This dissertation advances the emerging nonlinear field and takes a critical step in its practical application in RF acoustic active components. The author hopes that the advancements discussed in this dissertation will lead to further developments in nonlinear acoustic devices for future communication systems.

Appendix A Fabrication and Measurement Note

A1 Surface Acoustic Wave Devices

The fabrication process of surface acoustic wave delay lines is developed in the Integrated Systems Nanofabrication Cleanroom and Nanolab of University of California, Los Angeles. The process includes wafer preparation, photolithography, develop, metal deposition and lift off.

Wafer preparation: The piezoelectric substrate for exciting surface acoustic wave is YX-128° lithium niobate thin film, which is cleaned using Matrix 105 – Downstream Ashier and dehydrated using hot plate at 100 ℃ for 10 minutes. After that, the substrate is cooled down for 5 minutes before spinning the photoresists.

Photolithography: HDMS and AZ nLOF 2020 are the chosen photoresists, which are deposited on the lithium niobate substrate using Headway PWM32 – Spin Coater. First the HDMS is put on the top of substrate with a pipe, spinning at 500 rpm spin speed with 500 rpm/s spin ramp for 5 seconds, followed by 3000 rpm spin speed with 500 rpm/s spin ramp for 60 seconds. Secondly the AZ nLOF 2020 is poured on the wafer and spinning at 500 rpm spin speed with 500 rpm/s spin ramp for 5 seconds, followed by 3000 rpm spin speed with 500 rpm/s spin ramp for 60 seconds. After covering the sample with photoresists, the sample is placed at the hot plate at 110℃ for 1 minute's soft bake before cooling down. The sample and the mask are then placed on Karl Suss MA6 Contact Aligner for exposure. The photomask is drawn using L-edit and made by Heidelberg DW66 Laser writer. The exposure time is 7.7 second with 8.5 mW power, which should be adjusted by the exact power shown on the machine. After exposure, the sample is placed on the hot plate at 110℃ for 1 minute's post exposure bake.

Develop: Before depositing the metal on the sample, the photoresist should be developed to obtain the desired pattern. During the develop process, the sample is immersed in a beaker with half MIF 300 for 50 seconds. Photoresists that are exposed by the UV Light become soluble in the solvent. After developing, the wafer is cleaned again before metal deposition.

Metal Deposition: The material for interdigital transducers of the surface acoustic wave delay line is Al deposited by CHA Mark 40 Electron Beam Evaporator. The thickness of the Al deposited is 70nm, which is precisely controlled by the crystal in the Electron Beam Evaporator equipment.

Lift off: For the lift off process, the sample is immersed in a beaker of half NMP with Al Foil covering on the low-speed Orbit-shaker for one night. During the liftoff process, photoresist becomes soluble in the solvent, and metal on the photoresist is moved by the photoresist. In this way, the pattern is transferred from photoresist to metal.

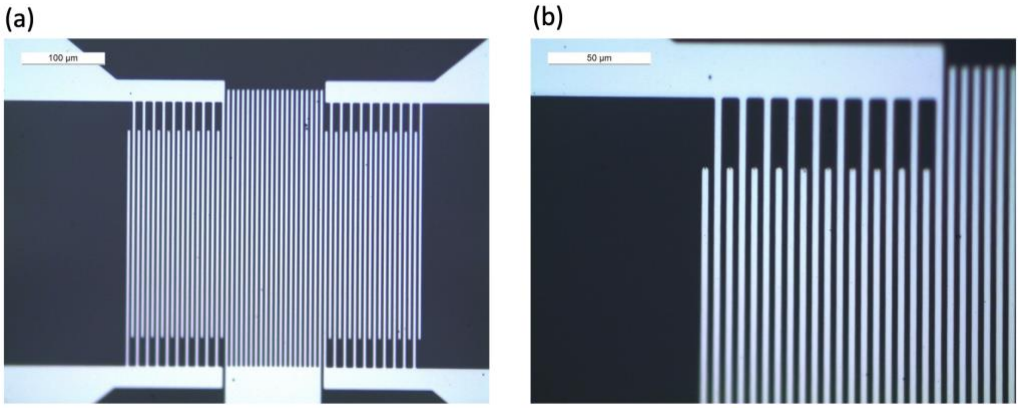

Figure A1.1.1 Optical images of surface acoustic wave delay lines.

Images of surface acoustic wave delay lines under optical microscope with different lenses are shown in Figure A1.1.1. There will be defects in one or two surface acoustic wave devices for

every chip, but overall, the devices are fabricated as expected, with fine and clean patterns of electrodes.

The PCB for testing the surface acoustic wave devices is shown in Figure A1.1.2(a), which is drawn and simulated in Advanced Design System (ADS) before being cut by the LPKF ProtoLaser machine in the center for High Frequency Electronics in UCLA. Because the size of each surface acoustic wave device is very small, four surface acoustic wave devices are put on the same PCB for testing. The SMA connectors are wire bonded to the PCB before the chip is pastes on the PCB using tape. The chips fabricated in the clean room are diced and wire bonded to the PCB. The final design for measurement is shown in Figure A1.1.2 (b), with each set of SMA connected to the two feeding pads of the surface acoustic wave delay lines.

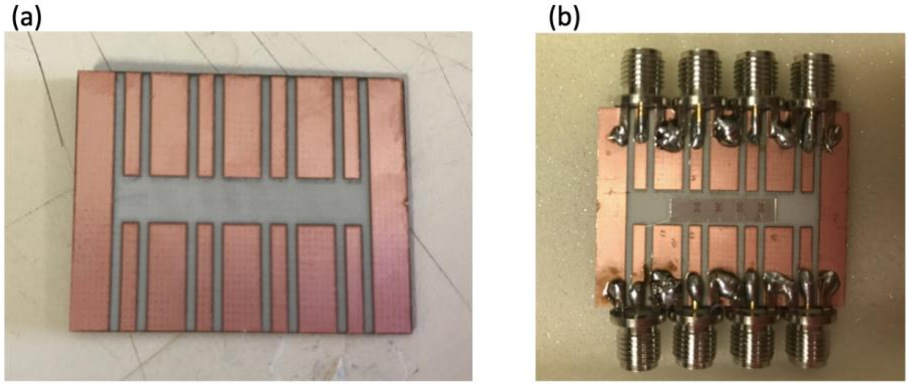

Figure A1.1.2 (a) PCB cut by Laser Machine and (b) device for testing.

A2 Lamb Wave Devices

The fabrication process of the lamb wave devices is developed from Sidhant Tiwari's dissertation[77]. Here is only a brief summarized fabrication recipe, which includes wafer preparation, patterned Pt deposition, AlN deposition, via etch, patterned Al deposition, release vent etch, and Si etch. More details can be found in appendix of ref[77].

Wafer preparation: The wafer for lamb wave devices is a blank Si substrate with resistivity greater than 10 kΩ. cm. The wafer is cleaned using acetone, methanol, IPA, DI water and dehydrated using hot plate at 150 ℃ for 15 minutes.

Patterned Pt deposition: HDMS and AZ nLOF 2020 are the chosen photoresists for patterned Pt deposition on Si. HMDS vapor is firstly coated on Si wafer for 10 minutes. Then the AZ nLOF 2020 is poured to the wafer and is spinning at 500 rpm spin speed with 100 rpm/s spin ramp for 5 seconds, followed by 3000 rpm spin speed with 1000 rpm/s spin ramp for 30 seconds. Soft bake is 1 minute at 100℃. The exposure time is 4.7 second with 12 mW power. Post exposure bake is 1 minute at 100℃. During the develop process, the sample is immersed in a beaker with half MIF 300 for 60 second and cleaned using DI water. Descum in Oxygen plasma using 1minute recipe in Matrix Ashes is recommended for removing the remaining photoresist. 10nm Ti and 50nm Pt are deposited on the sample using CHA Electron Beam Evaporator. For the lift off process, the sample is immersed in a beaker of half NMP with Al Foil covering on the low-speed Orbit-shaker for one night.

AlN deposition: The AlN layer is sent to Claire and John Bertucci Nanotechnology Laboratory of Carnegie Mellon University for AlN deposition. The thickness of AlN is 400nm. The film is deposited with slightly tensile stress. The average AlN stress is -28.8MPa.

via etch: KMPR1005 is the chosen photoresist for via etch. The sample is cleaned and dehydrated at 150 ℃ for 15 minutes. KMPR1005 is poured to the sample and is spinning at 500 rpm spin speed with 100 rpm/s spin ramp for 5 seconds, followed by 3000 rpm spin speed with 300 rpm/s spin ramp for 30 seconds. Edge bead removal is performed using cleanroom swab dipped in acetone. Soft bake is 5 minutes at 100℃. The exposure time is 7.4 second with 12 mW power. Post exposure bake is 2 minutes at 100℃. During the develop process, the sample is immersed in a beaker with SU8 developer for 9 minutes. It is recommended to do development

in a beaker with a stirring bar and with the sample facing down. To clean the sample after development, fresh SU8 developer is sprayed to wash the sample for 10 seconds, IPA is then sprayed to wash the sample for another 10 seconds. Then the sample is rinsed with DI water and dried with nitrogen. For via etch (wet etch for AlN), the sample is immersed in a beaker with AZ300MIF. The sample is taken out every 2 mins and dunked in a beaker with DI water immediately to stop the etching. The sample is then dried and observed under microscope. The etch is easily observed by color change under microscope. When the etch is finishing, the AlN starts to look spotty and then the etch will start to clear out the spots. Keep repeating the above etch process before the wet etch is completed. Total time is 10-20 minutes, and it depends on the size of vias and thickness of AlN. To remove the photoresist after via etch, the sample is immersed in NMP at 80℃ for 1-2 hours or longer.

Patterned Al deposition: KMPR1005 is the chosen photoresist for Al deposition and the photolithography process is the same with that in via etch. 10nm Ti and 100nm Al are deposited on the sample. For the lift off process, the sample is immersed in immersed in NMP at 80℃ for 4-5 hours or longer. It is recommended to do liftoff with a stirring bar and with the sample facing down.

Release vent etch: KMPR1005 is the chosen photoresist for release vent etch and the photolithography process is the same with that in via etch. The AlN and Pt are etched using chlorine-based plasma. After etching, release vents are shown as grey (the color of silicon) under microscope. To remove the photoresist after the release vent etch, the sample is immersed in NMP at 80℃ for 1-2 hours or longer.

Si etch: The sample is dehydrated at 150 ℃ for 15 minutes before the Si is isotropic etched by XeF_2. The pulse duration is 1 minute, and the pressure is set to 2500 mTorr. The number of pulses vary for each design.

Figure A1.2.1(a) shows the whole wafer after Pt deposition. The wafer is then sent out for AlN deposition. Figure A1.2.1 (b) and A1.2.1 (c) are the optical images of a via after 6 mins of wet etch and 10 mins of wet etch. By comparing figure A1.2.1 (b) and A1.2.1 (c), the gradual clear of spots inside the via is observed. Figure A1.2.1 (d) shows the optical image of lamb wave resonator before the Si etch, with top electrode (Al), bottom electrode (Pt), via and release vent clearly labeled. The wafer is diced into dies as shown in figure A1.2.1 (e), for the ease of Si etch and the following measurements.

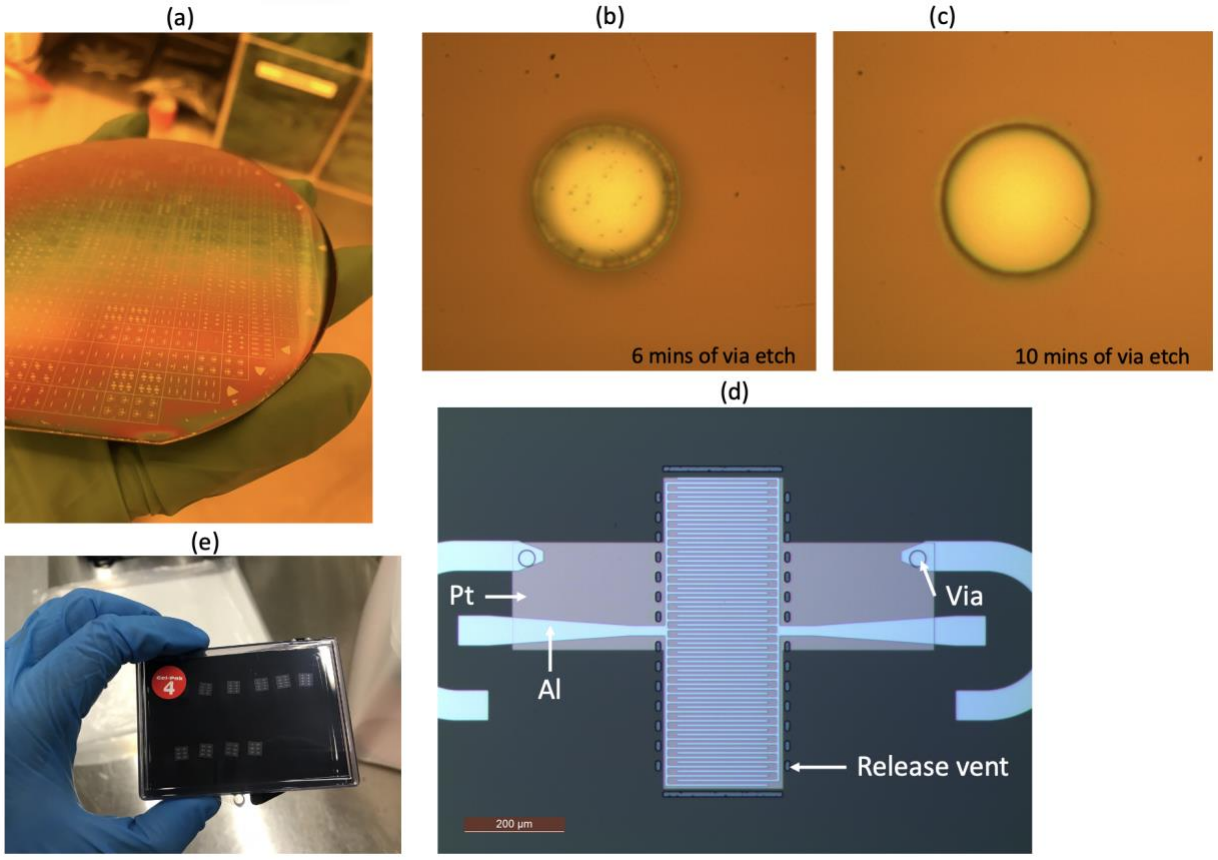

Figure A1.2.1 (a) The whole wafer after Pt deposition. The images of a via under optical microscope after (b) 6 mins of wet etch and (c) 10 mins of wet etch. The spots are gradually cleared during the wet etch process. (d) The optical image of lamb wave resonator before the Si etch. The top electrode (Al), bottom electrode (Pt), via and release vent are clearly labeled. (e) Diced dies.

The characterization of lamb wave resonators is performed using cascade probe station in the center for High Frequency Electronics in UCLA. As shown in figure A1.2.2, two ground-signal-ground probes are used for contacting the Al pads on the device under test. The probes are connected to the equipment like VNA, or spectrum analyzer for measuring the response. The microscope is for probing, and the positioning arm is adjusted for metal contacting.

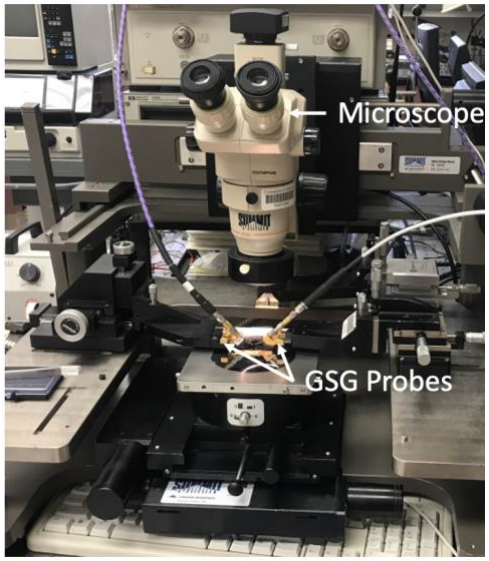

Figure A1.2.2 Cascade probe station for characterizing the lamb wave resonators.

References

1. Ruppel, C. C. W., Acoustic Wave Filter Technology-A Review. *IEEE Trans Ultrason Ferroelectr Freq Control* **2017,** *64* (9), 1390-1400.

2. White, R. M.; Voltmer, F. W., Direct Piezoelectric Coupling to Surface Elastic Waves. *Applied Physics Letters* **1965,** *7* (12), 314-316.

3. Tobolka, G.; Faber, W.; Albrecht, G.; Pilz, D., High Volume TV-IF Filter Design, Fabrication, and Applications. In *IEEE 1984 Ultrasonics Symposium*, 1984; pp 1-12.

4. Lakin, K. M.; Wang, J. S., Acoustic bulk wave composite resonators. *Applied Physics Letters* **1981,** *38* (3), 125-127.

5. Olsson, R. H.; Hattar, K.; Homeijer, S. J.; Wiwi, M.; Eichenfield, M.; Branch, D. W.; Baker, M. S.; Nguyen, J.; Clark, B.; Bauer, T.; Friedmann, T. A., A high electromechanical coupling coefficient SH0 Lamb wave lithium niobate micromechanical resonator and a method for fabrication. *Sensors and Actuators A: Physical* **2014,** *209*, 183-190.

6. Gevorgian, S. S. T. A. K. V. A. K., *Tuneable Film Bulk Acoustic Wave Resonators*. 2013.

7. Smith, W. R.; Gerard, H. M.; Collins, J. H.; Reeder, T. M.; Shaw, H. J., Analysis of Interdigital Surface Wave Transducers by Use of an Equivalent Circuit Model. *IEEE Transactions on Microwave Theory and Techniques* **1969,** *17* (11), 856-864.

8. Pozar, D. M., *Microwave Engineering*.

9. Tien, P.; Suhl, H., A Traveling-Wave Ferromagnetic Amplifier. *Proceedings of the IRE* **1958,** *46* (4), 700-706.

10. Tien, P. K., Parametric Amplification and Frequency Mixing in Propagating Circuits. *Journal of Applied Physics* **1958,** *29* (9), 1347-1357.

11. Cullen, A. L., A Travelling-Wave Parametric Amplifier. *Nature* **1958,** *181* (4605), 332-332.

12. Landauer, R., Parametric Amplification along Nonlinear Transmission Lines. *Journal of Applied Physics* **1960,** *31* (3), 479-484.

13. Suarez, A.; Melville, R., Simulation-assisted design and analysis of varactor-based frequency multipliers and dividers. *IEEE Transactions on Microwave Theory and Techniques* **2006,** *54* (3), 1166-1179.

14. Magierowski, S.; Bousquet, J. F.; Zhixing, Z.; Zourntos, T., RF CMOS Parametric Downconverters. *IEEE Transactions on Microwave Theory and Techniques* **2010,** *58* (3), 518-528.

15. Kabir, S.; Magierowski, S.; Messier, G. G.; Zhao, Z., A Direct 100 GHz Parametric CMOS Tripler. *IEEE Microwave and Wireless Components Letters* **2013,** *23* (10), 557-559.

16. Gray, B.; Melville, B.; Kenney, J. S., Analytical Modeling of Microwave Parametric Upconverters. *IEEE Transactions on Microwave Theory and Techniques* **2010,** *58* (8), 2118-2124.

17. Lee, W.; Afshari, E., Distributed Parametric Resonator: A Passive CMOS Frequency Divider. *IEEE Journal of Solid-State Circuits* **2010,** *45* (9), 1834-1844.

18. Lee, W.; Afshari, E., Low-Noise Parametric Resonant Amplifier. *IEEE Transactions on Circuits and Systems I: Regular Papers* **2011,** *58* (3), 479-492.

19. Foster, M. A.; Turner, A. C.; Sharping, J. E.; Schmidt, B. S.; Lipson, M.; Gaeta, A. L., Broad-band optical parametric gain on a silicon photonic chip. *Nature* **2006,** *441* (7096), 960-3.

20. Marhic, M. E.; Andrekson, P. A.; Petropoulos, P.; Radic, S.; Peucheret, C.; Jazayerifar, M., Fiber optical parametric amplifiers in optical communication systems. *Laser Photon Rev* **2015,** *9* (1), 50-74.

21. Kuo, B. P.; Hirano, M.; Radic, S., Continuous-wave, short-wavelength infrared mixer using dispersion-stabilized highly-nonlinear fiber. *Opt Express* **2012,** *20* (16), 18422-31.

22. Yu, Z.; Fan, S., Complete optical isolation created by indirect interband photonic transitions. *Nature Photonics* **2009,** *3* (2), 91-94.

23. Sharping, J. E.; Fiorentino, M.; Kumar, P.; Windeler, R. S., Optical parametric oscillator based on four-wave mixing in microstructure fiber. *Opt Lett* **2002,** *27* (19), 1675-7.

24. Mohebbi, H. R.; Majedi, A. H., Analysis of Series-Connected Discrete Josephson Transmission Line. *IEEE Transactions on Microwave Theory and Techniques* **2009,** *57* (8), 1865-1873.

25. Yaakobi, O.; Friedland, L.; Macklin, C.; Siddiqi, I., Parametric amplification in Josephson junction embedded transmission lines. *Physical Review B* **2013,** *87* (14).

26. Qin, S.; Xu, Q.; Wang, Y. E., Nonreciprocal Components With Distributedly Modulated Capacitors. *IEEE Transactions on Microwave Theory and Techniques* **2014,** *62* (10), 2260-2272.

27. Qin, S.; Wang, Y. E., Broadband Parametric Circulator with Balanced Monolithic Integrated Distributedly Modulated Capacitors (DMC). In *2016 IEEE MTT-S International Microwave Symposium (IMS)*, 2016; pp 1-4.

28. Wu, Q.; Zou, X.; Qin, S.; Wang, Y. E., Frequency translational RF receiver with time varying transmission lines (TVTL). In *2017 IEEE MTT-S International Microwave Symposium (IMS)*, 2017; pp 1767-1769.

29. Wu, Q.; Zou, X.; Wang, Y. E., Jamming Resilient Spread Spectrum Receiver with Time-Varying Transmission Line (TVTL) RF Correlator. In *2020 IEEE Radio and Wireless Symposium (RWS)*, 2020; pp 20-23.

30. Wu, Q.; Zou, X.; Zhu, R.; Wang, Y. E., Chip-Scale RF Correlator with Monolithically Integrated Time-Varying Transmission Line (TVTL). In *2018 IEEE/MTT-S International Microwave Symposium - IMS*, 2018; pp 431-434.

31. Zou, X.; Wu, Q.; Wang, Y. E., Monolithically Integrated Parametric Mixers With Time-Varying Transmission Lines (TVTLs). *IEEE Transactions on Microwave Theory and Techniques* **2020,** *68* (10), 4479-4490.

32. Chao, G., Parametric Amplification of Surface Acoustic Waves. *Applied Physics Letters* **1970,** *16* (10), 399-401.

33. Inaba, R.; Mikoshiba, N., Parametric amplification of surface acoustic wave of ZnO-Ga-doped yttrium iron garnet. *Applied Physics Letters* **1982,** *41* (1), 25-26.

34. Rotter, M.; Ruile, W.; Wixforth, A., Non-reciprocal SAW devices for RF applications. In *2000 IEEE Ultrasonics Symposium. Proceedings. An International Symposium (Cat. No.00CH37121)*, 2000; pp 35-38.

35. Supriyo, D., *Surface Acoustic Wave Devices*. Prentice-Hall: 1986.

36. Basceri, C.; Streiffer, S. K.; Kingon, A. I.; Waser, R., The dielectric response as a function of temperature and film thickness of fiber-textured (Ba,Sr)TiO3 thin films grown by chemical vapor deposition. *Journal of Applied Physics* **1997,** *82* (5), 2497-2504.

37. Noeth, A.; Yamada, T.; Muralt, P.; Tagantsev, A. K.; Setter, N., Tunable thin film bulk acoustic wave resonator based on Ba(x)Sr(1-x)TiO3 thin film. *IEEE Trans Ultrason Ferroelectr Freq Control* **2010,** *57* (2), 379-85.

38. Defay, E.; Ben Hassine, N.; Emery, P.; Parat, G.; Abergel, J.; Devos, A., Tunability of aluminum nitride acoustic resonators: a phenomenological approach. *IEEE Trans Ultrason Ferroelectr Freq Control* **2011,** *58* (12), 2516-20.

39. Cherednick, V. I.; Dvoesherstov, M. Y., Surface acoustic wave, electric boundary conditions, velocity control, sensors. In *2011 International Conference on Multimedia Technology*, 2011; pp 6075-6077.

40. Myers, L. E.; Bosenberg, W. R., Periodically poled lithium niobate and quasi-phase-matched optical parametric oscillators. *IEEE Journal of Quantum Electronics* **1997,** *33* (10), 1663-1672.

41. Gallo, K.; Assanto, G.; Parameswaran, K. R.; Fejer, M. M., All-optical diode in a periodically poled lithium niobate waveguide. *Applied Physics Letters* **2001,** *79* (3), 314-316.

42. Yao, Z.; Tiwari, S.; Lu, T.; Rivera, J.; Luong, K. Q. T.; Candler, R. N.; Carman, G. P.; Wang, Y. E., Modeling of Multiple Dynamics in the Radiation of Bulk Acoustic Wave Antennas. *IEEE Journal on Multiscale and Multiphysics Computational Techniques* **2020,** *5*, 5-18.

43. Yao, Z.; Wang, Y. E.; Keller, S.; Carman, G. P., Bulk Acoustic Wave-Mediated Multiferroic Antennas: Architecture and Performance Bound. *IEEE Transactions on Antennas and Propagation* **2015,** *63* (8), 3335-3344.

44. Gao, A.; Zou, J., Extremely High Q AlN Lamb Wave Resonators Implemented by Weighted Electrodes. In *2019 IEEE International Electron Devices Meeting (IEDM)*, 2019; pp 34.5.1-34.5.4.

45. Mal, A. K. a. S., S.J., *Deformation of elastic solids*. Prentice Hall: 1991.

46. On waves in an elastic plate. *Proceedings of the Royal Society of London. Series A, Containing Papers of a Mathematical and Physical Character* **1997,** *93* (648), 114-128.

47. Schneider, J. D. Next Generation Acoustic and Magnetic Devices for Radio Frequency Communication. 2020.

48. Schneider, J. D.; Lu, T.; Tiwari, S.; Zou, X.; Mal, A.; Candler, R. N.; Wang, Y. E.; Carman, G. P., Frequency conversion through nonlinear mixing in acoustic waves. *Journal of Applied Physics* **2020,** *128* (6).

49. Lin, C.-M.; Yantchev, V.; Zou, J.; Chen, Y.-Y.; Pisano, A. P., Micromachined One-Port Aluminum Nitride Lamb Wave Resonators Utilizing the Lowest-Order Symmetric Mode. *Journal of Microelectromechanical Systems* **2014,** *23* (1), 78-91.

50. Piazza, G., Contour-Mode Aluminum Nitride Piezoelectric MEMS Resonators and Filters. In *MEMS-based Circuits and Systems for Wireless Communication*, 2013; pp 29-54.

51. Hashimoto, K.-y., *Surface Acoustic Wave Devices in Telecommunications*. 2000.

52. Hashimoto, K.-y., *RF bulk acoustic wave filters for communications*. 2009.

53. Piazza, G.; Stephanou, P. J.; Pisano, A. P., Single-Chip Multiple-Frequency ALN MEMS Filters Based on Contour-Mode Piezoelectric Resonators. *Journal of Microelectromechanical Systems* **2007,** *16* (2), 319-328.

54. Piazza, G.; Stephanou, P. J.; Pisano, A. P., Piezoelectric Aluminum Nitride Vibrating Contour-Mode MEMS Resonators. *Journal of Microelectromechanical Systems* **2006,** *15* (6), 1406-1418.

55. Rinaldi, M.; Zuniga, C.; Zuo, C.; Piazza, G., Super-high-frequency two-port AlN contour-mode resonators for RF applications. *IEEE Trans Ultrason Ferroelectr Freq Control* **2010,** *57* (1), 38-45.

56. Zou, J.; Lin, C.-M.; Gao, A.; Pisano, A. P., The Multi-Mode Resonance in AlN Lamb Wave Resonators. *Journal of Microelectromechanical Systems* **2018,** *27* (6), 973-984.

57. Lam, C. a. G., Anming and Lin, Chih-Ming and Zou, Jie, A review of Lamé and Lamb mode crystal resonators for timing applications and prospects of Lamé and Lamb mode PiezoMEMS resonators for filtering applications. *Proc. Int. Symp. Acoustic Devices Future Mobile Commun. Syst.* **2018**.

58. Segovia-Fernandez, J.; Cremonesi, M.; Cassella, C.; Frangi, A.; Piazza, G., Anchor Losses in AlN Contour Mode Resonators. *Journal of Microelectromechanical Systems* **2015,** *24* (2), 265-275.

59. Lozzi, A.; Villanueva, L. G.; Yen, E. T.-T., Anchor loss dependence on electrode materials in contour mode resonators. In *2016 IEEE International Frequency Control Symposium (IFCS)*, 2016; pp 1-4.

60. Miller, J. M. L.; Ansari, A.; Heinz, D. B.; Chen, Y.; Flader, I. B.; Shin, D. D.; Villanueva, L. G.; Kenny, T. W., Effective quality factor tuning mechanisms in micromechanical resonators. *Applied Physics Reviews* **2018,** *5* (4).

61. Gao, A.; Winterkorn, M.; Yang, Y.; Lu, R.; Provine, J.; Gong, S., Boosting Qs of AlN Resonators by Redefining Acoustic Boundaries. In *2019 IEEE 32nd International Conference on Micro Electro Mechanical Systems (MEMS)*, 2019; pp 883-886.

62. Pillai, G.; Li, S.-S., Quality factor boosting of bulk acoustic wave resonators based on a two dimensional array of high-Q resonant tanks. *Applied Physics Letters* **2020,** *116* (16).

63. Xu, C.; Kochhar, A.; Piazza, G., Dynamic Q-enhancement in aluminum nitride contour-mode resonators. *Applied Physics Letters* **2019,** *115* (17).

64. Naing, T. L.; Nilchi, J. N.; Liu, R.; Rocheleau, T. O.; Nguyen, C. T. C., Active Q-control for improved insertion loss micromechanical filters. In *2014 IEEE International Frequency Control Symposium (FCS)*, 2014; pp 1-6.

65. Rugar, D.; Grutter, P., Mechanical parametric amplification and thermomechanical noise squeezing. *Phys Rev Lett* **1991,** *67* (6), 699-702.

66. Carr, D. W.; Evoy, S.; Sekaric, L.; Craighead, H. G.; Parpia, J. M., Parametric amplification in a torsional microresonator. *Applied Physics Letters* **2000,** *77* (10), 1545-1547.

67. Guo, C.; Fedder, G. K., A quadratic-shaped-finger comb parametric resonator. *Journal of Micromechanics and Microengineering* **2013,** *23* (9).

68. Lee, J.; Li, C.-S.; Wang, Z.; Li, M.-H.; Chin, C.-H.; Li, S.-S.; Feng, P. X. L., Exploring parametric resonance effects in bulk-mode CMOS-MEMS resonators. In *2014 IEEE International Frequency Control Symposium (FCS)*, 2014; pp 1-3.

69. Mahboob, I.; Yamaguchi, H., Piezoelectrically pumped parametric amplification and Q enhancement in an electromechanical oscillator. *Applied Physics Letters* **2008,** *92* (17).

70. Lu, T.; Schneider, J. D.; Zou, X.; Tiwari, S.; Yao, Z.; Carman, G.; Candler, R. N.; Wang, Y. E., Lamb Wave Resonator Loaded Non-reciprocal RF Devices. In *2020 IEEE/MTT-S International Microwave Symposium (IMS)*, 2020; pp 516-519.

71. Engelbrecht, R., Parametric Energy Conversion by Nonlinear Admittances. *Proceedings of the IRE* **1962,** *50* (3), 312-321.

72. Yeung, L. K.; Zou, X.; Wang, Y. E., Parametric quality factor enhancement for highly-selective miniaturized BPFs. In *2020 IEEE Radio and Wireless Symposium (RWS)*, 2020; pp 148-151.

73. Yeung, L. K.; Zou, X.; Wang, Y., Parametrically enhanced bandpass filters. *IET Microwaves, Antennas & Propagation* **2021**.

74. Pozar, D. M., *Microwave Engineering*. John wiley & sons: 2011.

75. Lu, T.; Schneider, J. D.; Yao, Z.; Carman, G.; Wang, Y. E., Nonlinear Surface Acoustic Wave Grating for Parametric Amplification. In *2019 IEEE Radio and Wireless Symposium (RWS)*, 2019; pp 1-3.

76. Wang, Y.; Goh, W. L.; Chai, K. T.; Mu, X.; Hong, Y.; Kropelnicki, P.; Je, M., Parasitic analysis and pi-type Butterworth-Van Dyke model for complementary-metal-oxide-semiconductor Lamb wave resonator with accurate two-port Y-parameter characterizations. *Rev Sci Instrum* **2016,** *87* (4), 045004.

77. Tiwari, S. Dynamics of Multiferroic Coupling. UCLA, 2020.

78. Lin, C.-M.; Lai, Y.-J.; Hsu, J.-C.; Chen, Y.-Y.; Senesky, D. G.; Pisano, A. P., High-Q aluminum nitride Lamb wave resonators with biconvex edges. *Applied Physics Letters* **2011,** *99* (14).

79. Campanella, H., *Acoustic Wave and Electromechanical Resonators: Concept to Key Applications*. Artech House: 2010.

80. Colombo, L.; Kochhar, A.; Xu, C.; Piazza, G.; Mishin, S.; Oshmyansky, Y., Investigation of 20% scandium-doped aluminum nitride films for MEMS laterally vibrating resonators. In *2017 IEEE International Ultrasonics Symposium (IUS)*, 2017; pp 1-4.

81. Park, M.; Hao, Z.; Kim, D. G.; Clark, A.; Dargis, R.; Ansari, A., A 10 GHz Single-Crystalline Scandium-Doped Aluminum Nitride Lamb-Wave Resonator. In *2019 20th International Conference on Solid-State Sensors, Actuators and Microsystems & Eurosensors XXXIII (TRANSDUCERS & EUROSENSORS XXXIII)*, 2019; pp 450-453.